Methanol oxidation on oxygen covered Cu surfaces

Sung Sakong

Technische Universität München
Physik-Department T30
Univ.-Prof. Dr. A. Groß

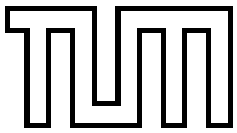

Methanol oxidation on oxygen covered Cu surfaces

Sung Sakong

Vollständiger Abdruck der von der Fakultät für Physik der Technischen Universität München zur Erlangung des akademischen Grades eines

Doktors der Naturwissenschaften (Dr. rer. nat.)

genehmigten Dissertation.

Vorsitzender:		Univ.-Prof. Dr. Katharina Krischer
Prüfer der Dissertation:	1.	Univ.-Prof. Dr. Axel Groß, Universität Ulm
	2.	Univ.-Prof. Dr. Wilhelm Brenig, em.

Die Dissertation wurde am 2. Juni 2005 bei der Technischen Universität München eingereicht und durch die Fakultät für Physik am 25. Juli 2005 angenommen.

Abstract

The partial oxidation of methanol to formaldehyde on clean and oxygen precovered Cu(100) and Cu(110) has been studied by density functional theory calculations within the generalized gradient approximation. We have studied the geometric and electronic structure of the reaction intermediates. Methanol is only very weakly bound to copper while methoxy is chemisorbed. Furthermore, we have identified a highly deformed formaldehyde species strongly interacting with Cu(100) and Cu(110). The reaction paths have been determined using the nudged elastic band method. It turns out that the rate-limiting step is the dehydrogenation of methoxy to formaldehyde which is hindered by a significant activation barrier. While dosing with oxygen does not reduce this barrier, it still facilitates this reaction by stabilizing the methoxy intermediate on the Cu surface and causing the removal of surface hydrogen via water desorption.

Zusammenfassung

Die Oxidation von Methanol zu Formaldehyd über reinen und Sauerstoff-vorbedeckten Cu(100)- und Cu(110)-Oberflächen wurde mittels Dichtefunktionaltheorie in der verallgemeinerten Gradientennäherung untersucht. Durch Analyse der geometrischen und elektronischen Struktur der Reaktions-Zwischenprodukte entsteht ein detailliertes Bild des Reaktionsmechanismus. Methanol ist mit 0.3 eV nur sehr schwach auf der Kupferoberfläche gebunden. Im Gegensatz dazu geht Methoxid, mit einer Bindungsenergie von 2.8 eV, mit der Oberfläche eine starke chemische Bindung ein. Außerdem wurde ein ungewöhnlich stark deformiertes Formaldehyd gefunden, welches sehr stark mit den Kupferoberflächen wechselwirkt. Der Reaktionspfad wurde mit der NEB-Methode (*nudged elastic band*) bestimmt. Aus der Untersuchung geht hervor, daß der Reaktionsschritt, der die Reaktionsrate limitiert, die Oxidation von Methoxid zu Formaldehyd ist. Dieser Oxidationsschritt wird von einer hohen Aktivierungsbarriere behindert. Obwohl die Vorbedeckung mit Sauerstoff die Barriere nicht reduziert, erleichtert sie dennoch die Reaktion durch die Stabilisierung des Methoxids auf der Kupferoberfläche und durch Öffnen eines weiteren Reaktionspfades, der die Entfernung des Oberflächenwasserstoffs durch Wasserdesorption ermöglicht.

Acknowledgments

Most of all, I thanks my supervisor Prof. Dr. Axel Groß with my best esteem to allow me to join his active and challenging group and to research on this interesting subject. Without his valuable advices and careful concern, I could not achieve any meaningful progress.

I also would like to thank my colleagues of the T30g group. At first for ex-members Dr. Markus Lischka, Dr. Christian Bach and Dr. Ata Roudgar, where you are with my best wishes. For Dr. Areezo Dianat, Thomas Markert, Christian Mosch and Dr. Yoshihiro Gohda, I hope better understanding in both science and personal.

Especially, I would like to appreciate German Academic Exchange Service (DAAD) for the financial support during last 3 years (2001-2004). I gratitude for the members of Referat 424 to the efforts to handle my personal inquiries. The benefit of DAAD covered more than economic province, it allowed me to concentrate on my research with better understanding of Germany. I could not forget my thanks to Prof. Dr. Harald Friedrich and Prof. Dr. Wilhelm Brenig, they did kindly write the recommendation letters. I acknowledge the financial support by the Wilhelm und Else Heraeus-Stiftung for attending the DPG-Frühjahrstagungen 2003 and 2004.

I thanks Prof. Dr. Karl-Heinz Leist who charges with the exchange program between Sogang University (Seoul, Republic of Korea) and Technische Universität München. I had been introduced to Germany and Technische Universität München by the program. I expect many successes in the program also in the future.

I devote my work to my wife Jeongae Kim for her sincerity and sacrifice. All the time, she is my most important felicity.

München — Sung Sakong
May 2005

Contents

List of Figures

List of Tables

Chapter 1

Introduction

The heterogeneous catalytic reaction of gaseous molecules over metal surfaces is an important industrial mechanism. Worldwide, more than 90% of all everyday chemicals are usually produced by one or more industrial catalytic reactions. The human life without the support of catalysts almost would not be possible in the mass production ages.

The most important properties of a catalyst can be characterized as reactivity and selectivity. A heterogeneous catalyst increases the reactivity by supplying reaction paths with a lower energetic cost. The control of the reaction path can also maximize the amount of target products by improving the selectivity. An efficient catalyst has apparently economic advantages, lowering the costs and enlarging the gain. Recently, moreover, catalysts extend its usage to reduce pollution by converting hazardous waste to less harmful materials.

Historically the study of catalysis had been started in 1830s, but considerable progress was only made in 20th century. The concept of catalysis as we know it today had been established by W. Ostwald in 1901. The development of catalysts is still mainly dependent on the trial and error approach. For example, the industrial ion-oxide catalyst for the synthesis of ammonia was found after testing around 20 thousands different catalysts. A systematic improvement of catalysts became only possible after gaining a microscopic understanding of catalytic reactions, as for example employed in the development of a improved steam-reforming catalyst based on a Au/Ni alloy [1].

The advent of the ultrahigh vacuum (UHV) technology and precise analyzing methods allows to perform adsorption experiments on well-characterized clean surfaces. In recent years, due to the progress in surface sensitive techniques detailed pictures of surface reactions are revealed. The chemical identity, binding energy and geometric configuration are precisely determined by modern surface science techniques from low energy electron diffraction (LEED) to near edge X-ray adsorption fine structure (NEXAFS). Chemical reactions are observed, e.g., by the technique of temperature

programmed desorption (TPD). The field of modern surface science is characterized by a wealth of microscopic experimental information [2].

Modern *ab initio* calculation methods opened the door to the "virtual chemistry lab" [3]. The progress of the first-principles technology allows to handle a variety of gas-surface systems without any empirical parameters [2, 4]. The widely adopted *ab initio* density functional theory has proved its reliability for dealing with surface problems. Nowadays, the improvement of the accuracy of first principle calculations has led to the capability to predict properties of surface systems. Thus theory and experiment can be abreast in the field of gas-surface reactions. At the same time, the enhancement of computation power also allows the virtual chemistry lab to treat much larger and complicated systems.

Beyond simple molecules larger molecules such as ammonia or organic molecules on rough surfaces can be considered. Even though the system are getting closer to realistic ones, however, still there are differences to a real catalyst which consists of a high concentration of steps and facet edges. On the other hand catalytic surface reactions may not only be related to defect structures, but more importantly to general electronic properties. Then the restricted research of well-defined low indexed surfaces is also valuable for understanding real catalysts in both experiment and theory. In this thesis, the catalytic reaction of methanol on copper surfaces will be theoretically discussed.

Methanol is one of the major bulk chemicals with an annual product volume of 21.8 million tons (year 2000) [5], and the demand is still increasing today. Methanol has enormous usages for many different kinds of purposes such as converting various aldehydes, acids, ethers, olefins and so on. Moreover, recently, it has been suggested as an proton provider to fuel cell engines [6]. The next generation of direct methanol fuel cell is a strong candidate for a clean energy source without any production of toxic materials. Therefore both the synthesis and conversion of methanol are important in the industrial field.

The synthesis and reforming of methanol are in general based on catalytic processes on metals. The synthesis in the industrial scale uses heterogeneous catalysts, e.g. commercial binary Cu/ZnO catalysts, with natural gases as source materials. Moreover, in the steam reforming of methanol Cu/ZnO catalyst plays also a dominant role, in particular for the dehydrogenation to formaldehyde. However, recently it was claimed that Rh/ZnO has a better selectivity to reduce the poisonous CO production in the fuel cell. Hence in the study of Cu based catalysts, the reduction of CO production turned out to be one of the most interesting subjects.

In spite of the tremendous use and importance of methanol reactions on Cu based catalyst, the microscopic understanding is still poor. Surprisingly, an industrial level formaldehyde production from methanol is simply described as *exposure of methanol over hot Cu*. Therefore the theoretical study of methanol reactions over Cu catalysts in a systematic way helps to develop a microscopic picture of catalytic reactions.

Recent studies of binary Cu/ZnO catalysts reported that the active site for the synthesis of methanol is metallic Cu [7, 8]. This was derived from the fact that the reactivity was proportional to the size of the Cu area. The epitaxial growth of Cu cluster over Zn-terminated ZnO leads to bulk Cu crystals even under low coverage [9–

11]. The lattice mismatch between Cu and ZnO is 21%, therefore the strain effect will be dominant for small Cu clusters. Thus, the study of strain effects in methanol reactions over pure copper surfaces is relevant also for the understanding of the reactivity of commercial catalysts. It is also expected that the microscopic study of reactions leads to an improvement of the efficiency of real catalysts.

In 1978, very influential experiments to determine the methanol oxidation pathways over copper surface had been performed by Wachs and Madix [12]. Numerous experiments and theoretical approaches proved their validity in the last 26 years. In this thesis the main purpose is to rebuild the reaction pathways of Wachs and Madix theoretically and to interpret the energetics of the theoretical reaction pathways. In Chap. 2 the theoretical backgrounds will be reviewed, and in Chap. 3 the molecular properties of the reaction intermediates will be precisely studied. In Chap. 4 strain effects present in real catalysts will be addressed by slab calculations. Finally, in Chap. 5 reaction pathways and their energetics will be determined and discussed.

Chapter 2

Theoretical backgrounds

In the past century, the quantum theory of many-body systems has been intensively studied in order to accurately solve the non-relativistic many particle Schrödinger equation which includes the Coulomb interactions of nuclei and electrons in solid. The determination of total energies and the corresponding wave functions of the system represents a rather complicated problem; its solution cannot be acquired in a straightforward way. Successful numerical techniques were established in two major fields, wave function and electron density methods in chemistry and physics, respectively. Commonly, the implementation of both methods is based on the simplification of the Schrödinger equation by the Born-Oppenheimer approximation [13].

This approximation simplifies the system in terms of electrons moving in an external potential. The large mass mismatch of nuclei and electron allows the consideration of the ionic coordinates as static parameters. Thus one can assume that the electron distribution finds instantly its minimum energy configuration for each ionic configuration, while the nuclei respond very slowly to the change of the electron distribution. However, unfortunately, this useful approach does not cover all interesting physical phenomena, especially not ionic-motion-induced electron excitations, such as for example the Ziman effect [14].

Historically, chemists have treated reactions at surfaces earlier than physicists by using wave function based quantum chemistry methods. The methods are based on the expansion of the wave function in terms of Slater determinants. Many quantum chemistry methods for reactions on finite clusters have been developed to improve the quality of the description. In spite of a brilliant improvement of the basis set and correlation description, these methods still have critical problems. A proper selection of the basis set is inevitable for a comprehensible description of a given system. Furthermore, although the accuracy of wave function calculations can be improved by increasing the number of basis functions, the cost for accuracy becomes easily enormous in larger system.

Here we use an alternative method to solve the electronic structure problem, *ab*

initio density functional theory (DFT) proposed by Hohenberg and Kohn in 1964 [15]. This method, together with the improvement in computer power, has allowed the treatment of extremely complex molecular and catalytic systems. Nowadays, finally, DFT calculations satisfy also chemical accuracy due to the development of the generalized gradient approximation for exchange-correlation. The big success of DFT and its contribution to the scientific progress resulted in the Nobel prize for chemistry in 1998 for Walter Kohn.

2.1 Density functional theory

DFT is based on the famous Hohenberg-Kohn theorem [15]: *"The ground-state density $n(\mathbf{r})$ of a system of interacting electrons in an external potential uniquely determines this potential."*. DFT can be regarded as a revised successor of Thomas-Fermi theory [16–18]. The main idea of DFT is the substitution of the multi-dimensional wave function $\Psi(\mathbf{r}_1, \mathbf{r}_2, \cdots, \mathbf{r}_N)$ of N interacting electrons by the simple electron density $n(\mathbf{r})$ which is a function of three-dimensional coordinates. The implementation of this idea via effective one-particle Schrödinger equations had been developed by Kohn and Sham [19].

2.1.1 Kohn-Sham equations

Consider the time-independent, non-relativistic Schrödinger equation for the wave function Ψ of N interacting electrons,

$$E\Psi = \hat{H}\Psi = (\hat{T} + \hat{V} + \hat{V}_{\text{ext}})\Psi \tag{2.1}$$

where the Hamilton operator of the system consists of the kinetic energy operator $\hat{T}$, the electron-electron interaction potential $\hat{V}$ and the external potential $\hat{V}_{\text{ext}}$. The external potential $\hat{V}_{\text{ext}}$ includes the Coulomb interaction between electron and nuclei and external fields. In this equation the electronic and ionic motion are decoupled, electron-phonon excitations are excluded and nuclei coordinates are considered as a parameter.

Following the Hohenberg-Kohn theorem, there is an one-to-one correspondence between the electron ground-state density and the many-body wave function of interacting electrons. This means that the ground-state electron density is uniquely determined by $\hat{V}_{\text{ext}}$,

$$n(\mathbf{r}) \mapsto |\Psi[n]\rangle \text{ and } n(\mathbf{r}) \mapsto V_{\text{ext}}(\mathbf{r}). \tag{2.2}$$

The ground state solution of the Schrödinger equation is derived through the Rayleigh-Ritz variational principle [20–22] by minimizing the expectation value of the total energy. The iterative cycle of minimization will be continued until self-consistency is accomplished with respect to a trial wave function [23]. The minimization using the electron-density reaches the ground state energy via the relations in Eq. (2.2),

$$E_0 = \min_{\Psi} \langle \Psi | T + V + V_{\text{ext}} | \Psi \rangle = \min_{n(\mathbf{r})} E[n(\mathbf{r})] \tag{2.3}$$

where

$$E[n] = T[n] + V_{\mathrm{H}}[n] + E_{\mathrm{xc}}[n] + V_{\mathrm{ext}}[n]. \tag{2.4}$$

$T[n]$ is the kinetic energy functional for non-interacting electrons and $V_{\mathrm{ext}}[n]$ is the functional of the external potential. The Hartree energy $V_{\mathrm{H}}[n]$ which describes the classical Coulomb energy of electrons is given by

$$V_{\mathrm{H}}[n] = \frac{1}{2}\int d\mathbf{r}d\mathbf{r}' \frac{\mathrm{e}^2}{4\pi\epsilon_0}\frac{n(\mathbf{r})n(\mathbf{r}')}{|\mathbf{r}-\mathbf{r}'|}. \tag{2.5}$$

The total energy includes a purely quantum mechanical interaction, the so-called exchange-correlation energy $E_{\mathrm{xc}}[n]$. It is usually of the order of 1 eV per electron. The improvement of the accuracy of DFT is strongly dependent on the proper determination of the exchange-correlation energy. The exchange-correlation functional is not known in general. It is an universal functional that depends only on the electron-density itself.

The electron-density of N independent electrons is expressed as

$$n(\mathbf{r}) = \sum_{i=1}^{N} |\varphi_i(\mathbf{r})|^2 . \tag{2.6}$$

The basis electron function $\varphi_i(\mathbf{r})$ are selected to be orthonormal to each other. The variation of the energy functional $E[n]$ with the orthonormality constraint $\langle\varphi_i|\varphi_j\rangle = \delta_{ij}$ leads to a set of self-consistent one-electron equations, namely the Kohn-Sham equations [19], which are equivalent to the many-electron problem:

$$\left[-\frac{\hbar^2}{2m}\nabla^2 + V_{\mathrm{eff}}(\mathbf{r})\right]\varphi_i(\mathbf{r}) = \varepsilon_i(\mathbf{r})\varphi_i(\mathbf{r}), \tag{2.7}$$

where the effective potential V_{eff} is given by

$$V_{\mathrm{eff}}(\mathbf{r}) = V_{\mathrm{H}}(\mathbf{r}) + V_{\mathrm{xc}}(\mathbf{r}) + V_{\mathrm{ext}}(\mathbf{r}). \tag{2.8}$$

The exchange-correlation potential $V_{\mathrm{xc}}(\mathbf{r})$ is given by the functional derivative of the exchange-correlation energy with respect to the electron density,

$$V_{\mathrm{xc}}(\mathbf{r}) = \frac{\delta E_{\mathrm{xc}}[n(\mathbf{r})]}{\delta n(\mathbf{r})}. \tag{2.9}$$

For a correct exchange-correlation energy, the potential given by the functional derivative would give an exact description of exchange and correlation. The set of wave functions φ_i and Kohn-Sham eigenvalues ε_i is determined by solving the Kohn-Sahm equations self-consistently. In the first iteration an initially guessed charge density is inserted in the Hartree and exchange-correlation terms of the Kohn-Sahm equations. In the following iterations, the new electron density is generated by the Kohn-Sham eigenstates as described in Eq. (2.6) which determines the effective potential for the next iteration. The self-consistency cycle is repeated until the convergence of the charge density which then also yields the ground state energy. The procedure is accelerated

by mixing new and old charge densities. Advanced mixing technique, such as the modified Broyden's method [24], can significantly speed up the convergence by utilizing more than just the charge density of the electronic step and damping spurious Fourier components of the intermediate charge density.

The Kohn-Sham equations represent a mapping of the many-body problem of interacting electrons onto coupled one-electron equations with an effective potential. However, it leads to the double-counting of electron-electron interactions, when the sum of single-particle Kohn-Sham eigenvalues is considered in the total energy. The ground state energy of the system will be exact by removing the over-counted energies as

$$E[n] = \sum_{i=1}^{N} \varepsilon_i - \frac{1}{2} \int d\mathbf{r}\, V_{\mathrm{H}}(\mathbf{r}) n(\mathbf{r}) - \int d\mathbf{r}\, V_{\mathrm{xc}}(\mathbf{r}) n(\mathbf{r}) + E_{\mathrm{xc}}[n]. \tag{2.10}$$

Therefore the eigenvalues of the Kohn-Sham equation are not the energies of single-electron states but the derivatives of the total energy with respect to the occupation numbers of these states [25].

2.1.2 Exchange-correlation functionals

The universal functional of the exchange-correlation energy $E_{\mathrm{xc}}[n]$ is not known in close and analytic form yet. There is a simple approximation for the exchange-correlation energy functional, namely the local density approximation (LDA) [19]. The LDA assumption is that the exchange-correlation energy per electron at a point $\mathbf{r}$ in the electron gas $\varepsilon_{\mathrm{xc}}(\mathbf{r})$ is equal to those of a homogeneous electron gas $\varepsilon_{\mathrm{xc}}^{\mathrm{LDA}}(\mathbf{r})$ with the same density $n(\mathbf{r})$: thus the exchange-correlation functional is approximated as

$$E_{\mathrm{xc}}[n] = \int d\mathbf{r}\, n(\mathbf{r}) \varepsilon_{\mathrm{xc}}(n(\mathbf{r})). \tag{2.11}$$

The LDA exchange-correlation potential is taken as a purely local functional, depending only on the density at position $\mathbf{r}$. Then the LDA exchange-correlation potential in Eq. (2.9) is simplified as

$$V_{\mathrm{xc}}^{\mathrm{LDA}}(\mathbf{r}) = \frac{\partial}{\partial n} n \varepsilon_{\mathrm{xc}}(n) \bigg|_{n=n(\mathbf{r})}. \tag{2.12}$$

The LDA exchange-correlation itself can be obtained using an interpolation scheme between analytic asymptotic behaviors and intermediate results based on quantum Monte Carlo calculations of the homogeneous electron gas [26]. Furthermore, the LDA satisfies important sum rules for the electron-hole pairing. Surprisingly, in spite of the inexact representation of the inhomogeneous electron gas, LDA has been successful for various bulk and surface problems [23]. LDA yields relatively reliable lattice constants and ionic configurations, but in fact the reasons for this good accuracy are not fully understood.

LDA calculations are not sufficiently accurate for gas-phase and surface chemical reactions [2]. Usually LDA overestimates chemical binding energies, the binding energies and cohesive energies are too large compared to experiment. The attempts to

improve DFT by using a Taylor expansion of the exchange-correlation energy $\varepsilon_{xc}[n]$ in the density had not been successful since it violates the sum rule for the exchange-correlation hole [2, 27, 28]. Only in the so-called generalized gradient approximation (GGA) the problem has been overcome [29–32], where the GGA exchange-correlation energy is expressed as

$$E_{\mathrm{xc}}[n] = \int d\mathbf{r}\, n(\mathbf{r})\varepsilon_{\mathrm{xc}}(n(\mathbf{r}), |\nabla n(\mathbf{r})|), \tag{2.13}$$

which includes the gradient of the density $|\nabla n(\mathbf{r})|$. Chemical binding energies are described much better in GGA. For many chemical reactions DFT calculations using GGA, finally, achieved chemical accuracy [2].

The search for finding better exchange-correlation functionals has not been finished. In spite of the success of the functional of Perdew and Wang (PW91) [31] and Perdew-Burke-Ernzerhof (PBE) [32], still there are a number of failures in GGA. These include [2]: (*i*) improper description of van der Waals forces, (*ii*) insufficient electron affinities of negative ions, (*iii*) underestimation of cohesive energies, (*iv*) underestimation of band gaps, (*v*) wrong long-range of the effective one-particle potential at large distances, (*vi*) erroneous representation of anti-ferromagnetic insulators as metals.

Besides the effort to improve the GGA functional itself, e.g. the revised version of PBE (RPBE) [33], the attempts of including exact exchange or considering meta-GGA's have led to a better accuracy. However, in spite of the better description of exchange-correlation, computational power economics strongly recommends calculations using efficient GGA schemes. All calculations reported in this thesis have been evaluated using the GGA in the form proposed by Perdew and Wang (PW91) [31].

2.1.3 Plane wave basis sets with special k-points

In the previous sections we reviewed the way to map an interacting many-body system into effective one-electron problems. However, for solid systems the solution of Kohn-Sham equations still requires to handle the dynamics of in principle an infinite number of noninteracting electrons in a static high-dimensional potential.

The periodicity of a solid crystal can be utilized employing Bloch's theorem to reduce the infinite number of electrons to a finite number of electrons within a single primitive unit cell [34]. The eigenvalues of these so called Bloch functions correspond to discretely spaced band energies. The electron wave functions are expressed as the product of a cell-periodic part and a plane-wave-like part. Usually the basis functions are selected to be plane waves, hence the electronic wave functions are

$$\varphi_{\mathbf{k},i}(\mathbf{r}) = \sum_{\mathbf{G}} c_{i,\mathbf{k}+\mathbf{G}} e^{i(\mathbf{k}+\mathbf{G})\cdot\mathbf{r}}, \tag{2.14}$$

where $\mathbf{G}$ represents the reciprocal lattice vectors and $\mathbf{k}$ is restricted to the first Brillouin zone and i is the band index [34]. The electronic wave functions at each $\mathbf{k}$ can be represented in terms of a *discrete* plane wave basis set. Thus, by Bloch's theorem, the electrostatic potential can be constructed by the contribution of occupied electronic states at each $\mathbf{k}$ point, where the $\mathbf{k}$ is in the first Brillouin zone.

The electronic wave functions will be almost identical when **k** points are very close together. Hence the electronic wave function over a region of **k** space can be represented by the wave function at a single **k** point. Hence the calculation of the electrostatic potential requires only a finite number of electronic states at a finite number of **k** points, and this electrostatic potential together with the external potential then determines the total energy of the system. Thus the total energy of solid systems per unit cell is expressed as

$$E = \langle H \rangle = \frac{1}{V} \sum_i \int_V d\mathbf{k}\, H_i(\mathbf{k}) f(\varepsilon_i(\mathbf{k})) \approx \frac{1}{V} \sum_{\{\mathbf{k}\}} H_i(\mathbf{k}) f(\varepsilon_i(\mathbf{k})), \tag{2.15}$$

where the volume of the unit cell is V and $f(\varepsilon_i(\mathbf{k}))$ is the density of electronic states at a given band i and point **k**. The integral over the first Brillouin zone and sum over band indices are replaced by a sum over a special kpoint set $\{\mathbf{k}\}$. The most common way to select special **k** points is described by Monkhorst and Pack [35]. This set corresponds simply to an equispaced grid of **k** points. For accurate calculations of metals, more **k** points than for insulator or semiconductor are required to describe the Fermi surface precisely. To improve the accuracy of the discrete approximation to the Brillouin zone integration, broadening methods are employed. The broadening is controlled by the temperature parameter $\sigma = k_\mathrm{B}T$. The value of σ has to be carefully selected in the calculation of Cu, since its d-electron structure is fully occupied and the upper bound of d-electronic structure is located lower than the Fermi energy which creates a low density of states at the Fermi energy. To avoid any spurious contributions, σ must be small enough. First order Methfessel-Paxton smearing [36] and the linear tetrahedron method [37] are used for the calculations in this thesis.

In principle, at each **k** point, an infinite plane wave basis set is required to expand the electronic wave function. However, for practical reasons, the number of plane wave basis is controlled by the energy cutoff,

$$E_\mathrm{cutoff} = \max_{\mathbf{G}} \left[\frac{\hbar^2}{2m} |\mathbf{k} + \mathbf{G}|^2 \right]. \tag{2.16}$$

The accuracy of this approximation will be simply improved by enlarging E_cutoff.

By employing Bloch's theorem and a plane wave basis set, the Kohn-Sham equations Eq. (2.7) are transformed to

$$\sum_{\mathbf{G}'} \left[\frac{\hbar^2}{2m} |\mathbf{k} + \mathbf{G}|^2 \delta_{\mathbf{G},\mathbf{G}'} + V_\mathrm{eff}(\mathbf{G} - \mathbf{G}') \right] c_{i,\mathbf{k}+\mathbf{G}'} = \varepsilon_i c_{i,\mathbf{k}+\mathbf{G}}, \tag{2.17}$$

where the kinetic energy is diagonal and $V_\mathrm{eff}(\mathbf{G} - \mathbf{G}')$ is the Fourier transform of the effective potential. The eigenvalues ε_i and the plain wave coefficients $c_{i,\mathbf{k}+\mathbf{G}}$ are obtained by diagonalizing the Hamiltonian. The size of the Hamiltonian matrix is determined by the energy cutoff. Modern iterative methods find the electronic states that minimizes the energy functional with avoiding direct matrix diagonalization [23, 38].

The implementation of the Kohn-Sham equations in the Vienna *ab initio* simulation package (VASP) [39–42] is organized as follows: The wave function is expanded in plane

waves on a finite **k** point mesh, and the resulting Hamiltonian is iteratively solved either by a sequential conjugate gradient (CG) minimization [43, 44] or by a residual minimization method (RMM) [38, 45] using a direct inversion in the iterative subspace.

Using a plane wave basis set also offers the advantage that the force $\mathbf{F}_I$ on an ion at position $\mathbf{R}_I$ can be computed by the Hellmann-Feynman theorem [46],

$$\mathbf{F}_I = -\frac{dE}{d\mathbf{R}_I} = -\frac{\partial E}{\partial \mathbf{R}_I} \tag{2.18}$$

as the derivatives of the basis set with respect to the position of the ion are vanishing.

2.1.4 Pseudopotential approximation

Although Bloch's theorem allows to expand the wave functions in a discrete set of plane wave basis set, it is not appropriate to describe the tightly bounded core electrons which have rapidly oscillating nodes by plane waves. To reproduce the details of the electronic wave functions near the core in all-electron calculations requires a prohibitively large size of the plane wave basis set. The decomposition of the wave function in different basis sets for the core and the interstitial regions helps to reduce the size of the plane wave basis. The first method using such a decomposition was the augmented plane waves (APW) method within the *muffin-tin* approximation [47]. The problem of the APW, a large computational cost, has been partially solved by the concept of the linearized augmented plane waves (LAPW) by Andersen [48]: the wave functions of the core regions are described by a linear combination of radial expansions and its first energy derivative expansions. For the interstitial region, commonly APW and LAPW use a plane wave basis set. All electron methods, such as the most recently developed full-potential LAPW [49], provide a very accurate description of the system, but the computational cost is very high for the description of transition metals and first-row non-metal systems.

The computational effort is, of course, increased by including more electrons in the DFT calculations. The construction of pseudopotentials reduces the number of electrons by replacing the effect of the core electrons by an effective potential. As a result, the use of pseudopotentials reduces the computational effort considerably. The idea of pseudopotentials comes from the fact that most of the chemical properties of physical systems are much more dependent on the valence electrons than on the localized core electrons and that core electrons hardly take part in any chemical reactions [2, 50]. Replacing core electrons by an ionic potential leads to a pseudopotential that acts on a set of pseudo wave functions. A pseudo wave function and the corresponding potential are illustrated in Fig. 2.1. Outside the core region the pseudopotential and the pseudo wave function are identical to the all-electron potential and wave function. In the core region, the radial nodes of the wave function are removed while maintaining the norm of the wave functions and the scattering properties.

The general form of norm-conserving pseudopotentials is given by

$$V_{\text{pseudo}}(\mathbf{r}) = \sum_{l,m} |Y_{lm}\rangle \, V_l(\mathbf{r}) \, \langle Y_{lm}|. \tag{2.19}$$

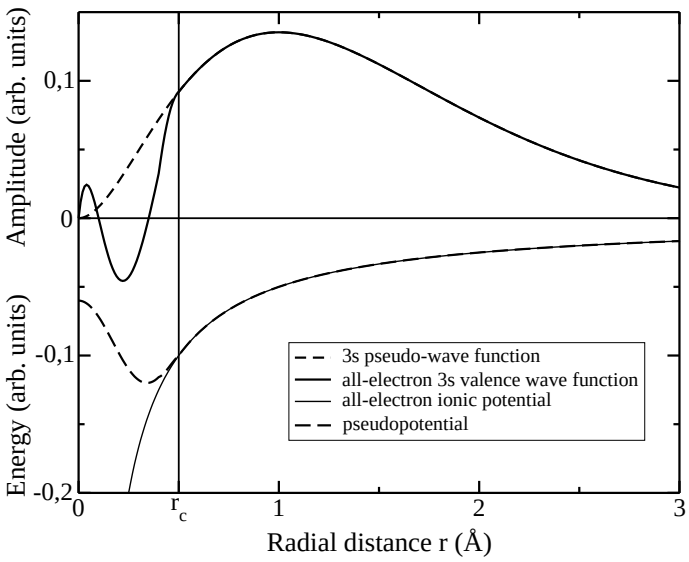

Figure 2.1: Schematic illustration of the difference between the all-electron and pseudo $3s$ wave function and their corresponding potentials [2].

where $|Y_{lm}\rangle$ denotes spherical harmonics. It is called semi-local since it is local in the radial part and non-local in the angular part. The implementation of a plane wave basis in the pseudopotential approach was first done by Troullier and Martins [51] and Rappe *et al.* [52]. The accuracy of the pseudopotential calculations is only determined by the energy convergence of the valence electrons, since core electrons are not directly considered.

The development of Vanderbilt or ultrasoft pseudopotentials (USPP) by David Vanderbilt [53] represents a significant improvement for the pseudopotential approximation. In the generation of USPP, in contrast to the traditional pseudopotential approach, the norm-conserving constraint has been removed. However, this ansatz violates charge conservation. In order to recover the correct charge density, overlap matrix derived augmentation charges are introduced in the core region. The electron density is subdivided in a delocalized smooth part and a localized hard part in the core regions. The USPP allows an accurate description of many systems with a much lower energy cutoff, thus leading to a significantly reduced computational effort.

An alternative approach to disentangled core and valence states is known as the projector augmented-wave (PAW) method [54, 55]. The idea of the PAW method is based on that the all-electron wave functions are derived by pseudo wave functions using a linear transform. This linear transform is uniquely determined by a sum of local, atom-centered contributions. Each local contributions acts only within some augmentation region enclosing the respective atom. The augmentation in the core region is given by the overlap with localized projector functions, which is consistent with the frozen-core approximation [2, 54]

PAW is an all-electron calculation, however it only requires the computational effort of a pseudopotential calculation. The frozen core constraint of the PAW method makes possible the computational efficiency of ultrasoft pseudopotentials with preserving the

accuracy of all-electron calculations. Interestingly, the difference between PAW and USPP is just based on one-center terms [55], which leads to the high efficiency of the PAW method. It exhibits a higher accuracy than the USPP method when the system depends on the core electrons, e.g. in the case of oxygen atoms. In this work, however, we will remain within the framework of USPP for all DFT calculations.

2.1.5 Supercell approach

In solid state physics, structures that break the crystalline symmetry exhibit many interesting physical properties. Also in theoretical methods requiring three-dimensional periodicity symmetry breaking structures can be treated within the concept of Bloch's theorem using the supercell approach. The supercell includes the symmetry breaking structure surrounded by a bulk crystal region, and periodicity is reproduced by repeating the supercell structure. Therefore the system is described as a bulk with an array of symmetry breaking structures. The size of the supercell has to be large enough so that the interactions between defects which are located in neighboring unit cell become negligible.

In the case of surfaces, the three-dimensional crystal periodicity is broken in the direction of the surface normal z. The ideal surface system consists of a semi-infinite bulk region and a semi-infinite vacuum region along the z axis with preserving the periodicity in the x-y plane. In the so-called slab approach, however, the semi-infinite metal is replaced by a slab with a finite number of atomic layers. In this approach, a two-dimensional lattice is obtained where the periodicity is given by the surface unit cell. To recover three-dimensional periodicity, the slab is now repeated in the z direction by adding a sufficiently large region of vacuum in between slabs. The size of the vacuum region and the number of atomic layers are chosen such that the surface energy and workfunction of the slab are converged, i.e. they do not change when the size of the layers is enlarged. For low index metal surfaces, four or five layers slab and at least 10 Å of vacuum layer are already sufficient to fulfill the convergence of surface energy. For example, the convergence of the workfunction for Cu(100) requires a five layer Cu slab with 12 Å of vacuum layer.

The size of the unit cell in lateral direction depends on the particular problem. When single molecular or atomic adsorption is considered, it must be large enough to remove the interactions between adsorbates in neighboring unit cell. The lateral size of the supercell also depends on the considered coverage of the adsorbates.

2.2 Physical properties

The improvements in the computer powers made the treatment of realistic systems by DFT methods possible. In this section, the numerical setup and the computational treatment of adsorbate systems will be addressed. Moreover, the general concepts and physical properties for surface adsorption and surface reactions will be briefly described.

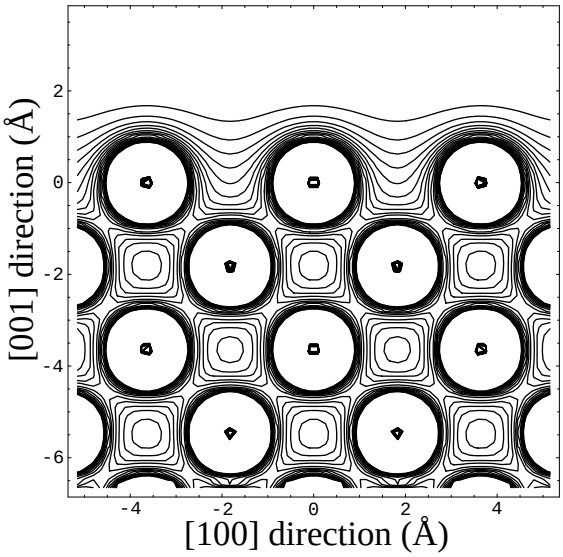

Figure 2.2: Electron density of a Cu(001) surface along a (010) plane demonstrating electron smoothing at a metal surface [2].

2.2.1 Geometry relaxations

The construction of slabs requires the equilibrium lattice constant from bulk calculations. The common way to determine the lattice constant of a bulk crystal is the interpolation of DFT cohesive energies as a function of the lattice constant. The direct energy minimization requiring the change of the unit cell volume is thus avoided, which would lead to additional correction forces arising from the stress tensor, namely Pulay stress. DFT bulk energies with the same energy cutoff and same number of **k** points are fitted to the Birch-Murnaghan equation [56, 57]

$$E(V) = E(V_0) + \frac{B_0 V}{B_0'(B_0'-1)}\left[B_0'\left(1-\frac{V_0}{V}\right) + \left(\frac{V_0}{V}\right)^{B_0'} - 1\right], \tag{2.20}$$

where V is the unit cell volume of the strained crystal and B_0 and B_0' are the bulk modulus and its pressure derivative at the equilibrium volume V_0. DFT lattice constants are usually close to experimental values, but but often with asystematical difference. LDA lattice constants are usually smaller than experimental ones while GGA ones are larger. This simply reflects the overestimation of cohesive energies in the LDA and their underestimation in the GGA. The optimization of the VASP parameters is in general performed in bulk calculations. The lattice constant, the optimized energy cutoff and the k-point selection are determined in this step.

A substrate is constructed by stacking atomic layers with the bulk lattice constant. For close packed (111) and (100) surfaces of face centered cubic (fcc) crystals, 4 or 5 layers are already sufficient for converged result. The rather open surface (110) requires also only 5 atomic layers. However, the complex (210) surface already demands 11 atomic layers for converged results. Since the slabs are separated in z-direction so that there is no interaction, only one k-point along this direction is required. However, the

ideal bulk positions are no longer stable at a surface. At the surface of a solid the electronic structure and charge density are strongly modified. Considering the charge density of metal surfaces, the surface electron distribution is much smoother than in the bulk. This Smoluchowski smoothing [58] leads to a rather uniform distribution of the charge density thus lowering the kinetic energy of the surface electrons as illustrated in Fig. 2.2. As a result of the surface charge density redistribution, the ion cores experience inward forces to the bulk. For a realistic slab model, the surface ion relaxation is included by computing the ionic forces by the Hellmann-Feynman theorem. In Cu substrates, the relaxation of the upper-most ions affects the ion positions by only a few hundredth of an Angstrom. The shift of the second layer atoms is generally smaller than in the first layer.

Adsorption systems are modeled by locating the adsorbates on one side of the slab. The atoms of the bottom layers of the slab are at their bulk position. This slightly improves the description of the subsurface layers on the adsorbate side. In the case of the adsorption of massive molecules the adsorbate induced surface relaxation must also be accounted. For example, the adsorption energy of methoxy (CH_3O) on the hollow site of Cu(100) is enlarged by 0.03 eV by surface relaxation, while atomic hydrogen adsorption leads to no ionic rearrangement. DFT adsorption geometries can be compared to results from low energy electron diffraction (LEED) and near edge X-ray adsorption fine structure (NEXAFS) experiments, and to scanning tunneling microscope (STM) images. For many systems, DFT yields reliable results for adsorption geometries, surface reconstructions and binding energies.

2.2.2 Adsorption energies and activation barriers

The DFT total energy $E[n]$ is used to determine the adsorption energy E_{ads} which is defined as the total energy difference between the adsorbate system and the sum of the clean substrate and the gas-phase atom or molecule. In molecular non-dissociative adsorption, the adsorption energy is defined as

$$E_{\mathrm{ads}} = E_{\mathrm{adsorbate}} - (E_{\mathrm{slab}} + E_{\mathrm{mol}}). \tag{2.21}$$

For many closed-shell molecules, it corresponds simply to the physisorption energy, and in most case this will be underestimated in GGA. In the case of open-shell molecules, e.g. CO, Eq. (2.21) gives the chemisorption energy the molecule. However, for the dissociative adsorption, e.g. of hydrogen, the adsorption energy per atom includes the bond breaking of the gas-phase molecule,

$$E_{\mathrm{ads}} = E_{\mathrm{slab+H}} - (E_{\mathrm{slab}} + \frac{1}{2}E_{\mathrm{H_2}}). \tag{2.22}$$

The adsorption energy is used as a parameter of the reactivity. It can also describe the energy state of a reaction intermediates, then the reference energy for the reaction must be defined as the total energy of the reactants. The reference energy for methanol oxidation, for example, is given by,

$$E_{\mathrm{ref}} = E_{\mathrm{slab}} + \mathrm{n}E_{\mathrm{CH_3OH}} \tag{2.23}$$

where E_{CH_3OH} denotes the energy of gaseous methanol and n is the number of methanol molecules in the supercell. The adsorption energy is one of the most important results obtained by DFT calculations. It can be compared to the binding energy determined by thermal desorption spectroscopy (TDS) experiments. However, the DFT adsorption energy does not correspond to the Helmholtz free energy since it does not include any entropic effects [59]. This can be corrected by considering the energy of vibrational excitations after diagonalizing the corresponding Hamiltonian matrix. However, usually the entropic contributions are small so that they can be neglected.

Surface reactions can be fully described by molecular dynamics (MD) simulations. However, the adiabatic potential energy surface (PES) approach in terms of DFT total energies $E(\{\mathbf{R}_I\})$ as a function of the ionic coordinates also leads to valuable results with lower computational effort. In the simulation of adsorption processes often the substrate is considered rigid, since the relaxations are small during the reaction. However, for phonon-supported adsorption systems, e.g. hydrogen over Si, the consideration of substrate relaxations are inevitable for a correct description of the adsorption process.

From the PES, important informations about the adsorption/desorption dynamics can be derived. In the case of diatomic adsorption, one usually considers two-dimensional cuts through the six-dimensional configuration space, so-called elbow potentials for fixed molecular orientation and lateral center of mass coordinates.

In addition, the associative desorption barrier E_{des} along a particular reaction path can be derived from the dissociative adsorption barrier via

$$E_{\mathrm{des}} = E_{\mathrm{b}} - (E_{\mathrm{ads}}^{\mathrm{H}^1} + E_{\mathrm{ads}}^{\mathrm{H}^2}) \tag{2.24}$$

where inequivalent atomic adsorptions are assumed.

Elbow plots of the PES therefore help in identifying pathways, barrier regions and transition states along the reaction path. However, they always give a restricted subset of the true multi-dimensional PES and the true dynamics of the molecular adsorption process.

2.2.3 Density of states

The chemical nature of a static configurations can be analyzed by looking at the density of states (DOS). This quantity is given by

$$N(E) = \sum_{i=1}^{\infty} \delta(E - \varepsilon_i), \tag{2.25}$$

where the sum extends over all eigenstates of the appropriate one-particle Hamiltonian, for example the Kohn-Sham Hamiltonian Eq. (2.7). As mentioned in Sec. 2.1.3, only a finite number of eigenstates can be calculated at a given set of $\mathbf{k}$ points. Therefore, a continuous distribution of the DOS is only acquired by smearing. In the consideration of chemical bond formation and breaking we are interested in the atomic orbitals or hybrids which take part in the bonding. In surface problems, of course, the electronic

structure of the interacting surface atoms is also important. This analysis can be done using the concept of the projected DOS as defined by [59–61]

$$n_\alpha(E) = \sum_{i=1}^{\infty} |\langle \phi_\alpha | \varphi_i \rangle|^2 \, \delta(E - \varepsilon_i), \tag{2.26}$$

where ϕ_α is a properly chosen localized function. In a plane wave basis the wave function is just projected onto the respective atomic s, p, d orbitals. The decomposition into atomic orbitals can lead to the understanding of bonding and anti-bonding contributions for a particular reaction.

However, the Kohn-Sahm eigenvalues ε_i are not the true energy eigenvalues of single electrons. It rather corresponds to the eigenstates of non-interacting quasi-particles. Thus using the density of states as an excitation energy or single-electron levels has no theoretical justification. However, the common practice and the errors introduced in such an approach are usually acceptable [62]. The application of the DFT-DOS spectrum for describing chemical bond formation and breaking have been extraordinarily successful.

2.2.4 Charge density analysis

The charge density is one of the quantities directly acquired from DFT calculations. However, the charge density itself is somewhat hard to analyze. A band decomposed charge density will be helpful to understand chemical bonds, but the much simpler picture of electron density differences gives also valuable results. It is defined as the electron density difference between the coupled and the uncoupled system. The electron density difference is obtained by the simple evaluation

$$\Delta n = n(\text{interacting system}) - \sum_i n(\text{non}-\text{interacting system } i). \tag{2.27}$$

For adsorbate systems the non-interacting systems are selected as the gas-phase molecule and the slab. Then the electron density difference by Eq. (2.27) will give the bonding and anti-bonding electron density induced by the molecule-slab interaction. The bonding character is recognized as an accumulation of electron density, the anti-bonding character as a depletion of the electron density. However, the charge density difference analysis does not include the orbital projection of molecular bonds, e.g. it does not distinguish between σ and π bonds. Such results are only obtained from electron localization function (ELF) calculations [63]. In spite of the nice features of the ELF, there is still a problem of determining the appropriate isosurfaces. In this thesis, keeping simplicity, only an electron density difference analysis will be applied.

2.3 Chemical reactions

The determination of surface reactions requires the calculation of the appropriate PES. A diatomic adsorbate system is fully described by a 6-dimensional PES, if the rearrangement of substrate degrees of freedom is not crucial, and 2-dimensional cuts are

often useful to analyze the system. However, considering the formation of clusters or reactions of large molecular systems such as ammonia (NH_4) and methanol (CH_3OH), the determination of high dimensional energy hyperplane requires an immense computational power. The artificial reduction of dimensions by freezing selective coordinates can lead to erroneous results by predicting wrong reaction configurations. Here transition state theory (TST) is introduced as a simple and effective method to ascertain reaction pathways with a comparably low cost.

2.3.1 Transition state theory

The construction of the quantum version of TST raises the following questions. First of all, how can physical observables be properly expressed in quantum language, in particular the partition function? A variety of quantum generalizations has been proposed as a model of QTST, but we focus on the method of replacing the classical statistical average by a quantum statistical average, especially on the method using the idea of a centroid density which are based on Gillan's rate theory [64, 65]. As a first application, Voth, Chandler and Miller (VCM) built a quantum version of the partition function [66, 67]. The next question is how the quantum statistical formulation satisfies the variational criterion to determine the rate limiting step. Messina, Schenter and Garrett (MSG) generalized VCM's idea by allowing a variational method in quantum Monte Carlo sampling [68, 69]. More recently, the reversible work transition state theory (RW-TST) has been developed by Mills, Jónsson and Schenter [70, 71]. The advantage of the reversible work method is a high applicability to multi-dimensional systems with satisfying the variational criterion.

We start from the classical version of TST for simplicity to assemble the QTST to DFT problems. When the reactant and product states are well divided by a hypersurface through the transition state $Z^\ddagger$ and the energy of the particles in the reactant state follows a Boltzmann distribution, classical transition rate is expressed as

$$k^{\mathrm{TST}} = \frac{1}{2}\langle|v_\perp|\rangle\frac{Q^\ddagger}{Q^{\mathrm{R}}} = \frac{k_{\mathrm{B}}T}{\sqrt{2\pi\mu k_{\mathrm{B}}T}}\frac{Q^\ddagger}{Q^{\mathrm{R}}}, \tag{2.28}$$

where k_{B} is Boltzmann's constant and μ is an effective mass for the reaction coordinate $\mathbf{\Gamma}_s$. The hyperplane confinement at the dividing surface is given by $Z = \mathbf{n}^\ddagger \cdot (\mathbf{r} - \mathbf{\Gamma}^\ddagger) = 0$. The dividing surface is determined by a variational method minimizing the rate constant [72], but for high-dimensional systems this is a non-trivial problem.

Expressing the quantum mechanical partition function is possible by adopting Feynman and Hibbs' formulations of quantum statistical mechanics [73]. The description in terms of Feynman path integrals (FPI) gives a general combination of quantum mechanics and quantum statistics in complex time τ. The quantum partition function is expressed in terms of FPIs where the effective potential is

$$V_{\mathrm{eff}}(x) = \sum_{i=1}^{P}\left[\frac{k(x_i - x_{i-1})^2}{2} + \frac{V(x_i)}{P}\right], \tag{2.29}$$

with the spring constant $k = mP/\hbar^2\beta^2$, the particle mass m and $\beta = 1/k_{\mathrm{B}}T$. The quantum partition function will be exact when $P \to \infty$. The quantum statistical

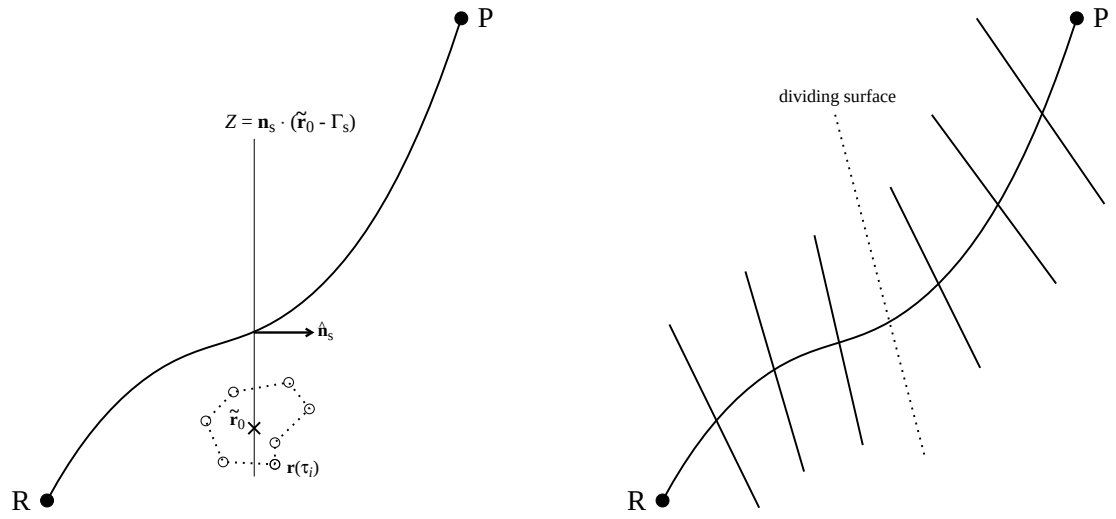

(a) Reaction path, Γ_s (b) Hyperplane Progress

Figure 2.3: The hyperplane intersecting the reaction path at the reaction coordinate s is defined as $Z = \mathbf{n}_s \cdot (\mathbf{r} - \mathbf{\Gamma}_s)$. The centroid density $\tilde{\mathbf{r}}_0$ is given by the FPI chain confined in the hyperplane (a). The hyperplane is gradually moved from the reactant region towards the products by varying the reaction coordinate (b). Reversible work allows moving and rotating the hyperplane to an intermediate region [71].

effects are taken into account by the delocalization of the FPI chain, for $P > 1$. The classical limit for the effective potential is given by $k \to \infty$. It corresponds to increasing the mass or temperature, and the system will be localized in the classical limit of hard springs.

The QTST was improved within the concept of rate theory in quantum systems by introducing the centroid coordinate $\tilde{x}_0$ by Gillan. It fixes the FPI chain at a given point and corresponds to the average over the remaining quantum degrees of freedom and classical bath degrees of freedom:

$$\tilde{x}_0 = \frac{1}{\hbar\beta} \int_0^{\hbar\beta} d\tau \, x(\tau) = \frac{1}{P} \sum_{i=1}^{P} x_i, \tag{2.30}$$

where i is running over all the FPI images of the particle. A gradual shift of the centroid from the reactant region to the saddle point yields the free energy difference and the rate constant at the transition state. The variational criterion was used for the dividing surface determination through minimizing the rate constant. However, in the approach of VCM and MSG the reaction coordinate was still one-dimensional. It can just be adopted to geometry restricted systems, e.g. $\mathrm{H} + \mathrm{H_2} \to \mathrm{H_2} + \mathrm{H}$. However, more realistic systems with high dimensional reaction coordinates were still hard to treat.

The concept of the RW-TST is based on the hyperplane confinement of the centroid integration, and moreover on the gradual and reversible shift of the hyperplane along the reaction coordinate. The progress of the reaction is written in terms of the FPI

centroids of the quantum mechanical atoms in the primary system. To buildup the reversible work, all particles in the reactant region are rearranged into the hypersurface Z^R as an intermediate state. Finally, the hypersurface Z^R is located in the reactant region. Then the rate constant is rewritten as

$$k^{\mathrm{TST}} = \frac{k_{\mathrm{B}}T}{\sqrt{2\pi\mu k_{\mathrm{B}}T}} \frac{Q^{\ddagger}}{Q^{Z^R}} \frac{Q^{Z^R}}{Q^{\mathrm{R}}} = \frac{k_{\mathrm{B}}T}{\sqrt{2\pi\mu k_{\mathrm{B}}T}} \frac{Q^{\ddagger}}{Q^{Z^R}} e^{-\beta\,\delta A(s)}, \tag{2.31}$$

with the free energy difference $\delta A(s)$. For reversible work, the hyperplane constraint becomes

$$Z = \mathbf{n}_s \cdot (\tilde{\mathbf{r}}_{\mathbf{0}} - \mathbf{\Gamma}_s) = 0. \tag{2.32}$$

The centroid integration at the reaction coordinate s is evaluated with the hypersurface confinement as illustrated in Fig. 2.3a. The hyperplanes progress from the reactant state to the product state along the reaction coordinate $\mathbf{\Gamma}_s$ is illustrated in Fig. 2.3b. If the hyperplanes are spaced closely enough to satisfy an adiabatic change of the free energy, then the free energy difference between the reference hyperplane Z^R and a hyperplane Z_s is given by

$$\delta A(s) = -\int_R^s dz s' \,\langle \frac{1}{P} \sum_{i=1}^{P} F_n(i)(1 - \kappa R_t(i))\rangle_{s'}, \tag{2.33}$$

where F_n represents the potential variance along the hyperplane normal, and R_t is the turning direction component of the distance from the reference point. The quantum mechanical partition function for a hyperplane at s is represented by

$$Q_s = \int D\mathbf{r}(\tau)\, e^{-\beta V_{\mathrm{eff}}} \delta[\mathbf{n}_s \cdot (\tilde{\mathbf{r}}_0 - \mathbf{\Gamma}_s)]. \tag{2.34}$$

However, for reversible work the free energy is evaluated by the free energy difference in Eq. (2.33) rather than directly evaluated by the partition function Eq. (2.34). Furthermore the statistical average of quantum observables in the hyperplane is

$$\langle X\rangle_s = \frac{\int D\mathbf{r}(\tau)\, e^{-\beta V_{\mathrm{eff}}}\, X\, \delta[\mathbf{n}_s \cdot (\tilde{\mathbf{r}}_0 - \mathbf{\Gamma}_s)]}{Q_s}. \tag{2.35}$$

When a reaction path from reactant to product region is defined, then the sequence of hyperplanes intersecting the path is also determined. The planes are selected close to each other enough to satisfy reversible work in Eq. (2.33). A convenient choice for the reaction path is the minimum energy path (MEP). The optimal dividing surface $Z^{\ddagger}$ is the hyperplane Z_s corresponding to the maximum free energy, where both the force $\langle F_n\rangle_s$ and the torque $\langle F_n R_t\rangle_s$ acting on the hyperplane vanish. An alternative choice of a zero-torque path (ZTP) leads to a pure translational supported free energy change. The MEP and ZTP have identical free energy barriers but ZTP yields a much smoother free energy curve [71]. The free energy barrier is determined independently from the selection of paths as long as the paths satisfy a variational criterion. The integration along the reaction path gives a free energy maximum at the free energy

barrier for the transition of the quantum system. Moreover it fulfills the variational criterion automatically.

As an example of the reversible work formulation to surface problems, hydrogen dissociative adsorption can be considered [70]. The reaction coordinate of the system is selected as the surface normal z for the approach to surface, and the hyperplane confinement of the MEP is expressed as $\tilde{z}_1 + \tilde{z}_2 =$ constant in the reactant region and $\tilde{x}_1 - \tilde{x}_2 =$ constant in the product region. In the intermediate region,

$$(\tilde{z}_1 + \tilde{z}_2) = c(\tilde{x}_1 - \tilde{x}_2), \tag{2.36}$$

where c is a constant. The quantum statistical sampling under the hyperplane confinement (each sampling is derived by the determination of corresponding FPI chain) leads to the evaluation of the average value of the free energy using Eq. (2.33), and the propagation along the reaction coordinate yields the potential energy curve. Thus the activation barrier of H_2 dissociation over Cu(110) surface was found to be 0.38 eV [70, 74]. It was slightly smaller than the experimental data 0.43 eV, but still in good agreement.

Finally, the implementation of the reversible work simplifies the QTST problem in the selection of the appropriate hyperplane confinement. The establishment of the corresponding reaction path is derived by connecting the minimum energy configurations of propagating hyperplanes. The MEP is defined by the boundary conditions that the MEP must start at the lowest-energy reactant state and finish in the lowest-energy product state. And it must satisfy the requirement that the force at any point be parallel to the MEP itself.

2.3.2 Nudged elastic band method

As an efficient way to find the MEP, the nudged elastic band (NEB) method was introduced by Jónsson *et al.* [70, 75]. This method finds the MEP in a variational fashion, but much faster than the original elastic band method. Consider an elastic band consisting of beads, connected by harmonic springs between reactant and product states. By using a set of images of the system the elastic band describes a discrete reaction pathway. Thus the problem to find the MEP is transformed to finding the minimum of a given function,

$$F(\mathbf{r}_1, \mathbf{r}_2, \cdots, \mathbf{r}_{P-1}) = \sum_{i=1}^{P-1} V(\mathbf{r}_i) + \sum_{i=1}^{P} \frac{kP}{2}(\mathbf{r}_i - \mathbf{r}_{i-1})^2, \tag{2.37}$$

where the sum is over the true potential energies of intermediate images $V(\mathbf{r}_i)$ and elastic spring energies which guarantees the continuity of the reaction path $\{\mathbf{r}\}$. The convergence of the images onto the MEP demands a rather high cost using all degree of freedoms. Here comes the concept of nudging, the coordinate decomposition. The force projection on the bead parallel and perpendicular to the local path accelerates the convergence under the following assumptions: (*i*) the perpendicular component of the force leads the bead onto the MEP and (*ii*) the parallel component pushes the band into the reactant or the product state with maintaining the space between the beads. The perpendicular force does not interfere with the convergence of the elastic band to

the MEP and the parallel force does not affect the distribution of images. In every iteration step, the tangent to the path must be re-estimated for force nudging. The iterations will be continued until all perpendicular component of the beads are zero, which means that the elastic band is located on the MEP.

The tangent definition with respect to the reaction path at each ionic step is significant for the convergence. The original NEB defines the tangent as a unit vector in the direction from the previous to the next bead. However, this definition leads to a convergence problem for a sudden change of the tangent. The revised tangent definition was introduced by Henkelman and Jónsson to avoid such a kink problem [75]. If the i-th image and its neighbors have a monotonic energy increase or decrease, the corresponding tangent is defined as

$$\tau_i = \begin{cases} \tau_i^+ & \text{if} \quad V_{i+1} > V_i > V_{i-1} \\ \tau_i^- & \text{if} \quad V_{i+1} < V_i < V_{i-1} \end{cases}, \tag{2.38}$$

where $\tau^+ = \mathbf{R}_{i+1} - \mathbf{R}_i$ and $\tau^- = \mathbf{R}_i - \mathbf{R}_{i-1}$. At a local minimum or local maximum, a mixed configuration is suggested as follows

$$\tau_i = \begin{cases} \tau_i^+ \Delta V_i^{\max} + \tau_i^- \Delta V_i^{\min} & \text{if} \quad V_{i+1} > V_{i-1} \\ \tau_i^+ \Delta V_i^{\min} + \tau_i^- \Delta V_i^{\max} & \text{if} \quad V_{i+1} < V_{i-1} \end{cases}, \tag{2.39}$$

with $\Delta V_i^{\max} = \max(|V_{i+1} - V_i|, |V_{i-1} - V_i|)$ and $\Delta V_i^{\min} = \min(|V_{i+1} - V_i|, |V_{i-1} - V_i|)$. There is further slight change in the definition of the force,

$$\mathbf{F}_i^s|_{\parallel} = k(|\mathbf{R}_{i+1} - \mathbf{R}_i| - |\mathbf{R}_i - \mathbf{R}_{i-1}|)\hat{\tau}_i, \tag{2.40}$$

which arranges the beads equally spaced in the band. The elastic band converges onto the MEP when the number of images is sufficiently large, but using an interpolation scheme the continuous MEP can be reproduced using only a few number of images. It allows the precise determination of the activation barrier and the local energy minimum from discrete image energies.

The implementation of the revised NEB into VASP followed the instruction of the Jónsson group. For the NEB calculations found in this thesis 4 images have been used. The energy curve was interpolated by cubic spline fitting in terms of the reaction coordinate using both the parallel and perpendicular forces. The reaction coordinate includes the sum of all ionic displacement.

The geometric configuration and energy barrier at the transition state is partly determined by the climbing image NEB [76] or the dimer method [77]. If the NEB images are already close to the true reaction path after several tens of NEB steps, the dimer method will accelerate the final convergence to the transition state.

Chapter 3

Surface adsorbates

Properties of various adsorbed molecules, corresponding to the intermediate states of methanol decomposition, have been calculated over Cu(100) and Cu(110). Each substrate was prepared as a 5 layer slab with the two upper most Cu layers fully relaxed. Substrates were separated by 12 Å of vacuum layer. For single molecular and atomic adsorption a (2×2) supercell with a coverage of $\theta_{\mathrm{mol}} = 0.25$ was used. Adsorbate induced surface re-relaxations are taken into account, but any adsorbate induced surface reconstruction was not included, e.g. the missing row reconstruction of (2×1)O/Cu(110). Adsorbate and co-adsorbate phases have been evaluated based on data from STM experiments.

3.1 Molecular properties of gas phase species

The assignment of molecular orbitals and the projected local density of states (LDOS) makes an intuitive interpretation of chemical bonding of molecules possible. The assignment of the molecular orbitals was done according to general quantum chemistry naming rule [78]. In the gas phase, atomic and molecular orbitals are defined by well-localized Kohn-Sham eigenstates. The characteristics of each LDOS peak can be associated with a particular molecular bond by an orbital projected LDOS analysis. In Fig. 3.1, the molecular orbitals of formaldehyde (CH_2O), methoxy radical (CH_3O) and methanol (CH_3OH) are plotted with respect to the vacuum energy. Formaldehyde and methanol are close-shell species, all shown orbitals are fully occupied. Close-shell species are stable in the gas-phase, but methanol forms a polycrystalline state through weakly polarized hydroxyl bonds (OH) like other alcohols. In contrast, methoxy is an open-shell species. The Fermi level of methoxy crosses the $2e$ orbital. The partially filled $2e$ radical induces the strong reactivity of the methoxy radical.

The symmetry of the gaseous species is reflected in the hybrid orbitals of the ethyl group ($:CH_2$) and methyl group ($\cdot CH_3$). The flat ethyl group forms σ_{CH_2} and π_{CH_2} hybrids with C_{2v} symmetry. On the other hand, the methyl group forms σ_{CH_3} and

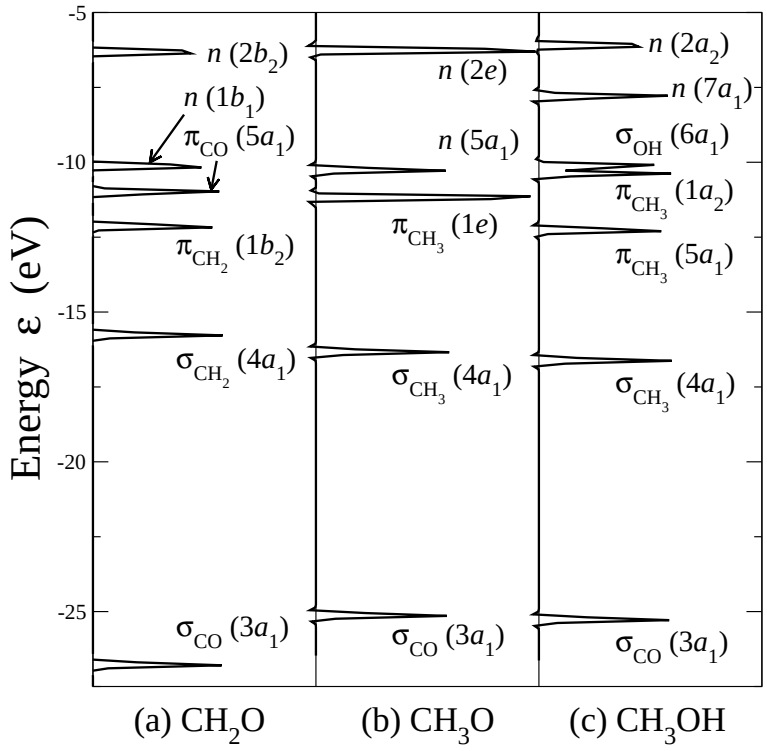

Figure 3.1: Occupied DOS peaks of gaseous molecules: (a) formaldehyde, (b) methoxy and (c) methanol. Chemical bonds are assigned in σ and π. n represents non-bonding electrons. The Fermi level of methoxy radical crosses the $2e$ orbital, corresponding to a filling factor of 3/4.

degenerate π_{CH_3} hybrids with C_{3v} symmetry. Formaldehyde forms an ethyl hybrid and oxygen sp^3 hybrids. The molecular orbitals of formaldehyde are assigned to the DOS peaks in Fig. 3.1a. The lowest orbital is the CO sigma-bond ($3a_1$), the CH_2 σ and π bonds ($4a_1$, $1b_2$) are located above it. The π-type bond of CO ($5a_1$) is the highest occupied bonding orbital. Non-bonding orbitals ($1b_1$-$2b_2$) are located just below the Fermi energy ε_F. In the methoxy radical (Fig. 3.1b), a degenerate CH_3 π-bonding orbital ($1e$) is found which comes from the hybridization of hydrogen s and formaldehyde $5a_1$ orbitals. The anti-bonding character of the $2e$ orbital leads to a CO bond stretching. Furthermore, the π_{CO} bond breaking and forming of the CH_3 group induces a σ_{CO} bond upshift. The non-bonding orbitals $1b_1$ and $2b_2$ are degenerate with $2e$ by symmetry and partially occupied from the $5a_1$ orbital.

In the gas-phase, upon the methoxy excitation of ${}^2E \rightarrow {}^2A_1$, a $5a_1$ electron transits into the $2e$ orbital:

$$\begin{array}{ll} (3a_1)^2(4a_1)^2(5a_1)^2(1e)^4(2e)^3 & {}^2E \\ (3a_1)^2(4a_1)^2(5a_1)^1(1e)^4(2e)^4 & {}^2A_1 \end{array} \tag{3.1}$$

This Rydberg state represents an excited state of the methoxy radical [79]. The $2e$ orbital filling induces a CO bond enlargement, because the $2e$ orbital has CO anti-bonding and CH_3 bonding characters [80]. As a reference, ${}^2A_1$ state can be compared with an active transition state of the photocatalytic hydrogenation and with a surface

adsorbate with a reactive $5b_1$ orbital.

As for methanol, the hydroxyl bond ($6a_1$) is formed from the bonding of the half-filled methoxy $5b_1$ and the hydrogen s-electron. Since the hydroxyl bond topologically breaks the C_{3v} symmetry of the CH_3 group, the π_{CH_3} states contributing to the $1e$ and $2e$ orbitals of methoxy are split into $5a_1/1a_2$ and $7a_1/2a_2$ states, respectively. It implies that over the high symmetry sites of a metal surface methoxy adsorbate binds without C_{3v} symmetry breaking. As a result, the methoxy adsorbate will maintain its $1e$ and $2e$ degeneracy at the high symmetry sites with an elongated CO bond along the surface normal.

The molecular properties of various gaseous organic molecules calculated using DFT are listed in Table 3.1. The bond geometry of each molecule is in good agreement with available experimental data within an 1 % error. According to the DFT calculations, there are two different angles $\angle_{HCO}$ of methanol whereas the angles $\angle_{HCH}$ are almost identical. Due to the presence of the OH bond, the C_{3v} symmetry of the CH_3 group is broken. Therefore there are two different values for $\angle_{HCO}$ and $\angle_{HCH}$. The $\angle_{HCH}$ values reflect the anisotropy of the CH_3 group induced by OH bond. The molecular geometry of the HCO radical is in good agreement with experiments; it shows that radicals can be also successfully reproduced by DFT calculations. Even though experimental information for the methoxy and the formate radical are missing, the DFT estimated molecular properties are expected to be reliable and accurate.

The energy convergence of the methanol molecule requires a high cutoff energy of the plane wave basis. The molecular energy is converged within 1 meV at 600 eV. However, already at 320 eV the error for the free methanol molecule is below 10 meV.

		CH_3OH	CH_3O	CH_2O	HCOO	HCO
$E_{mol}^{(g)}$	GGA	−30.22	−24.03	−22.15	−23.98	−16.72
d_{CO}	GGA	1.43	1.35	1.22	1.24	1.19
	Exp.	1.4246	-	1.2080	-	1.1712
d_{CH}	GGA	1.10	1.13	1.12	1.17	1.15
	Exp.	1.0936	-	1.116	-	1.110
$\angle_{HCO}$	GGA	112.3/106.5	112.0	122.0	108.2	123.1
	Exp.	-	-	121.75	-	127.43
$\angle_{HCH}$	GGA	108.4/108.9	106.7	116.0		
	Exp.	108.63	-	116.5		
d_{OH}	GGA	0.97				
	Exp.	0.9451				
$\angle_{COH}$	GGA	108.2				
	Exp.	108.5				

Table 3.1: Molecular properties of gas phase species evaluated by DFT. Molecular energy $E_{mol}^{(g)}$ is expressed in eV, chemical bond lengths d in Å and bond angle $\angle$ in degree. Experiment data of molecular geometry in gas-phase were found in *CRC Handbook of Chemistry and Physics, 75th ed., CRC Press (1995)*. Methoxy and formate radical data are not available.

Hence we have chosen a cutoff energy of 350 eV for all results reported in this thesis which yields sufficient accuracy.

3.2 Electronic structures of surface adsorbates

Detailed DFT calculations have been executed for various adsorbate configurations. The results show that the surface species can be mainly categorized as physisorbed or chemisorbed adsorbates by the strength of the surface-adsorbate interactions. On clean copper surfaces, the closed-shell species methanol and formaldehyde are weakly physisorbed. In Fig. 3.2, the LDOS of physisorbed methanol over Cu(100) and Cu(110) is plotted. The gas-phase LDOS can be compared to the adsorbate state by aligning the vacuum energies. The lower adsorbate orbitals $3a_1$-$5a_1$ are identical to the gas-phase orbitals. The gas-phase methanol molecular orbitals keep their identity on the metal surface which means that they are narrow and well-identified without any splitting or broadening by the interaction with the surface. The non-bonding electron peaks ($7a_1$-$2a_2$) are slightly shifted down, and the σ_{OH} orbital ($6a_1$) is at the same position as the $\pi_{\mathrm{CH_3}}$ ($1a_2$) orbital. However, still the peaks are well defined. Hence the change of the molecular bonds can be considered to be negligible. Experimentally, the peaks have been measured in UPS experiments by Bowker *et al.* on Cu(110) [81]. They show that physisorbed methanol orbitals are not affected strongly by the adsorbate-surface interaction. All peaks are located close to their gas-phase positions. The down-shift of the non-bonding electron orbital is also very small for the orbitals of physisorbed formaldehyde, as shown in Fig. 3.3. Such a small amount of orbital lowering of adsorbed

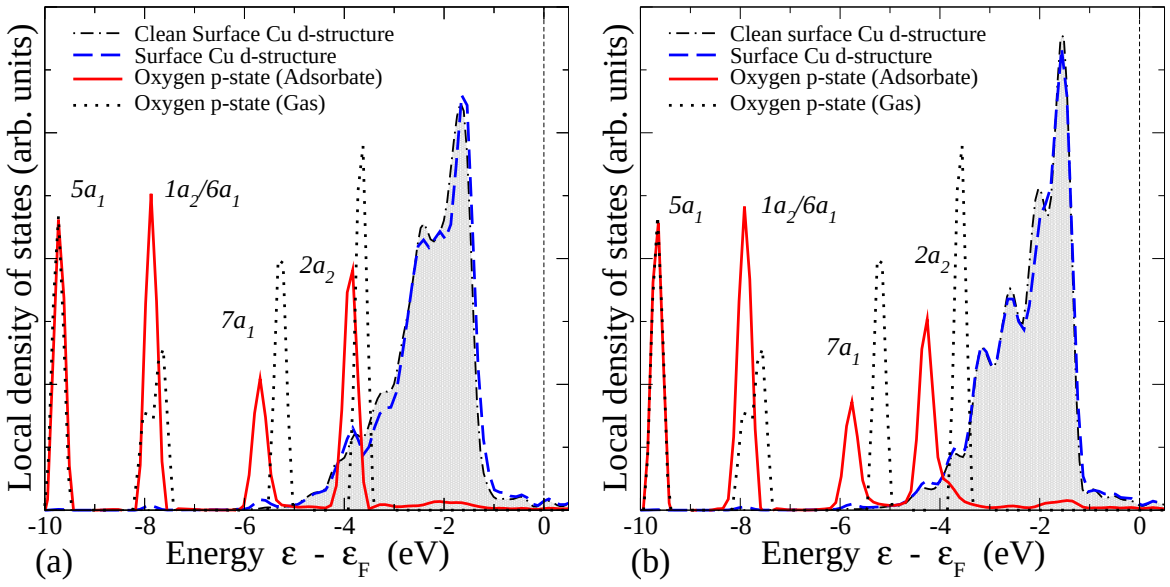

Figure 3.2: Local density of states of physisorbed methanol within the adsorption configuration (a) O_{top}-H_{hl}/Cu(100) and (b) O_{sb}-H_{hl}/Cu(110). The non-bonding electron orbitals ($7a_1$-$2a_2$) of the physisorbed adsorbates are shifted down still maintaining their gas-phase characters. The σ_{OH} orbital $6a_1$ is lowered by an anti-bonding contribution.

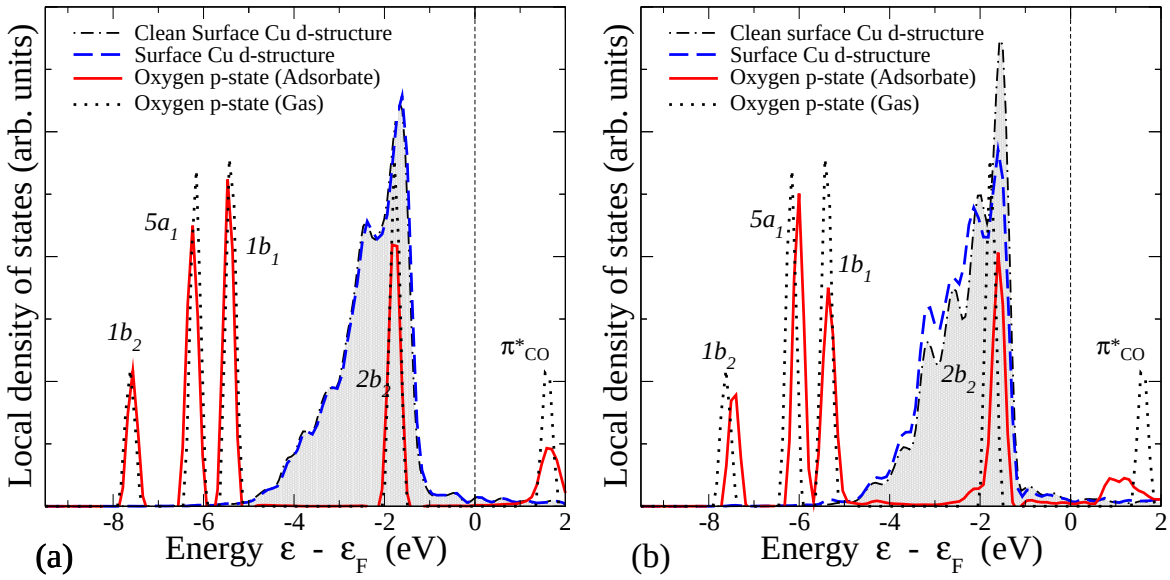

Figure 3.3: Local density of states of physisorbed formaldehyde at a large adsorption height on (a) Cu(100) and (b) Cu(110). The adsorption configuration for physisorbed formaldehyde is selected with the CO bond parallel to the surface at a large adsorption height, over 2.7 Å. The anti-bonding orbital π^*_{CO} is well localized over Fermi level.

molecules corresponds to a weak interaction between the adsorbate and the surface and to a small physisorption energy.

The molecular properties of adsorbed methanol are listed in Table 3.2 and of adsorbed formaldehyde in Table 3.4. The molecular geometries of physisorbed methanol and formaldehyde are not changed from the gas-phase structures at the various adsorption configurations. For both physisorbed molecules, the binding energies are estimated to be of the order of 0.1 eV. Experimentally, methanol and formaldehyde adsorption energies have been measured by different groups. A redhead analysis of SKS data gives a methanol adsorption energy of −0.56 eV on Cu(111) [82] and −0.43 eV on Cu(100) [83]. Formaldehyde on Cu(111) clusters which are supported by SiO_2 has an adsorption energy of −0.33 eV [84]. A TPD experiment on Cu(110) gives an adsorption energy of −0.70 eV for methanol and −0.56 eV for formaldehyde [12]. In previous theoretical studies, the determined physisorption energies were smaller than the experimental data [85–87]. The same trend is found in this work. The binding energies listed in Table 3.2 and Table 3.4 correspond to roughly half the experimental value. It can be explained by the fact that, in general, DFT-GGA underestimates physisorption energies and van der Waals forces.

The binding energy of physisorbed methanol has a weak dependence on the adsorption site. The hydroxyl group is close to the surface, and its bond is parallel to the surface. The oxygen prefers to be close to the top site and the OH bond is oriented towards a high symmetry site with the CO bond almost upright. The methanol adsorption configurations will be assigned as O_{site1}-H_{site2}, where "$site1$" represents the nearest high symmetry site for oxygen and "$site2$" for hydrogen. On Cu(100), the most

Lattice	Config	E_{ads}	$h_{\text{Cu-O}}$	$d_{\text{Cu-O}}$	d_{CO}	d_{OH}	$\angle_{\text{COH}}$	d_{CH}	$\angle_{\text{HCO}}$	$\angle n_{\text{CO}}$	$\angle n_{\text{OH}}$
Cu(100)	O_{top}-H_{br}	−0.18	2.24	2.27	1.44	1.00	112.8	1.10/1.09	111.1/105.8	27.0	85.7
	O_{top}-H_{hl}	−0.21	2.20	2.23	1.45	1.00	113.4	1.10/1.09	111.1/105.9	32.0	81.6
	O_{br}-H_{hl}	−0.19	2.46	2.84	1.45	1.00	111.8	1.10/1.09	111.3/106.5	8.9	103.1
Cu(110)	O_{sb}-H_{hl}	−0.35	1.84	2.34	1.46	1.01	114.0	1.10/1.09	110.6/105.5	17.6	96.3
	O_{top}-H_{lb}	−0.41	2.02	2.18	1.46	1.00	111.5	1.10/1.09	110.0/105.7	75.6	103.3
	O_{lb}-H_{hl}	−0.20	1.94	2.65	1.45	1.00	112.2	1.10	111.3/105.9	11.5	100.7

Table 3.2: Molecular properties of physisorbed methanol. The methanol adsorption energies E_{ads} are expressed in eV. The adsorption geometry is described by the adsorption height $h_{\text{Cu-O}}$ and the distance from the nearest Cu atoms $d_{\text{Cu-O}}$. The orientation of methanol is specified by the CO bond angle to the surface normal $\angle n_{\text{CO}}$ and to the OH bond $\angle n_{\text{OH}}$. The bond lengths are not very different from their gas-phase values. In all adsorbate configurations, the hydroxyl bond is parallel to surface.

favorable adsorption configuration corresponds to O_{top}-H_{hl} and on Cu(110) to O_{top}-H_{lb}. The adsorption energies differ within 30 meV between different adsorption sites on Cu(100). This means that methanol molecules which are located 2.2 Å above the surface are very mobile. On Cu(110), methanol is attracted closer to the surface caused by a stronger interaction between the methanol non-bonding electrons and the surface which is reflected by the larger interaction induced down-shift of the non-bonding orbital down-shift on Cu(110). As a consequence, the binding energy is larger by 0.2 eV compared to Cu(100). The adsorption position with the smallest distance to the nearest surface Cu atom, O_{top}-H_{lb}/Cu(110), has the largest adsorption energy. However, this configuration corresponds to a low-symmetry situation with the COH bond in a plane that does not contain the surface normal. A similar adsorption configuration was found on the top site of Pt(111) by Greeley and Mavrikakis [88], where the active site for oxygen is the top site.

For physisorbed formaldehyde, the CO bond is parallel to the surface. The adsorption height is larger than 2.7 Å, which is higher than for methanol physisorption. A parallel displacement, however, does not alter the adsorption energy at this adsorption height. Compared to the methanol physisorption, the smaller adsorption energy and the lesser variance of the LDOS reflect the weaker interaction between formaldehyde and surface. The anti-bonding orbital π^*_{CO} is well localized above the Fermi level ε_F, so that the back-donation from the metal surface is negligible.

The open-shell methoxy radical (CH_3O) chemisorbs directly via the oxygen atom. The CH_3-group orbitals ($4a_1$, $1e$) remain discrete at the surface as predicted by experiments [89, 90], since they are not disturbed by the surface-adsorbate interaction. In the gas-phase, the methoxy radical $2e$ orbital is partially filled. Electron transfer from the surface into the $2e$ orbital upon adsorption leads to CO bond stretching, since the

Lattice	Config	E_{ads}	h_{Cu-O}	d_{Cu-O}	d_{CO}	d_{CH}	$\angle_{HCO}$	$\angle n_{CO}$
Cu(100)	hollow	−2.96	1.21	2.18	1.46	1.10	109.8	0.0
	bridge*	−2.85	1.42	1.96	1.43	1.10	110.9/110.2	3.7
	top*	−2.22	1.83	1.83	1.41	1.10	110.8/111.0	2.8
Cu(110)	(111) step	−2.98	1.44	1.95	1.44	1.10	109.4/111.6	33.0
	long bridge	−2.63	1.17	2.03	1.45	1.10	109.8/111.5	16.3
	long bridge	−2.61	1.14	2.04	1.45	1.10	110.0/110.3	0.0
	hollow*	−2.33	1.09	2.41	1.46	1.10	110.4/109.9	0.1
	short bridge*	−2.98	1.44	1.95	1.44	1.10	109.3/111.8	34.0
	top*	−2.22	1.81	1.81	1.41	1.10	110.8/111.0	0.8
Cu(111)	fcc hollow	−2.68	1.45	2.08	1.44	1.10	110.1	0.0

Table 3.3: Molecular properties of adsorbed methoxy over various Cu surfaces. The binding energies E_{ads} are expressed in eV. The adsorbate geometry is described by the adsorption height h_{Cu-O}, the distance d_{Cu-O} and the CO bond tilt angle to the surface normal $\angle n_{CO}$. The symbol * denotes non-stable adsorption geometries with the oxygen atom located above a given high symmetries site, even if there are remaining forces at this oxygen site in the x-y plane.

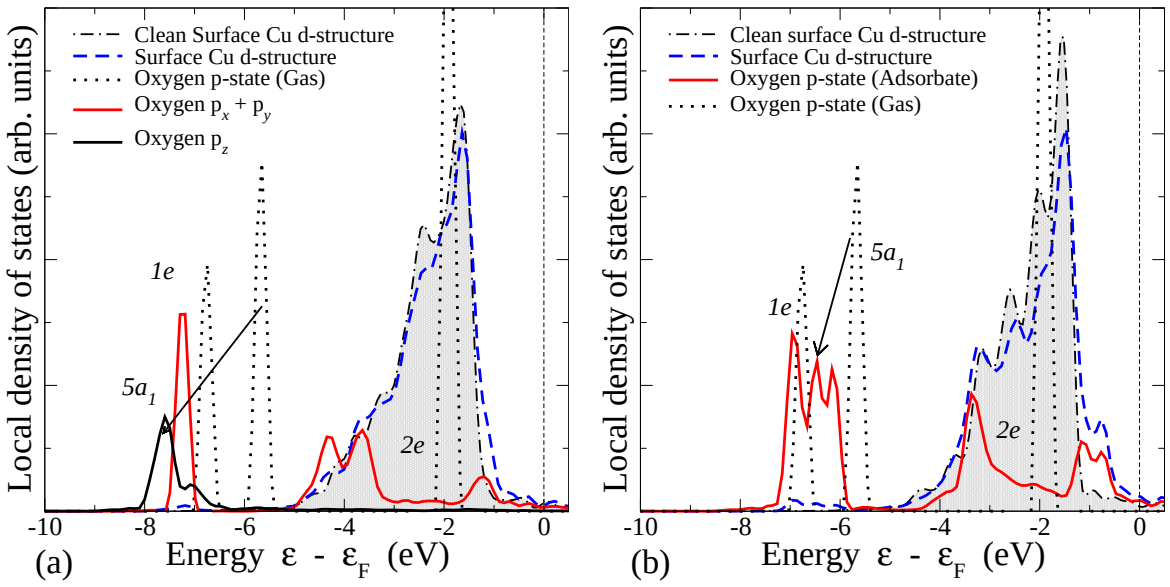

Figure 3.4: Local density of states of chemisorbed methoxy within the adsorption configuration of (a) O_{hl}/Cu(100) and (b) O_{ph}/Cu(110). On Cu(100), a $5a_1/1e$ orbital inversion is visible in terms of orbital projected DOS. The strong interaction between O and Cu leads to a split $2e$ orbital. On Cu(110), adsorption on the pseudo (111) edge leads to a breaking of the C_{3v} symmetry for the $1e$ orbital. As a result, the $1e$ orbitals are split and located around the $5a_1$ orbital.

$2e$ orbital has partially an anti-bonding CO character [80]. In Fig. 3.4, the LDOS peak of the $2e$ orbital is significantly broadened and split by the interaction with the surface d-band on both Cu(100) and Cu(110). This hybridization causes the direct chemical bonding of the methoxy-metal system. As a result, methoxy chemisorption involves a large adsorption energy. The relaxed methoxy adsorbate gains around 2.9 eV adsorption energy at the high symmetry sites. Figure 3.5 shows charge density difference plots for methoxy over the four-fold hollow site of Cu(100). Charge accumulation on the oxygen site and overall depletion on the nearest Cu sites are visible. Moreover, the strong charge depletion on CH_3 reflects the changes of the $\pi^*_{CH_3}$ orbital ($3e$) which contributes to the anti-bonding CO orbital and induces a stretching of the CO bond. The methoxy non-bonding electron pair $5a_1$ is also shifted down on the Cu surface leading to an $1e/5a_1$ orbital inversion, which has also been found in ARUPS experiment [91] and cluster calculation by Rodriguez (INDO/S) [92] for Cu(111). Figure 3.4a shows that the p_z ($5a_1$) orbital projected DOS is lower than the one of the $p_x + p_y$ ($1e$) orbitals.

An alternative description of the methoxy adsorption can be given by considering the gas-phase excitation of Eq. (3.1). In the presence of the substrate, the methoxy radical is activated to the $^2A_1$ state. This leads to a weakened CO bond and a $3a_1$ orbital up-shift which indicates a high reactivity. The electron donation into the $5a_1$ orbital is assumed to be the most probable process, it stabilizes the CO bond again. The $3a_1$ orbital recovers its position and the $5a_1$ orbital is lowered. The depletion

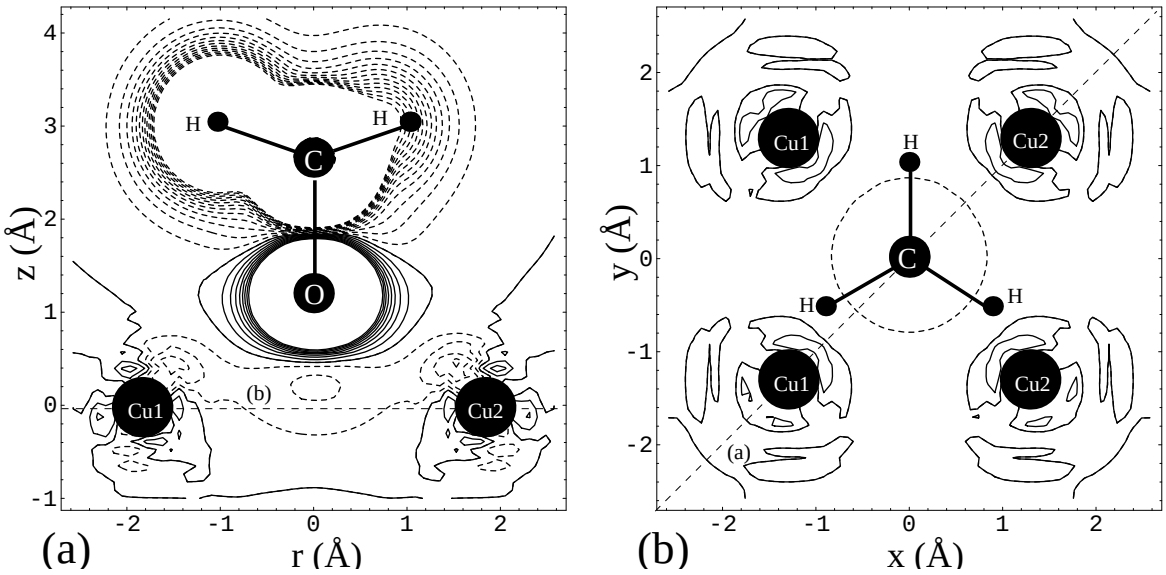

Figure 3.5: Charge density difference plot of adsorbed methoxy over the four-fold hollow site of Cu(100). (a) Side view along the [100] direction and (b) top view. The charge accumulation on the oxygen site is illustrated by solid lines, and the overall charge depletion on the nearest Cu atoms is denoted by dashed lines. The charge depletion on the CH_3 group (dashed lines) reflects the changes of the anti-bonding $3e$ orbital which leads to CO bond stretching. The parameter r in (a) corresponds to $\sqrt{x^2 + y^2}$.

of surface electrons will be compensated by the hybridization of the $2e$-d band. The adsorbate geometry partly reflects the $^2A_1$ state features described by Jackels [79]. The CO bond is stretched by 0.09 Å and the angle $\angle_{\mathrm{HCO}}$ is reduced by 2°, but the amount of the change is smaller than estimated by Jackels.

In Table 3.3, the molecular properties of chemisorbed methoxy are listed. The DFT calculations show that methoxy prefers high symmetry adsorption sites. On Cu(100), it is located at the four-fold hollow site in a configuration perpendicular to the surface as found in IR experiments by Ryberg [93]. Bridge and top site adsorption is only meta-stable under high hydrogen concentration. In the calculations, no fully relaxed adsorption geometry for methoxy adsorption at the bridge and top sites was found. The remaining force indicates that methoxy will slip down from the low coordination sites to the hollow site. However, under high atomic hydrogen coverage $\theta_{\mathrm{H}} = 0.25$, methoxy forms a fully relaxed meta-stable state at the bridge site with a 24.7° CO tilt angle. Several NEXSAFS and IRS studies have reported a $28 \pm 10°$ tilt of he CO bond on Cu(111) [91] and 30° tilt on Cu(100) [89]. These experiments apparently describe the meta-stable methoxy configuration under hydrogen co-adsorption. The DFT-GGA study by Greeley and Mavrikakis [85] also found a methoxy adsorption configuration at the high symmetry, three-fold hollow site of Cu(111). Our calculations for Cu(111) confirm the results of Greeley and Mavrikakis. On Cu(111), methoxy is by 0.3 eV more weakly bounded than on Cu(100) with a 0.25 Å higher adsorption site. SEXAFS experiments determined the methoxy adsorption configuration on Cu(111) yielding a

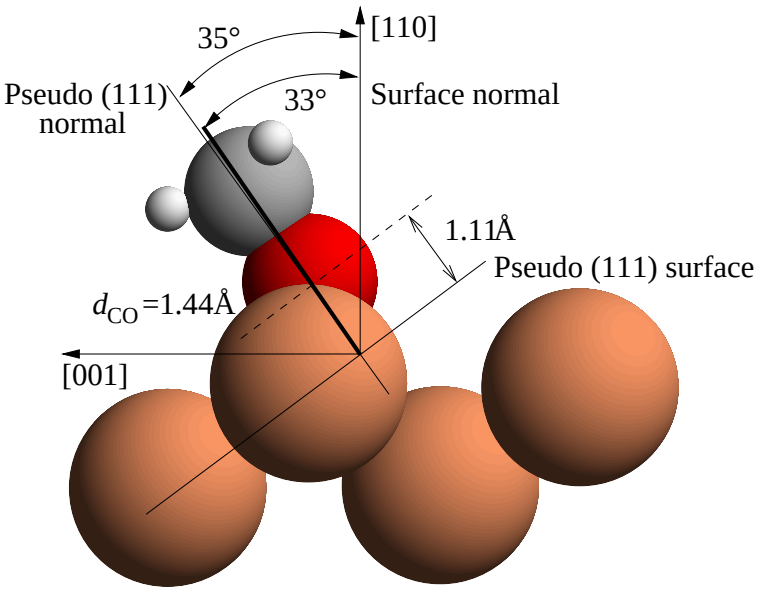

Figure 3.6: Adsorption geometry of methoxy on pseudo (111) edge site of Cu(110) in side view of direction [1$\bar{1}$0]. CO bond is oriented close to pseudo (111) surface normal.

CO bond length of 1.44 Å and a Cu-O distance of 2.00 Å [94], in good agreement with DFT calculations. Obviously, the close packed Cu(111) surface interacts less strongly with methoxy.

On Cu(110), surface methoxy is located at the pseudo (111) step edge site. The adsorption geometry is illustrated in Fig. 3.6 in a side view along the [1$\bar{1}$0] direction. The CO bond is tilted in [001] direction by 2° with respect to the pseudo Cu(111) surface normal. Interestingly enough, the adsorption height on the pseudo (111) surface of 1.11 Å is smaller than the pure Cu(111) surface result of 1.45 Å, and the distance to the nearest Cu atoms is also shorter by 0.1 Å. The adsorption on the step site enhances the methoxy-Cu substrate binding energy. This means that the methoxy adsorption depends not only strongly on the electronic structures, but also on geometric structural factors.

This adsorption configuration has also been found in NEXAFS experiments by Bader *et al.* [95] and XPD experiments by Holub-Krappe *et al.* [96] on Cu(110). These experiments find methoxy adsorbed on the short bridge site tilted by 30-40° along the [001] direction. It can be successfully interpreted as a pseudo (111) surface normal adsorption. The same adsorption configuration has been repeatedly found on various other systems, e.g. CH_3O/Ni(110) by Dastoor *et al.* [97] and NO/Pd(110) by Singh *et al.* [98]. Independent of the kind of substrate metal and adsorbate, the step edge configuration is often the most favorite adsorption site.

At an alternative adsorption site on Cu(110), the long bridge site, methoxy has two different adsorption geometries. In both configurations, the adsorption energy is smaller than on the pseudo (111) step edge by ca. 0.4 eV. At this configuration, the methoxy CO bond is either perpendicular or 16.3° tilted to the surface normal. The

tilt angle along the $[1\bar{1}0]$ direction was measured by Holub-Krappe *et al.* [96]. The experimental XPS value is about 18°, which is reproduced by our DFT calculations. As mentioned above, the CO bond orientation is influenced by the surface geometry. This configuration can be interpreted as a pseudo (100) step edge adsorption. However the terrace area of the pseudo (100) surface is not large enough, so that methoxy is hindered to be oriented along the pseudo (100) normal direction. Hence, the CO bond is not elongated along the pseudo (100) normal, and the adsorption energy is smaller than for the hollow site adsorption on Cu(100) by 0.33 eV.

A CO orientation perpendicular to the surface is repeatedly found on unstable top and four-fold hollow (second layer top) sites. The adsorption energies and the configurations of these unstable state are very close to the case of the Cu(100) top site adsorption. Apparently, the low symmetry adsorption is less sensitive to the direction of the surface orientation.

The LDOS peaks of methoxy on Cu(110) reflect the symmetry breaking at the pseudo (111) edge. In Fig. 3.4b, the π_{CH_3} ($1e$) orbital is split in two, and the $5a_1$ orbital is located between the $1e$ peaks.

3.3 Chemisorption of formaldehyde

Formaldehyde has been believed to be physisorbed on Cu metal surfaces. However, our DFT calculations predict a chemisorption configuration on both Cu(100) and Cu(110). The LDOS of the carbon and oxygen p-states of chemisorbed formaldehyde on Cu(100) is illustrated in Fig. 3.7. It shows a dramatic LDOS change compared to the physisorption state in Fig. 3.3a. The lower orbitals $3a_1$ and $4a_1$ are no more located at its gas-phase positions (see the inset in Fig. 3.7a), and the higher orbitals $1b_2$-$2b_2$ can not be clearly identified. Interestingly, the $3a_1$ and $4a_1$ orbitals are placed at the methoxy σ_{CO} and σ_{CH_3} positions in Fig 3.1. Furthermore, the Cu d-band structure close to the carbon site is also modified very strongly. The most impressive change is that the anti-bonding π^*_{CO} orbital is no more localized above the Fermi level, but shifted down significantly.

The LDOS of adsorbed formaldehyde on Cu(110) is illustrated for various adsorption in Fig. 3.8. The physisorbed formaldehyde peaks in Fig. 3.8a are hardly changed from their gas-phase positions. For the η^1-phase chemisorption, the oxygen binds to Cu atoms with a low coordination. The whole LDOS is shifted down by 1.2 eV. In particular, the position of the π_{CO} ($5a_1$) orbital becomes identical to the π_{CH_2} ($1b_2$) one as illustrated in Fig. 3.8b. The symmetry break caused by the presence of the surface leads to the reordering. The molecular geometry is not changed from the gas phase in the η^1-phase, but the adsorption energy is increased to -0.21 eV (listed in Table 3.4). As a result of the overall LDOS lowering, the anti-bonding π^*_{CO} orbital is just above of Fermi level. The peak is slightly broadened, but still well localized and unoccupied. The η^1-phase can still be interpreted as physisorption, since the adsorption energy is rather small and the LDOS peaks keep their shape. It is not clear, whether this configuration can be regarded as an intermediate for chemisorption.

The most dramatic LDOS changes are found for the η^2-phase formaldehyde chemisorp-

tion. The adsorption geometry has been determined to be with the CO bond parallel to the surface, and the carbon and oxygen atoms bind directly to the Cu atoms. Figures 3.8c and 3.8d describe the LDOS of the oxygen and carbon p-state of chemisorbed formaldehyde, respectively. The LDOS peaks are very similar to the ones on Cu(100) illustrated in Fig. 3.7. The adsorption geometry H_2C_{sb}-O_{sb}/Cu(110) is rather close to the H_2C_{br}-O_{br}/Cu(100) geometry. Thus we can conclude that the η^2-phase exists on various Cu faces. It corresponds to an universal adsorption scheme with a strong attraction to the surface. Both the carbon and oxygen atoms interact directly with the surface Cu structure. This leads to a σ_{CO} ($3a_1$) orbital up-shift of 1.55 eV and a σ_{CH_2} ($4a_1$) orbital down-shift of 0.93 eV as illustrated in the insets of Figs. 3.7a and 3.8c. This causes a methoxy-like CO and CH_2 orbital rearrangement, while higher orbitals ($1b_2$-$2b_2$) keep their formaldehyde characters. However, we found that the $1b_2$-$2b_2$ orbitals are extremely modified. The most important change is associated with the π^*_{CO} orbital filling. On both surfaces, the π^*_{CO} state is no more located above the Fermi level. The orbital is shifted down under the Fermi level as the arrows indicate in Figs. 3.7a and 3.8c and becomes occupied through electron transfer from the surface.

The theoretical background of the η^1- and η^2-phase chemisorption can be derived from the so-called Blyholder mechanism [99, 100]. It was introduced in order to explain the chemisorption of carbon-monoxide (CO) on metal surfaces. The Blyholder mechanism involves the σ donation of an electron from CO into unoccupied metal orbitals and π back-donation of electrons from metal orbitals into the $2\pi^*$ orbital of the CO molecule. This mechanism increases the CO-metal binding energy but decreases the CO bond strength [99–102]. On various metal surfaces the Blyholder mechanism has been intensively studied by theoretical [103, 104] and experimental investigations [105]. It has turned out that the Blyholder mechanism is very successful for alkali and transition

Lattice	Bond	Config	E_{ads}	h_{Cu-O}	d_{Cu-O}	d_{CO}	d_{CH}	$\angle_{HCO}$	$\angle_{HCH}$
Cu(100)	Phys.	-	−0.15	2.75	-	1.24	1.11	122.0	116.0
	Phys.	-	−0.14	3.00	-	1.24	1.11	121.6	117.0
	η^2	C_{br}-O_{br}	−0.70	1.42	2.13	1.41	1.11	112.5	106.7
Cu(110)	Phys.	-	−0.10	2.75	-	1.25	1.11	122.0	115.6
	η^1	O_{sb}	−0.21	1.72	2.16	1.27	1.10	120.1	119.7
	η^2	C_{sb}-O_{sb}	−0.63	1.17	2.02	1.41	1.11	110.7	107.3
O/Cu(110)	η^1	O_{sb}	−0.62	1.63	2.16	1.27	1.10	119.5	120.9
	η^2	C_{sb}-O_{sb}	−0.40	1.38	2.03	1.36	1.11	113.0	112.3

Table 3.4: Molecular properties of formaldehyde adsorbates. The binding energy E_{ads} is expressed in eV. The adsorption configuration is parallel to the surface for the physisorption and η^2-phase chemisorption states. For η^1-phase chemisorption, oxygen binds to the surface Cu atoms. The adsorption geometry is described by their adsorption height h_{Cu-O}, distance d_{Cu-O}. The molecular bonds are specified by the chemical bond lengths and their angles. For physisorption, the adsorption height is larger than 2.7 Å, and the surface geometry is not significant. The oxygen covered surface was evaluated within a (2×1)O structure in [001] direction, and formaldehyde was located between the oxygen rows.

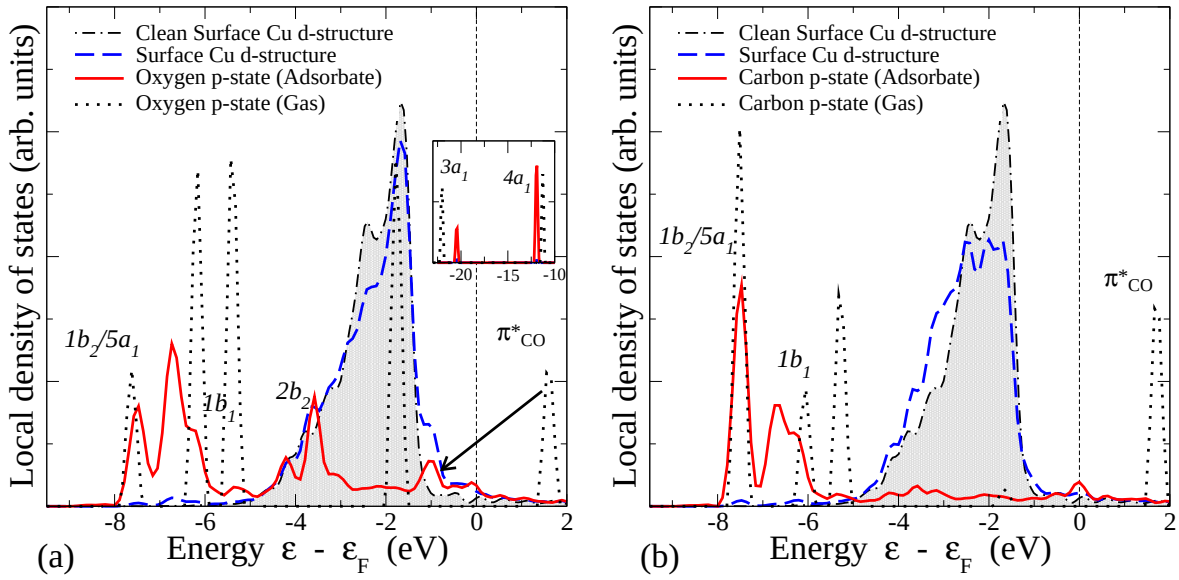

Figure 3.7: Local density of states of (a) the oxygen p-state of chemisorbed formaldehyde in the η^2-phase and of (b) the carbon p-state over Cu(100). The back-donation of metal electrons into the antibonding π^*_{CO} orbital leads to a dramatic change of the formaldehyde LDOS. A strong deformation of the surface Cu d-band beneath the carbon site in (b) indicates the direct chemical bond between Cu and C.

metals. On Cu surfaces, the π back-donation plays an energetically more important role in determining the character of the bond than the σ donation [106, 107]. CO is rather weakly bound to Cu with a heat of adsorption of about 0.8 eV [108]. Still it is believed that when the molecule has a partially filled π orbital, the back-donation mechanism is operative.

The formaldehyde adsorption had been studied by thermal desorption mass spectroscopy (TDMS) over clean and sulfided Pt(111) [109] and oxygen covered Ag(110) [110]. Furthermore, an EEL spectra study by Sexton *et al.* addressed polymeric paraformaldehyde adsorption over oxygen precovered Cu(110) surface [111]. A detailed identification of chemisorbed formaldehyde was first done by an EELS study on clean and oxygen covered Ru(001) [112]. The geometry of the chemisorbed formaldehyde η^2-phase had been identified by several early experiments on Ru and Zr catalysts [113, 114]. However, up to now, to the best of our knowledge the specification of η^2-phase formaldehyde on Cu is still missing both experimentally as well as theoretically. The change of the ν(CO) and $\delta(CH_2)$ vibrational modes reflects the stretching of the CO bond and the breaking of the C_{2v} symmetry of CH_2, respectively. It causes a rearrangement of the planar gas-phase geometry of CH_2O to a bend geometry. Compared to the physisorption and the η^1-chemisorption of formaldehyde, the η^2-phase has lost the π_{CO} character and the C_{2v} symmetry. The $1b_2$ and $5a_1$ orbitals are still identical, but the peaks are much broader. The non-bonding electron orbital $1b_1$ is split in two. In spite of the strong change, we can still assign the orbitals in terms of formaldehyde levels. The calculated formaldehyde chemisorption state can be successfully identified with the η^2-formaldehyde state found in EELS experiments. Because of its rearrangement, it is a

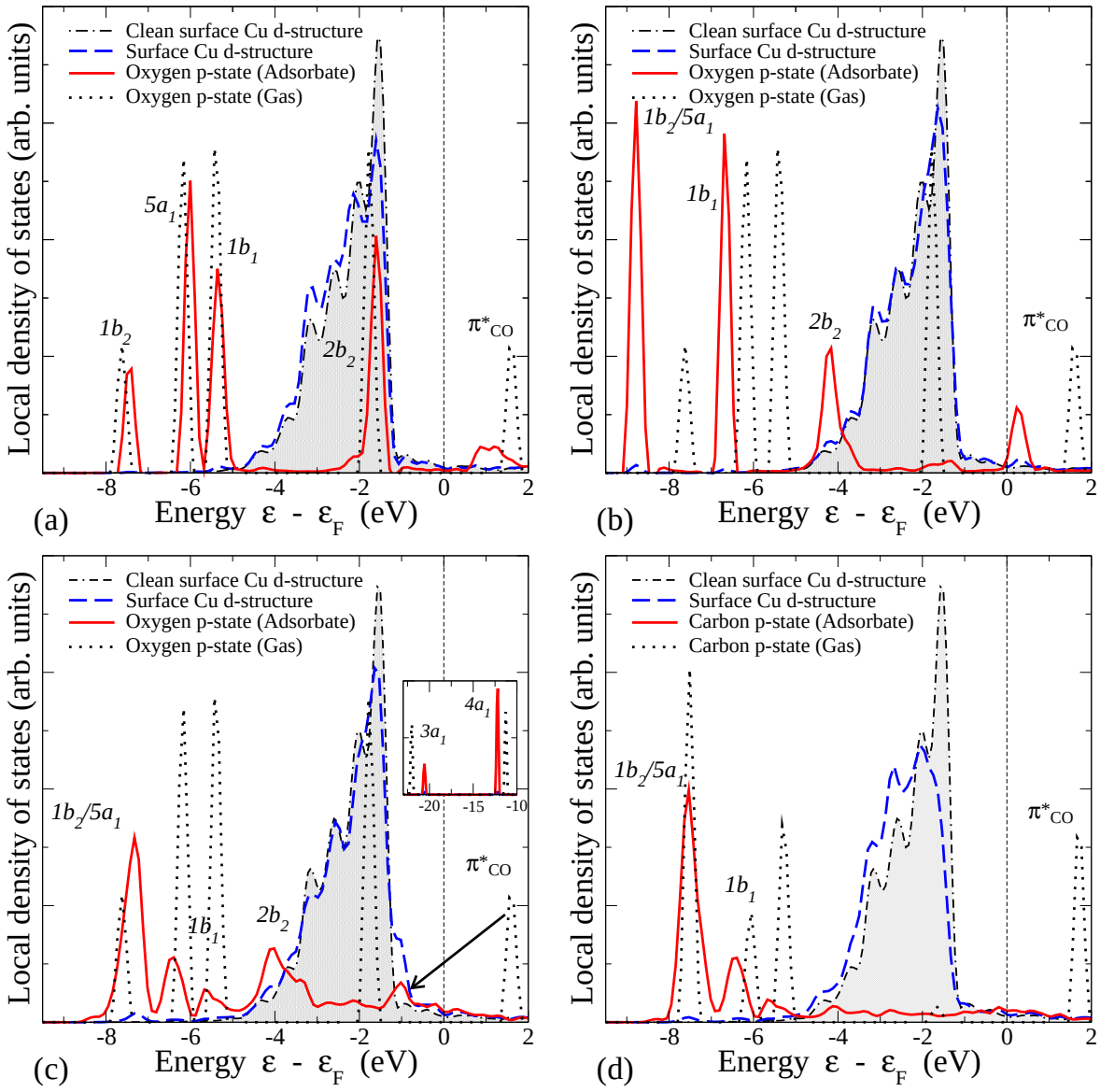

Figure 3.8: Local density of states of the oxygen p-state of adsorbed formaldehyde for (a) physisorption (b) η^1-phase chemisorption and (c) η^2-phase chemisorption on the clean Cu(110) surface. The carbon p-state of chemisorbed formaldehyde in the η^2-phase is plotted with the local d-band of the nearest Cu atom (Cu2 in Fig. 3.9) in (d). The hybridization of the anti-bonding state π^*_{CO} is increased upon the approach to the surface. This can be described by the Blyholder mechanism: back-donation from metal states into the anti-bonding π-type orbital of CO.

strong candidate for being an intermediate state for further dehydrogenation.

The case of carbon-dioxide (CO_2) is an example of back-donation to a close-shell molecule. XPS and HREELS experiments have found an anionic chemisorption state of CO_2 on polycrystalline Cu surfaces [115, 116]. The heat of adsorption of $CO_2^{\delta-}$ has been estimated to be 0.62 eV, whereas it is 0.19 eV for physisorption [117]. The anionic

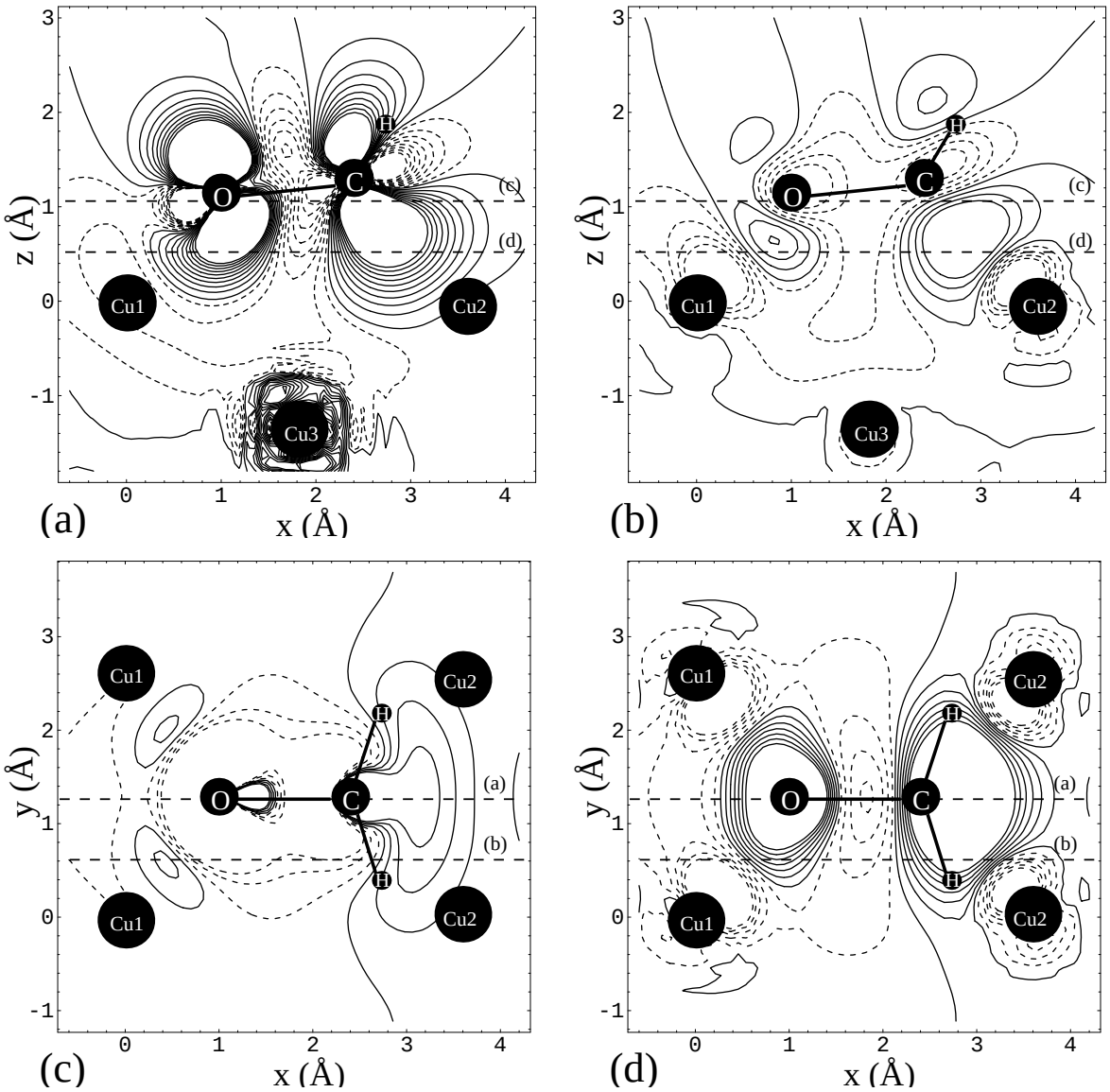

Figure 3.9: Charge density difference plots of chemisorbed formaldehyde on Cu(110). Side-views including the CO bond (a) and the intermediate position of the nearest Cu atoms (b). Top-views including the formaldehyde oxygen atom (c) and an intermediate position between the uppermost Cu atoms and formaldehyde (d). The dashed line indicate the positions of the perpendicular two-dimensional cuts. Solid lines represent charge accumulation and dashed line charge depletion.

adsorption on single-crystal surfaces is promoted by the co-adsorption of alkali metals, e.g. Cs or K, since alkali metals on Cu surface provide electrons for charge transfer to the CO_2 molecules. This confirms the validity of the back-donation model for filled π bond molecules.

Similarly, the filling of the formaldehyde anti-bonding π^*_{CO} orbital can also be described by the back-donation from the metal surface according to the Blyholder mech-

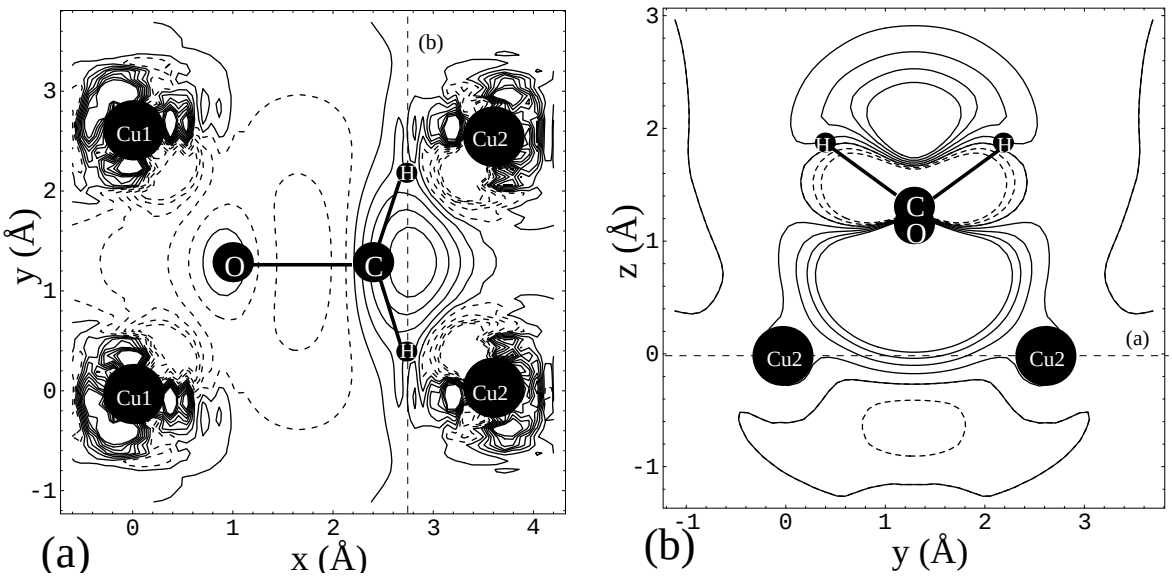

Figure 3.10: Charge density difference plots of chemisorbed formaldehyde on Cu(110). (a) Top view, (b) side view with the projections of the atomic positions included. The location of the 2-dimensional cuts is indicated by the dashed lines.

anism. The stretching of the CO bond is in good agreement with the predictions of the Blyholder model, the adsorption energy is 0.63 eV on Cu(110) and 0.70 eV on Cu(100). It is not sufficiently large to be interpreted as strong chemisorption. The relative small energy gain in adsorption comes from the cost of the CH_2 and CO bond deformation. The distortion energy of the η^2-phase adsorbate configuration is estimated to be 1.65 eV by performing calculations for the deformed molecule in the gas phase. The binding energy of the distorted formaldehyde is 2.28 eV on Cu(110), but most of this energy gain is compensated by the rearrangement of the chemical bonds.

The charge density difference plots in Fig. 3.9 illustrate the electron density depletion of the CO bond and its accumulation at the C and O ion sites. Figures 3.9a and 3.9c clearly show the CO bond weakening. Moreover, Figs. 3.9b and 3.9d indicate the direct chemical bonding of Cu-O and Cu-C. Cu ions act as an electron donor and carbon and oxygen as an acceptor. It implies that the η^2-formaldehyde is slightly anionic similar to case of CO_2 chemisorption.

The charge density difference at the surface Cu ions is illustrated in Fig. 3.10. The charge depletion of oxygen close to the Cu1 site is similar to the methoxy adsorption in Fig. 3.5. However, at the carbon atom close to the Cu2 site there is a charge accumulation. Interestingly, the surface charge localization leads to a strong Cu-C bond. It leads to a quasi C_{3v} symmetry of the adsorbed formaldehyde resembling a CH_3 configuration, Thus it leads to the resemblance of the geometric structures of η^2-formaldehyde and methoxy.

The promoting effect of co-adsorbed alkali metal, which was found in CO_2 adsorption over Cu, has not been investigated for formaldehyde adsorption, however, it is expected that co-adsorbed alkali metals promote the oxidation of formaldehyde to

CO_2. According to Wachs and Madix, there are two possible reaction mechanisms for adsorbed formaldehyde:

$$CH_2O^{(a)} + O^{(a)} \longrightarrow {CO_2}^{(g)} + {H_2}^{(g)} \tag{3.2}$$

$$CH_2O^{(a)} \longrightarrow CO^{(g)} + {H_2}^{(g)}. \tag{3.3}$$

In the presence of oxygen, the formaldehyde is converted to CO_2 according to Eq. (3.2). TPD experiments by Wachs and Madix had suggested formate (HCOO) as an intermediate state for the process [12]. In contrast, the formaldehyde oxidation without oxygen leads to CO desorption according to Eq. (3.3).

The importance of the two mechanisms Eqs. (3.2) and (3.3) becomes clearer when an oxygen covered surface is considered. We have prepared an oxygen covered surface in a (2×2)O/Cu(110) geometry. The oxygen rows are running in [001] direction and the coverage is $\theta_O = 0.5$. At high oxygen coverage, the surface will undergo an added-row reconstruction [118, 119]. The electronic properties of the CuO chain on the added-row surface are significantly different from isolated oxygen. However, in order to keep the simplicity and to focus on the contribution of pure oxygen, only the unreconstructed oxygen-covered Cu(110) surface is considered.

Interestingly enough, the energetically most favorable configuration is the η^1-phase on the oxygen covered surface. Furthermore, when atomic oxygen is located in the same row as the formaldehyde CO bond, the η^2-chemisorbed formaldehyde lost the Cu-C bonds. The co-adsorption of atomic oxygen leads to a surface charge redistribution with the electrons accumulated at the oxygen site. The low surface electron density attracts η^1-phase formaldehyde closer to the surface and induces a further energy gain. However, it also causes an electron depletion at the Cu-C bond of the η^2-phase formaldehyde. As a result, the Cu-C bond is weakened and the adsorption height of formaldehyde is increased. This is the reason why the η^1-phase contributes to the CO_2 desorption channel in Eq. (3.2). However, without the presence of surface oxygen the η^2-phase formaldehyde is considered as an intermediate state for CO desorption in Eq. (3.3). The rolling motion of η^2-phase formaldehyde is believed to lead to CH bond scissions. In this thesis, however, the dehydrogenation steps of formaldehyde to CO_2 or CO are not studied.

3.4 Methoxy super-structure

The sequential adsorption of oxygen and methanol produces predominantly methoxy adsorbates. STM images show that oxygen adatoms form a (2×1) structure. The presence of methanol reduces the size the oxygen-covered area while adsorbed methoxy forms super-structures separated from the oxygen islands [120, 121]. Terminal oxygen is believed to be more reactive than the centered oxygen in islands, because it is removed at first. This leads to the well-known methoxy induced (5×2) surface reconstruction [120, 121]. After further methanol oxidation, a methoxy $c(2 \times 2)$ super-structure has been detected with zigzag chains running in [001] direction. Eventually, methoxy forms islands with $c(2 \times 2)$ periodicity. The methoxy super-structures has been precisely determined by several STM experiments [120–124]. Furthermore, these

experiments find that oxygen islands and the $c(2 \times 2)$ methoxy structure were well separated, and that only a chain-like methoxy structure exists in the interspatial area.

The character of the pure methoxy $c(2\times2)CH_3O/Cu(110)$ and $c(2\times2)CH_3O/Cu(100)$ structure has been studied in detail by our DFT calculations. On Cu(110), adsorbed methoxy is located on pseudo (111) edge and long bridge sites with two different CO angles. At the pseudo (111) step edge, the $c(2 \times 2)$ structure leads to an energy gain of 0.06 eV/CH_3O with respect to the well separated (2×2) structure. At the long bridge site, the stabilization is 0.03 eV/CH_3O for both tilt angles.

When the methoxy coverage θ_{CH_3O} is increased to 0.5, the adsorbates try to maximize their intermolecular distance. The methoxy adsorbates in the $c(2 \times 2)$ structure are still well separated on Cu(110). The intermolecular interaction of methoxy is attractive, but very weak. In contrast, on Cu(100), the $c(2\times2)$ structure with methoxy at the hollow site is less stable by 0.13 eV/CH_3O. Interestingly enough, the $c(2\times2)$ structures are almost energetically degenerate at the hollow and bridge sites on Cu(100). Thus the stability of the adsorption sites depends on the coverage. In Sec. 3.2, we found that hydrogen co-adsorption induces a meta-stable methoxy adsorption configuration at bridge site. By increasing methoxy coverage, the same kind of meta-stable configuration is created.

The local adsorption geometry of methoxy in the $c(2\times2)$ structure is hardly changed from the low coverage (2×2) result listed in Table 3.3. The high coverage induces a slight buckling of the surface Cu atoms. A very detailed look at the charge density difference plot is shown in Fig. 3.11b. It illustrates the tiny redistribution of the electron density by forming the $c(2 \times 2)$ structure. The change of the electron density on each methoxy molecule is negligible. Hence, the stabilization of the methoxy super-structure is hard to explain in terms of charge density plots. The corresponding surface Cu d-LDOS is also plotted in Fig. 3.11a. According to the LDOS analysis, the surface d-band is slightly broaden in the $c(2 \times 2)$ structure. It reflects a stronger interaction between the Cu d-band and methoxy, which is, however, not visible in the LDOS of methoxy. Thus, the stabilization of the methoxy $c(2 \times 2)$ structure can hardly be explained by analyzing the LDOS or charge density difference plots.

Methoxy adsorption on the long bridge site still gives a stable configuration. The energy change is smaller than for the pseudo (111) step site adsorption, since methoxy

Lattice	Config	E_{ads}	ΔE_{ads}	$d_{n.n.}$	h_{Cu-O}	d_{Cu-O}	d_{CO}	d_{CH}	$\angle n_{CO}$
Cu(100)	hollow	−2.96	+0.13	3.64	1.25	2.19	1.45	1.10	0.7
	bridge	−2.85	+0.01	3.64	1.42	2.00	1.45	1.10	26.3
Cu(110)	pseudo fcc	−3.04	−0.06	4.46	1.43	1.95	1.44	1.10	35.0
	long bridge	−2.66	−0.03	4.46	1.21	2.03	1.45	1.10	21.5
	long bridge	−2.64	−0.03	4.46	1.23	2.02	1.44	1.10	0.5

Table 3.5: Molecular properties of the methoxy $c(2 \times 2)$ super-structure on Cu(110) and Cu(100) corresponding to a coverage of $\theta_{CH_3O} = 0.5$. The binding energy E_{ads} in the (2×2) structure and the further energy gain by forming the $c(2 \times 2)$ super-structure ΔE_{ads} are expressed in eV per molecule.

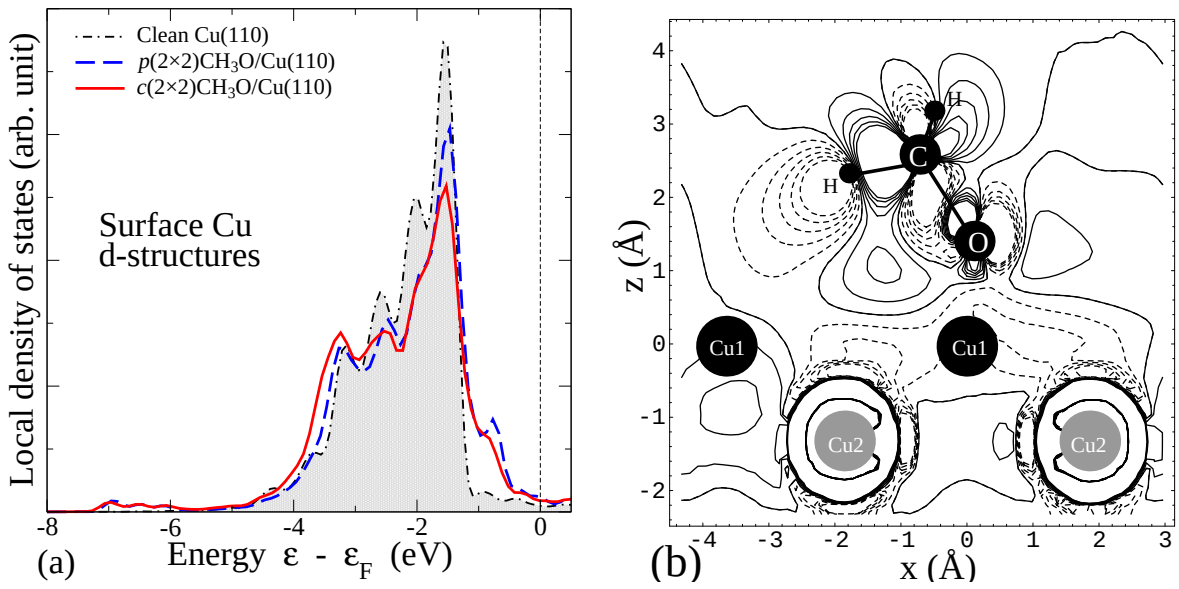

Figure 3.11: Local density of states and charge density difference plot for the formation of the methoxy $c(2 \times 2)$ structure on Cu(110). The scale of the contour lines is 10 times denser than for the charge density difference plot for the molecular adsorption, since the $c(2 \times 2)$ structure formation only leads to small changes of electron density.

at the long bridge induces a rather large rearrangement of surface Cu ions. For both methoxy tilt angles, the top Cu atoms relax in a zigzag pattern in $[1\bar{1}0]$ direction. Moreover, the tilt angle is increased to 21.5° which is partly promoted by the rearrangement of the top Cu atoms for the high methoxy coverage.

On the Cu(100) surface, the adsorption energy at the bridge site is lower than at the hollow site for the (2×2) structure. At a higher coverage, the hollow site is no more the most favorite adsorption configuration, however, it is a stable configuration which maintains a high symmetry.

The stability of the methoxy super-structure was also tested under the co-adsorption of atomic oxygen. The molecular properties of methoxy and co-adsorbed oxygen are listed in Table 3.6. The co-adsorption geometry is described in Fig. 3.12 where the methoxy coverage corresponds to $\theta_{CH_3O} = 0.5$ for the $c(2 \times 2)$ and $\theta_{CH_3O} = 0.25$ for the (2×2) structures. The adsorption site ph1 is below the C atom and ph2 below the O atom of the adsorbed methoxy. The zigzag chain has a $c(2 \times 2)$ structure and is running in $[1\bar{1}0]$ direction.

The co-existence of methoxy and oxygen results in large repulsive intermolecular interactions. At a low methoxy coverage corresponding to a (2×2) structure, which is described by the dash-dotted rectangle in Fig. 3.12 with methoxy at the corners, the presence of oxygen leads to a repulsive interaction of 0.78 eV for oxygen in a $c(2 \times 2)$ structure. Since methoxy is too close to the oxygen atoms, a large repulsive interaction results. Strong adsorption geometry changes are a consequence of this high oxygen coverage. The system lowers its total energy by maximizing methoxy-oxygen distance. The preferred structure is indeed a zigzag chain structure for oxygen in the

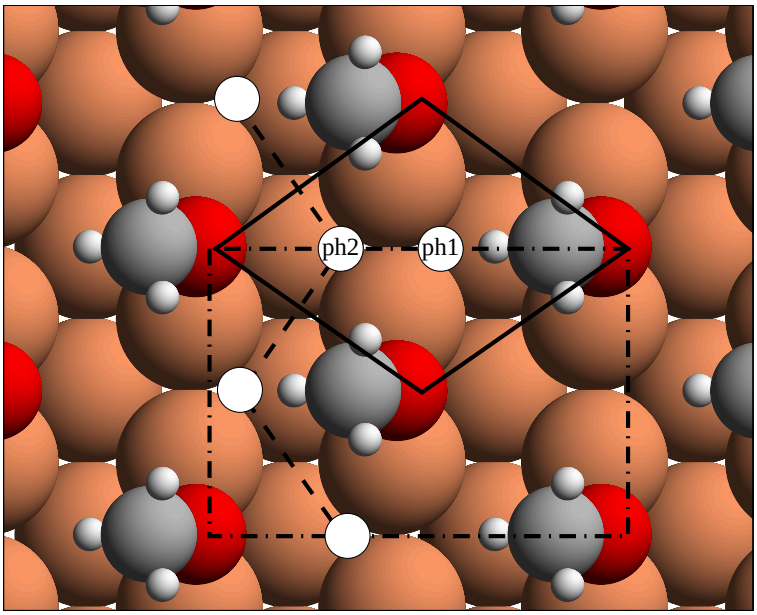

Figure 3.12: Geometry of the methoxy superstructure and co-adsorbate sites. The solid line denotes the $c(2 \times 2)$ supercell and the dash-dotted line the (2×2) structure. The co-adsorption sites ph1 and ph2 correspond to pseudo (111) fcc hollow dash-dotted sites, the dashed line illustrates the zigzag oxygen (2×1) structure in the $[1\bar{1}0]$ direction.

$[1\bar{1}0]$ direction. In this configuration, adsorbed methoxy is attracted to the second layer Cu atoms and the CO bond is oriented close to the surface normal. As a result, methoxy is located very close to the surface.

For the $c(2 \times 2)$ methoxy structure, at a coverage of $\theta_{CH_3O} = 0.5$, oxygen co-adsorption induces a large repulsion even at low coverages of oxygen. At the ph1 site, oxygen pushes the nearest two methoxy molecules outward of the pseudo (111) plane.

CH_3O	Adsorbate	ΔE	$d_{\text{n.n.}}$	$h_{\text{Cu-O}}$	$\angle n_{\text{CO}}$	$d_{\text{O-Ads}}$	Geo.
$c(2 \times 2)$	(2×2)O	0.83	3.91/5.05	1.46/1.40	42.5/25.8	3.07	ph1
	(2×2)O	0.71	3.87/5.10	1.41/1.45	37.8/36.6	2.83	ph2
	(2×1)O	1.39	3.25/5.96	0.96/1.41	2.8/33.4	3.15	$[1\bar{1}0]$
(2×2)	(2×2)O	0.14	5.15	1.48	35.1	2.89	ph2
	(2×1)O	0.23	5.15	1.06	0.3	3.46	$[1\bar{1}0]$
	$c(2 \times 2)$O	0.78	5.15	1.47	40.3	2.64	ph2

Table 3.6: Molecular properties of oxygen co-adsorbed with methoxy in the $c(2 \times 2)CH_3O$ and (2×2) structures. The adsorption sites of oxygen are specified in Fig. 3.12. The intermolecular repulsion ΔE is defined as the energy difference of methoxy adsorption at the clean and the O-covered surface. Under oxygen co-adsorption, the methoxy adsorption geometry becomes distorted. For high oxygen coverages of $\theta_O = 0.5$, the methoxy adsorbates lose their original 2×2 and $c(2 \times 2)$ periodicity.

This results in a metastable methoxy adsorption configuration with the CO bond tilt angle enlarged to 42.5°. In contrast, at the ph2 site, oxygen pushes the two nearest methoxy molecules inward of the pseudo (111) plane which causes no significant change of the methoxy adsorbate geometry. As a result, the ph2 oxygen adsorption induces smaller repulsion than the ph1 adsorption. The high-coverage oxygen adsorption in the chain structure causes a very large repulsion and a symmetry change of the methoxy adsorbates. On the highly oxygen-covered surface, the methoxy $c(2 \times 2)$ structure is broken and changed into a (2×1) chain like structure running in $[1\bar{1}0]$ direction. It is the same trend as found for the (2×2) structure, only the chain periodicity is now $c(2 \times 2)$. The methoxy adsorbates pushed outward of the pseudo (111) plane form the same geometry as in the case of the $(2\times2)CH_3O$ structure in the pressure of a $(2\times1)O$ structure.

The co-existence of methoxy and oxygen leads to a large repulsive interaction. This explains the fact that oxygen and methoxy islands on Cu(110) surface are well-segregated, as found in STM experiments. Moreover, it indicates that the methoxy oxidation is not promoted by surface oxygen. When methoxy is produced on the surface by the support of surface oxygen, it will propagate immediately to minimize its energy through maximizing the methoxy-oxygen distance. The methoxy adsorbates form a $c(2 \times 2)$ structure when the coverage is high enough. Growing $c(2 \times 2)$ islands expel isolated oxygen atoms from their interior.

STM experiments show that first the (5×2) reconstruction structure vanishes and then the chain-like structure shrinks. The $c(2 \times 2)$ structure remains longest on the surface [120, 121]. Furthermore, the methoxy structure is disturbed by continuing oxygen supply [124]. Additional oxygen adsorption leads to an instability of the methoxy superstructure and promotes further oxidation or thermal desorption. However, oxygen adsorption is believed to promote the forward reaction to formaldehyde whereas hydrogen promotes the backward reaction resulting in methanol desorption.

3.5 Co-adsorption of methanol and oxygen

A precoverage of oxygen is believed to promote the methanol oxidation on Cu surfaces [12, 82], especially as far as the hydroxyl bond breaking is concerned. In this section we discuss DFT calculations on oxygen precovered Cu(100) and Cu(110) surfaces including adsorbate induced surface relaxation. The oxygen atoms are located in their most favorable sites, which are the hollow sites on Cu(100) and the pseudo three fold hollow sites on Cu(110) within a coverage $\theta_O = 0.25$. The initial methanol geometries are selected as for the adsorption on the clean surface as listed in Table 3.2.

The molecular properties of methanol adsorption on oxygen covered Cu surfaces are listed in Table 3.7. On O/Cu(100), the methanol physisorption energy is increased by the presence of surface oxygen. Even though methanol is located far above the surface, the total energy is lowered. However, no spontaneous hydroxyl bond breaking is found on the Cu(100) surface for various configurations. Interestingly, the methanol induced surface re-relaxation is very strong for the O_{top}-H_{hl}/O_{hl}/Cu(100) adsorption configuration. It leads to a (111)-like surface deformation and a close attraction of

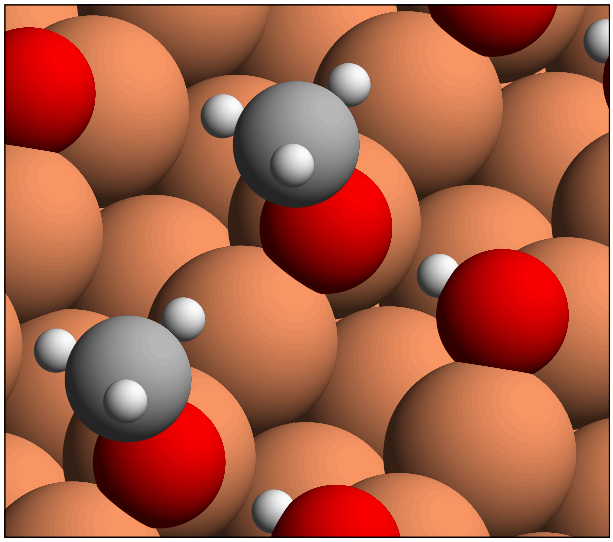

Figure 3.13: Geometry of neighboring methoxy and hydroxyl after the spontaneous methanol hydroxyl bond decomposition on O/Cu(110). Methoxy is located at the pseudo (111) step edge site and hydroxyl is located at the pseudo fcc hollow site of the lower terrace. The surface hydroxyl bond is oriented towards the methoxy oxygen site illustrating a still remaining CH_3O-OH interaction. This configuration is associated with a large adsorption energy of −1.53 eV.

methanol to the Cu atom. This demonstrates that oxygen is very stable on Cu(100) and does not easily take part in the methanol oxidation by the formation of a surface hydroxyl bond. This result, however, is at variance with previous experiments that found methanol oxidation at low temperatures over O/Cu(100) [93, 125].

The reactivity has been tested by changing the adsorbate coverage. For the lower coverage, a (3×2) unit cell was used. In this low coverage situation with $\theta_O = 0.17$, methanol is physisorbed within a O_{hl}-H_{br} configuration. The adsorption energy is

Lattice	Config	E_{ads}	h_{Cu-O}	d_{Cu-O}	d_{CO}	d_{OH}	$d_{O-O_{ad}}$	Relax
Cu(100)	O_{top}-H_{hl}/O_{hl}	−0.47	1.94	2.02	1.43	1.05	2.47	T
	O_{top}-H_{hl}/O_{hl}	−0.34	2.64	2.64	1.44	1.01	2.64	F
	O_{hl}-H_{br}/O_{hl}	−0.32	2.33	2.90	1.44	1.01	2.68	T
	O_{hl}-H_{br}/O_{hl}	−0.30	3.15	3.41	1.44	1.01	4.41	F
Cu(110)	O_{sb}-H_{hl}/O_{ph}	−1.52	1.43	1.99	1.45	1.73	2.74	T

Table 3.7: Molecular properties of methanol adsorption on oxygen precovered Cu surfaces with an oxygen coverage of $\theta_O = 0.25$. The adsorption energy E_{ads} is expressed in eV and the adsorption geometry is characterized by the height and distance from the nearest neighbor Cu atoms. The most favorable oxygen adsorption sites were selected which are the hollow site on Cu(100) and the pseudo fcc hollow site on Cu(110). The last column denotes whether surface relaxation was included (True) or not (False).

slightly increased compared to $\theta_O = 0.25$ when the surface rerelaxation is not included. In this configuration, the distance from the nearest Cu atom d_{Cu-O} is 2.65 Å. The distance is 0.25 Å shorter than for $\theta_O = 0.25$ (see Table 3.7). It shows that the methanol reactivity depends on the oxygen coverage.

Compared to the isolated adsorbates, the CH_3O+OH structure within a (2×2) surface unit cell is energetically unfavorable, indicating again the repulsive interaction of methoxy with other adsorbates. On the (3×2)O surface, the energy is lower by 0.1 eV, indicating a smaller repulsion. The total energy change from methanol to methoxy and hydroxyl bonds is estimated to be 0.5 eV for the (3×2) unit cell. This small energy difference already implies that the spontaneous conversion of methanol to methoxy is rather unlikely on the O/Cu(100) surface.

On the contrary, on oxygen-covered Cu(110), the methanol hydroxyl bond is spontaneously broken with a large decomposition energy gain. The stable configuration of neighboring methoxy and hydroxyl is illustrated in Fig. 3.13. Methoxy is located in a pseudo (111) step edge site and OH in a fcc hollow site of the lower terrace. This configuration corresponds to an adsorption energy of -1.53 eV which is significantly larger than on O/Cu(100). It is partially based on an attractive methoxy-hydroxyl interaction. There is a remaining attractive interaction of 0.32 eV in the structure illustrated in Fig. 3.13 compared to well-separated adsorbed methoxy and hydroxyl.

The high reactivity of the O/Cu(110) surface can be interpreted as a step effect [126]. The geometry of step sites increases the reactivity due to the low coordination number of the step atoms. Moreover, at the step site it is easier for adsorbates to find an energetically favorable adsorption geometry. The GGA-PW91 calculations of the dissociation barrier of N_2 over Ru(0001) by Logadóttir and Nørskov show a considerable reduction at step [126]. The same electronic structure and geometric contribution is expected on the O/Cu(110) step edge. Interestingly enough, in this configuration the methoxy adsorption geometry is very close to the methanol physisorption geometry on clean Cu(110). It gives an extra advantage for the OH bond dissociation: methoxy easily finds the final state geometry and the dissociated hydrogen atom diffuses efficiently to the atomic oxygen site.

The LDOS of the surface adsorbates in Fig. 3.13 is plotted in Fig. 3.14. The Cu-O interaction peaks are as expected for both methoxy and hydroxyl. The methoxy $2e$ orbital and the Cu-O_{ad} peak are well split by the Cu d-band. The methoxy-hydroxyl attractive interaction leads to the O-OH peak. This is derived from the alignment of the methoxy oxygen p-state (solid line), hydroxyl oxygen p-state (dotted line) and hydroxyl hydrogen s-state (thin sold line). The anti-bonding O-OH* interaction has no hydroxyl s-electron contribution. The hydroxyl bond orientation with respect to the methoxy oxygen site in Fig. 3.13 confirms these findings; on the clean surface the bond was oriented along the surface normal. The interaction maximizes the distance between CH_3O and OH, but at the same time minimizes the CH_3O-H distance. Furthermore, the CH_3O-OH interaction induces a stabilization of the non-bonding electrons. The methoxy $5a_1$ orbital becomes lower than the split $1e$ orbital peaks. On the clean surface, it was located between the $1e$ peaks.

In Fig. 3.14b, the methoxy LDOS for clean Cu(110) is compared to the one for OH-covered Cu(110). The dotted line represents the clean surface methoxy LDOS and

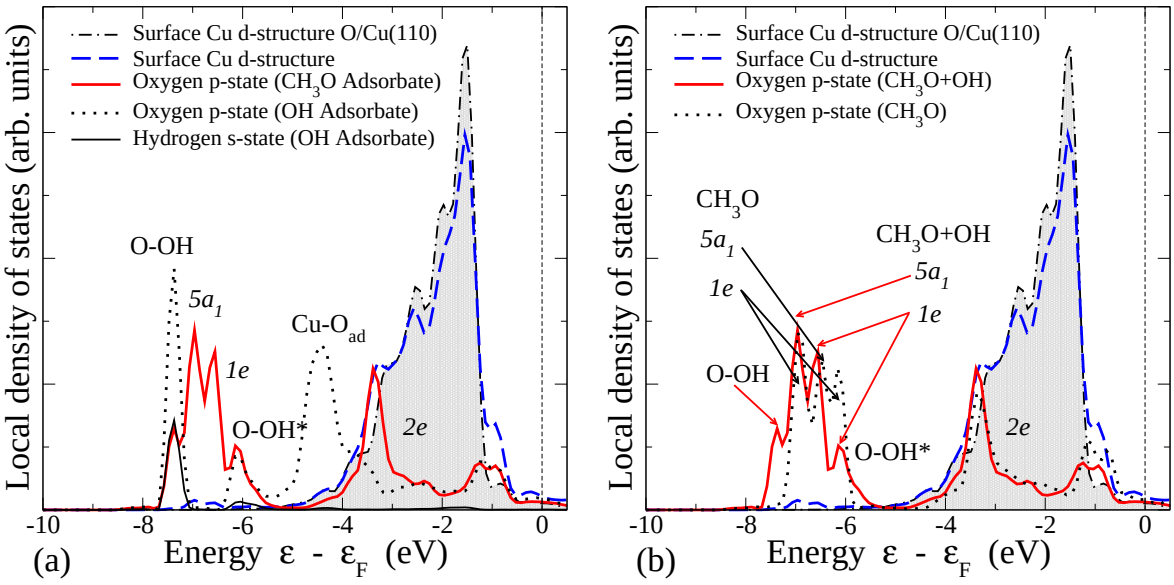

Figure 3.14: Local density of states of spontaneously decomposed methanol over oxygen covered Cu(110): (a) CH_3O+OH/Cu(110) and (b) comparison with the clean surface adsorbate CH_3O/Cu(110). The methoxy-hydroxyl interaction forms new O-OH peak and its anti-bonding contribution O-OH* in (a). The ordering of the $5a_1$ and $1e$ orbitals is reversed compared to the methoxy adsorbate on the clean surface in (b).

the solid line the methoxy-hydroxyl system. The $2e$ orbitals are almost identical in the two configurations. This means that the CH_3O-Cu bond is not disturbed by the hydroxyl co-adsorption. The modification of the LDOS is characterized by the creation of a O-OH peak and the $1e$ peak down-shift caused by the O-OH* interaction.

In conclusion, the difference between O/Cu(100) and O/Cu(110) is that the surface adsorbates methoxy and hydroxyl interact repulsively on Cu(100) but attractively on Cu(110). This interaction depends sensitively on the surface geometry and the adsorption configuration, in particular for open step-like structures. The absence of open structures on oxygen-covered Cu(100) and Cu(111) suppresses the hydroxyl bond breaking.

Chapter 4

Reactivity on stretched surfaces

Recently the relationship between the catalytic reactivity of binary Cu/ZnO catalysts and the strain of the copper in the Cu/ZnO system has been intensively discussed [127]. The surface strain influence on the surface reactivity has been rationalized in terms of the d-band model [128, 129]. At the expanded substrate, the overlap between the Cu atoms is reduced, which leads to a narrowing of the d-band. In the case of transition metals, the d-band is not completely occupied. If the d-band is more than half-filled, charge conservation causes an up-shift of the d-band upon its narrowing [129, 130]. The higher d-band center usually causes a higher reactivity [128]. Surprisingly, the GGA-PW91 calculations for oxygen adsorption on strained Cu(111) surface by Xu and Mavrikakis were interpreted successfully within the d-band model, in spite of the fact that the Cu d-band is fully occupied and a d-band up-shift should not be expected [131].

In this chapter, a detailed analysis of the hydrogen adsorption and the reactivity of the reaction intermediates in methanol oxidation over expanded substrates will be presented in terms of the d-band model. The hydrogen-Cu substrate system has served as a benchmark system for the study of the interaction of molecules with surfaces, both experimentally [132–137] as well as theoretically [138–147]. Thus the calculations of hydrogen reactivity over strained copper might contribute to a microscopic understanding of the reactivity of real binary catalysts.

4.1 Hydrogen adsorption in d-band model

The concept of *reactivity* in surface problem is usually associated with the binding energy between adsorbate and surface. A larger binding energy denotes a more reactive system. An early model to describe the surface reactivity was based on the concept of Pauli repulsion. The Pauli repulsion of the s-electrons of adsorbing H_2 is reduced by the availability of empty d-states near the Fermi level. Thus the Fermi level is correlated with the reactivity of metal [148, 149]. Unfortunately, this simple model

was too poor to describe surface reactions properly. Here we take into account the prominent d-band model proposed by Hammer and Nørskov [128].

The d-band model describes the interaction of molecular adsorbates and transition or noble metal via separate sp-state and d-band contributions. The interaction of the sp-bands leads to an energy renormalization of the adsorbate energy levels. In the case of H_2 interacting with a sp-metal surface (Aluminum or jellium), both the bonding (σ_g) and the antibonding (σ_{u^*}) states are renormalized. The d-band contributes to the interaction energy by the d-band center hybridization with the renormalized hydrogen σ_g and σ_{u^*} orbitals. The extra energy gain by the d-band contribution is expressed as a second order perturbation term,

$$\delta E \sim \frac{V^2}{|\varepsilon_d - \varepsilon_\sigma|}, \tag{4.1}$$

where $V \ll |\varepsilon_d - \varepsilon_\sigma|$ and the coupling matrix element V is $\langle \phi_\sigma | H | \phi_{\mathbf{k}} \rangle$. The whole interaction energy due to the d-band of the H_2-metal surface system including bonding and anti-bonding orbitals is expressed in [128] as

$$\delta E_d^{H_2} = -2\frac{V^2}{\varepsilon_{\sigma_{u^*}} - \varepsilon_d} - 2(1-f)\frac{V^2}{\varepsilon_d - \varepsilon_{\sigma_g}} + \alpha V^2 \tag{4.2}$$

where f is the d-band filling factor of the metal. ε_d denotes the center of the surface d-band, and ε_{σ_g} and $\varepsilon_{\sigma_{u^*}}$ represent renormalized bonding and antibonding levels. The coupling matrix element V depends on the distance between the interacting atoms. It usually decreases rapidly with increasing distance. Coupling matrix elements of hydrogen and transition or noble metal atoms interaction have been approximated by a simple $1/r^3$ dependence in Hammer and Nørskov's work [128, 130]. If the surface ions are nonequivalent, then the d-band contribution is replaced by the weighted sum over the corresponding atoms.

The first term in Eq. (4.2) describes the energy gain due to the attractive interaction of the H_2 antibonding level with the d-band. The energy gain of the σ_g-d interaction depends on the d-band filling in the second term. In noble metals, the d-states are fully occupied, thus the filling factor is $f = 1$. Therefore the contribution of the σ_g-d interaction will vanish for noble metals, such as Cu. The last term is the energetic cost of the orthonormalization between the molecular and the substrate states.

In the case of the H_2/Cu system, the d-band is fully occupied and located 2 eV below the Fermi energy. Hence the d-band contribution for the H_2/Cu system can be simplified to

$$\delta E_d^{H_2/Cu} = -2\frac{V^2}{\varepsilon_{\sigma_{u^*}} - \varepsilon_d} + \alpha V^2. \tag{4.3}$$

The original version of the d-band model [128] included the factor of $(1-f)$ in the attractive term of Eq. (4.2). However, later it turned out that irrespective of the filling factor there is an attractive contribution of the σ_g-d interaction [103, 150]. Moreover there is a linear relationship between the d-band center shift and the change in the chemisorption strength of atomic hydrogen on metal surfaces,

$$\delta E_d^H = -\frac{V^2}{|\varepsilon_d - \varepsilon_H|^2}\delta\varepsilon_d, \tag{4.4}$$

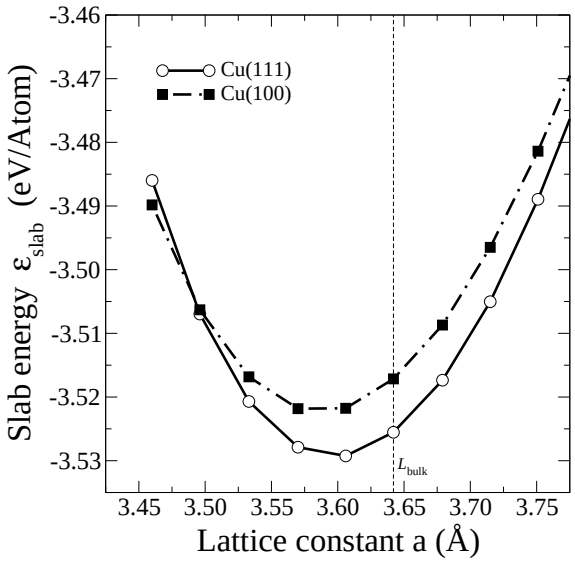

Figure 4.1: Slab energy per atom as a function of the lateral lattice strain for Cu(100) and Cu(111) surfaces. The Cu(100) and Cu(111) slabs consist of 5 and 4 layer atoms, respectively. The anisotropic distortion of the crystal leads to an energy minimum at a lower position than the bulk value. The energy per atom of the close-packed (111) slab is lower than for the more open (100) slab and closer to the bulk energy of Cu.

if $\delta\varepsilon_{\mathrm{d}} \ll |\varepsilon_{\mathrm{d}} - \varepsilon_{\mathrm{H}}|$. This can be understood in terms of the Newns-Anderson model [103]. The position of the renormalized hydrogen 1s adsorption resonance ε_{H} entering Eq. (4.4) is a strongly varying function of the distance of the hydrogen atom from the surface according to jellium calculations [151, 152]. It drops from 1 eV below the Fermi energy at a distance of 1.2 Å to 6 eV below the Fermi energy at a distance of 0.4 Å. Still, the Newns-Anderson model shows that an upshift of the d-band center causes a stronger bonding of adsorbates with their crucial renormalized adsorption states well below the Fermi level [103], even for a filled d-band.

The slab energy per atom as a functions of the lattice strain is illustrated in Fig. 4.1. It shows that the energy of the close-packed Cu(111) slab increases steeply under slab compressing, and crosses the Cu(100) curve at -4% compression. The high electron concentration of Cu(111) leads to a stronger repulsion. The energy minimum of the strained slab was found at a smaller interatomic distance than the equilibrium bulk value.

Strained substrates are prepared with lateral lattice constants modified by -3% and $+2\%$. The two upper most layers are fully relaxed. The lateral lattice strain causes modifications in the distances of the relaxed layers. Table 4.1 lists the layer distances of Cu(111) and Cu(100) as a functions of the strain. The top layer positions are shifted outward on the compressed substrate since the electron density is enhanced. On the other hand, we find an inward relaxation on the expanded substrate. The second layer position of the close-packed Cu(111) surface is hardly influenced by the strain, Cu(111) has almost bulklike features already in the second layer.

The local d-band density of strained Cu(111) surfaces and its variation are plotted in

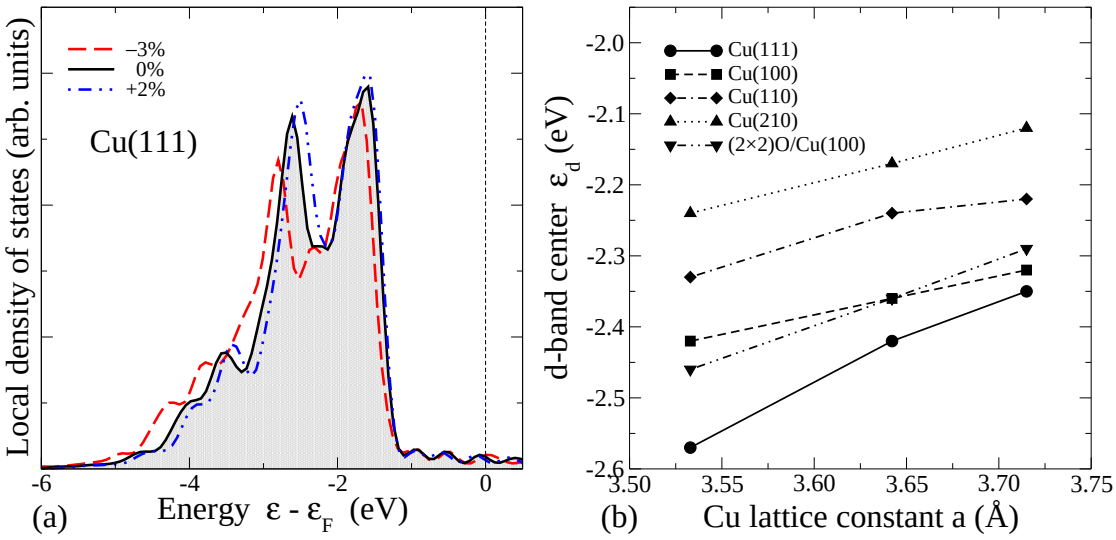

Figure 4.2: Local density of states at the uppermost layer of Cu(111) as a function of the lattice strain (a). The d-band center ε_{d} of the surface layer with respect to the Fermi energy as a function of the lattice strain for different copper surface terminations. It is determined from the d-band density of states n_{d} by $\varepsilon_{\mathrm{d}} = \int dE\, E\, n_{\mathrm{d}}(E) / \int dE\, n_{\mathrm{d}}(E)$ (b).

Fig. 4.2a. The d-band width decreases for increasing lattice constant, as follows from simple tight-binding considerations due to the reduced overlap. In fact, the d-band center of the uppermost Cu(111) layer shifts up with increasing lattice constant, in agreement with previous calculations [131]. However, this upshift cannot be explained by the simple argument of charge conservation as in the case of a transition metal with a partially filled d-band. As Fig. 4.2a indicates, the upper edge of the local Cu d-band at the surface is apparently pinned with respect to the Fermi energy. Because of this pinning the band narrowing causes an upshift of the d-band center.

The d-band center ε_{d} as a function of the lattice strain for different Cu surface terminations are plotted in Fig. 4.2b. The first fact that is obvious is that the more open the surface, i.e., the less coordinated the surface atoms, the higher the d-band

Lattice	a/a_{eq}	Δ_{12}	Δ_{23}	ε_{d}	$\Delta\phi$
Cu(111)	0.97	1.02	1.03	−2.57	
	1.00	1.00	1.02	−2.42	
	1.02	0.97	1.02	−2.35	
Cu(100)	0.97	1.01	1.04	−2.42	4.63
	1.00	0.97	1.01	−2.36	4.52
	1.02	0.94	0.97	−2.32	4.47

Table 4.1: Height difference ($\Delta_{ij} = (h_i - h_j)/d_{eq}$) of the Cu slabs as a function of the lateral lattice constant as a result of relaxation. On compressed surfaces, the top atoms move outwards and on expanded surface inwards.

center. Secondly, the shift of the d-band center is much larger for the Cu(111) surface than for the Cu(100) or Cu(110) surface. The local density of states of the close-packed Cu(111) surface is much more bulk-like compared to the more open Cu(100) surface. This demonstrates that the effect of the lattice strain on the electronic structure at an already open, less coordinated surface is less pronounced than for a close-packed surface.

According to the d-band model the atomic hydrogen binding energies on Cu should increase for expanded surfaces while the dissociation barrier should become smaller for increasing lattice constants which usually leads to a higher reactivity. Furthermore, the model should also be applicable for reaction intermediates of the methanol oxidation.

4.2 Chemisorption of atomic hydrogen on Cu

Atomic hydrogen adsorption energies are determined as a function of the lattice strain at the high-symmetry sites of the Cu(111), Cu(100), Cu(110), Cu(210) and the oxygen-precovered (2×2)O/Cu(100) surfaces. All hydrogen adsorption energies have been obtained for a surface coverage of $\theta_{\mathrm{H}} = 0.25$. For higher hydrogen coverage it turned out that the results were influenced by the mutual repulsive interaction between the hydrogen atoms. For $\theta_{\mathrm{H}} = 1$, we found an increase in the atomic binding energy upon lattice expansion which was simply due to the reduced repulsion between the adsorbates. For the unstrained surfaces, our results compare well with previous calculations in a similar setup within the typical uncertainty of DFT calculations of ± 0.1 eV [153, 154].

As far as the general site dependence of the hydrogen adsorption energies on the low-index copper surfaces is concerned, we observe that hydrogen prefers to be located at the high-coordination adsorption sites. This is also true for the Cu(110) surface. Note that the hollow site at the (110) surface corresponds to adsorption on top of the second layer atom in the trough so that this site is effectively also a low-coordination adsorption site. The most favorite site on the (110) surface is the pseudo three fold hollow site on both unstrained and expanded slabs. However, on the compressed surface, the short bridge site shows the largest adsorption gain. The hydrogen-surface distance is larger on the compressed surface. On the pseudo-threefold hollow site of the (110) surface, an adsorption symmetry change occurs. The symmetry of the hydrogen adsorption configuration on the pseudo-threefold hollow site becomes broken upon the compression of the slab and the increase of the hydrogen adsorption height. As a result, hydrogen is placed on the bridge site of the pseudo (111) surface. This adsorption configuration has two nearest Cu atoms. An adsorption symmetry change is also found for the long bridge site of the (110) surface. On the expanded substrate, hydrogen is attracted further towards the surface, and the second layer copper ions become the nearest neighbors. The adsorption symmetry is close to the one for the short bridge site.

According to the d-band model, the interaction between a hydrogen atom and the copper d-band should be repulsive, hence one would not expect that it is energetically favorable to build up many bonds between the hydrogen 1s and the Cu d states. On the other hand, the delocalized Cu sp states lead to a strong attraction of the hydrogen towards the surface. At the high-coordination sites, the hydrogen atom can minimize

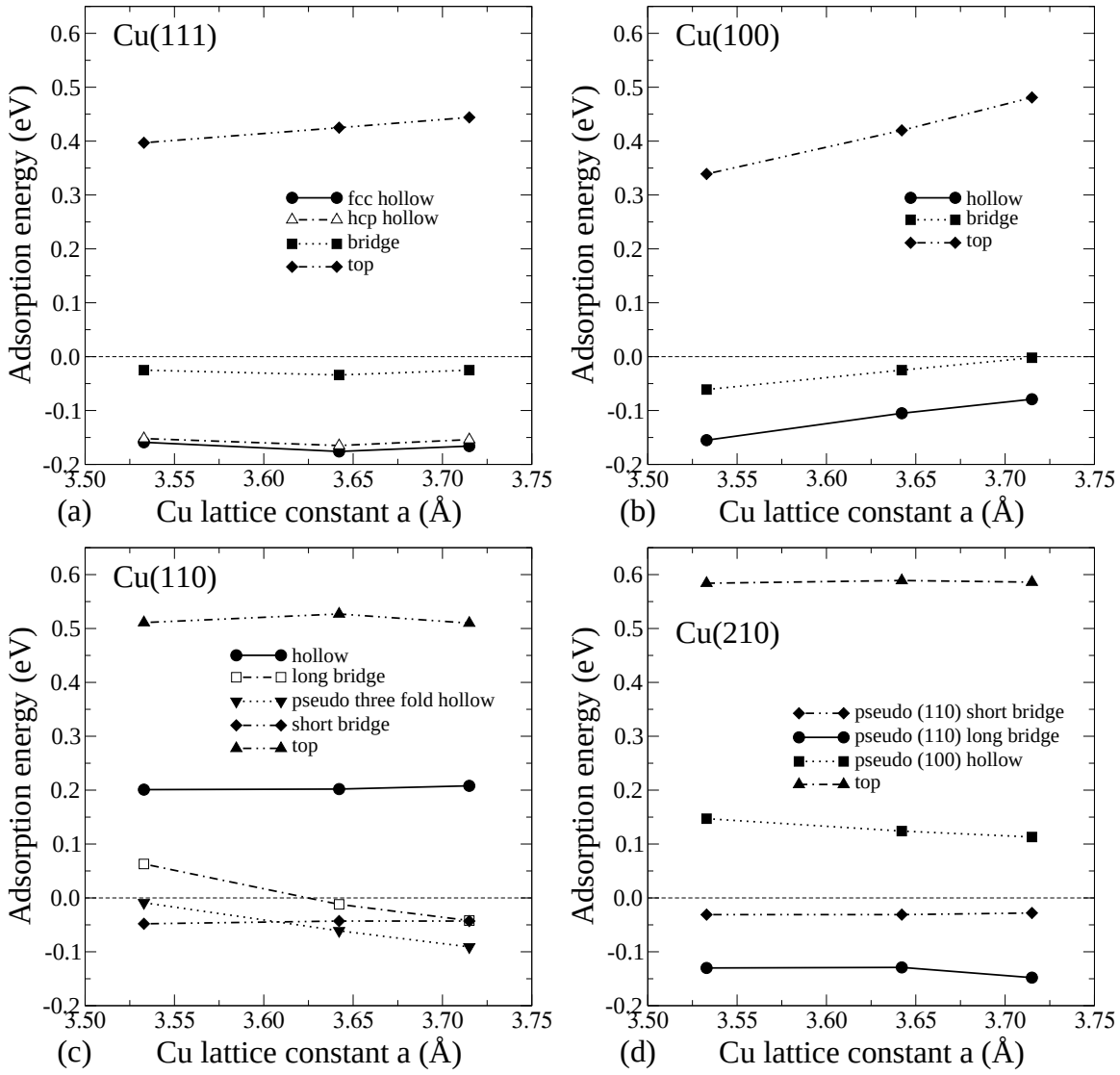

Figure 4.3: Atomic hydrogen adsorption energies as a function of the lattice strain at the high-symmetry points of (a) Cu(111), (b) Cu(100), (c) Cu(110) and (d) Cu(210).

its distance to the surface plane while keeping a maximum distance to the nearest Cu atom. This is illustrated in Table 4.2 where we have listed the height $h_{\mathrm{Cu-H}}$ of the adsorbate position with respect to the uppermost Cu plane and the distances $d_{\mathrm{Cu-H}}$ between the hydrogen atom and the nearest Cu atom in addition to the adsorption energies for the Cu(111) and Cu(100) surfaces.

For a quarter monolayer of hydrogen on clean Cu surfaces, there is no clear trend in the atomic adsorption energy as a function of lattice strain, as Fig. 4.3 demonstrates. On Cu(111) (Fig. 4.3a), the adsorption energies at the threefold hollow and the bridge sites are roughly independent of the lattice strain, as expected from the d-band model. At the top site, however, where hydrogen adsorption is endothermic with respect to the free hydrogen molecule in the gas phase, we even find a stronger repulsion for the

Lattice constant (Å)	Lattice strain	Cu(111) fcc hollow E_{ads}	fcc hollow h	fcc hollow $d_{\mathrm{Cu-H}}$	hcp hollow E_{ads}	hcp hollow h	hcp hollow $d_{\mathrm{Cu-H}}$	Bridge E_{ads}	Bridge h	Bridge $d_{\mathrm{Cu-H}}$	Top E_{ads}	Top $h = d_{\mathrm{Cu-H}}$
3.533	−3%	−0.159	0.976	1.741	−0.152	0.977	1.742	−0.025	1.102	1.666	0.397	1.526
3.642	0%	−0.176	0.919	1.748	−0.165	0.931	1.754	−0.034	1.060	1.668	0.425	1.525
3.715	+2%	−0.166	0.878	1.753	−0.154	0.883	1.751	−0.025	1.032	1.670	0.444	1.527

		Cu(100) Fourfold hollow E_{ads}	Fourfold hollow h	Fourfold hollow $d_{\mathrm{Cu-H}}$	Bridge E_{ads}	Bridge h	Bridge $d_{\mathrm{Cu-H}}$	Top E_a	Top $h = d_{\mathrm{Cu-H}}$
3.533	−3%	−0.155	0.638	1.878	−0.061	1.096	1.662	0.339	1.530
3.642	0%	−0.105	0.544	1.901	−0.025	1.046	1.659	0.420	1.530
3.715	+2%	−0.079	0.434	1.908	−0.002	1.015	1.660	0.481	1.532

Table 4.2: Atomic hydrogen adsorption energies E_{ads}, adsorption height h and nearest-neighbor distance $d_{\mathrm{Cu-H}}$ between hydrogen and copper atoms on various high-symmetry adsorption sites on Cu(111) as a function of the lattice strain. Energies are given in eV while distances are given in Å.

expanded substrate, or in other words, a larger attraction at the compressed surface, in contrast to the trends in adsorption energies as a function of lattice strain usually observed [129, 131]. On Cu(100) (Fig. 4.3b), this unexpected dependence of the adsorption energies on lattice strain is even obtained at all high-symmetry adsorption sites, whereas on Cu(110) (Fig. 4.3c) and Cu(210) (Fig. 4.3d) the binding energies are either constant or increase upon lattice expansion. Apparently, the predictions of the d-band model are only fully confirmed for hydrogen adsorption at the Cu(110) and Cu(210) surfaces. However, these results are partially influenced by the change in the symmetry of the adsorption site.

In recent molecular beam experiments of the O_2 adsorption on uniaxially stressed Cu(100) surfaces, lattice stress was found to enhance the O_2 adsorption for kinetic energies below 250 meV but to suppress it for energies above 250 meV. Our result that the dependence of the adsorption energies on lattice strain varies between different adsorption sites might provide an explanation for the experiments since at different kinetic energies different regions of the potential energy surface (PES) are probed by the impinging molecules.

The approximate reactivity measure of the d-band model for atomic adsorption Eq. (4.4) does not only depend on the d-band center but also on the coupling matrix element V which is strongly dependent on the distance between the interacting atoms. We have therefore analyzed the change in the adsorption position as a function of the lattice strain. As Table 4.2 demonstrates, at all higher coordinated adsorption sites, the adsorbed hydrogen atom relaxes towards the surface upon lattice expansion. However, this relaxation is done in such a way that the nearest-neighbor hydrogen-copper distance remains basically constant at all considered adsorption site. At the onefold coordinated top site where $h_{\mathrm{Cu-H}}$ and $d_{\mathrm{Cu-H}}$ are the same, there is also practically no change in the bond length between hydrogen and copper. Hence we may assume that the coupling matrix elements V also remain basically unchanged upon lattice expansion.

In order to understand the microscopic origin for the unexpected larger H-Cu attraction on the compressed substrate, we have analyzed the local density of states upon hydrogen adsorption in more detail. Fig. 4.4 shows the change of the local density of states of the Cu d-band at the unstrained (111) surface caused by the hydrogen adsorption on the fcc hollow and the top site, respectively. In addition, the density of states of the hydrogen 1s state is plotted. When the hydrogen atom is adsorbed on the fcc hollow site, the Cu d-band and the H 1s state remain well separated. Furthermore, the Cu d-band is hardly modified by the presence of hydrogen on the surface. Directly above the Cu d-band, the antibonding H 1s-Cu d resonances are visible whose occupation gives rise to the repulsion between the hydrogen atoms and the Cu d bands [155].

For the hydrogen adsorption at the top site, the hydrogen atom is mainly interacting only with one atom directly beneath. In addition, due to symmetry, the hydrogen 1s state only couples to the Cu $d_{3z^2-r^2}$ orbital because all other d orbitals are not rotationally symmetric with respect to the Cu-H bond along the z-axis. Consequently, the H atom at the top site is much more strongly interacting with the single Cu $d_{3z^2-r^2}$ orbital compared to the interaction of the H atom with the Cu d orbitals at the higher coordinated site. This is reflected by the fact that the local d band at the Cu atom

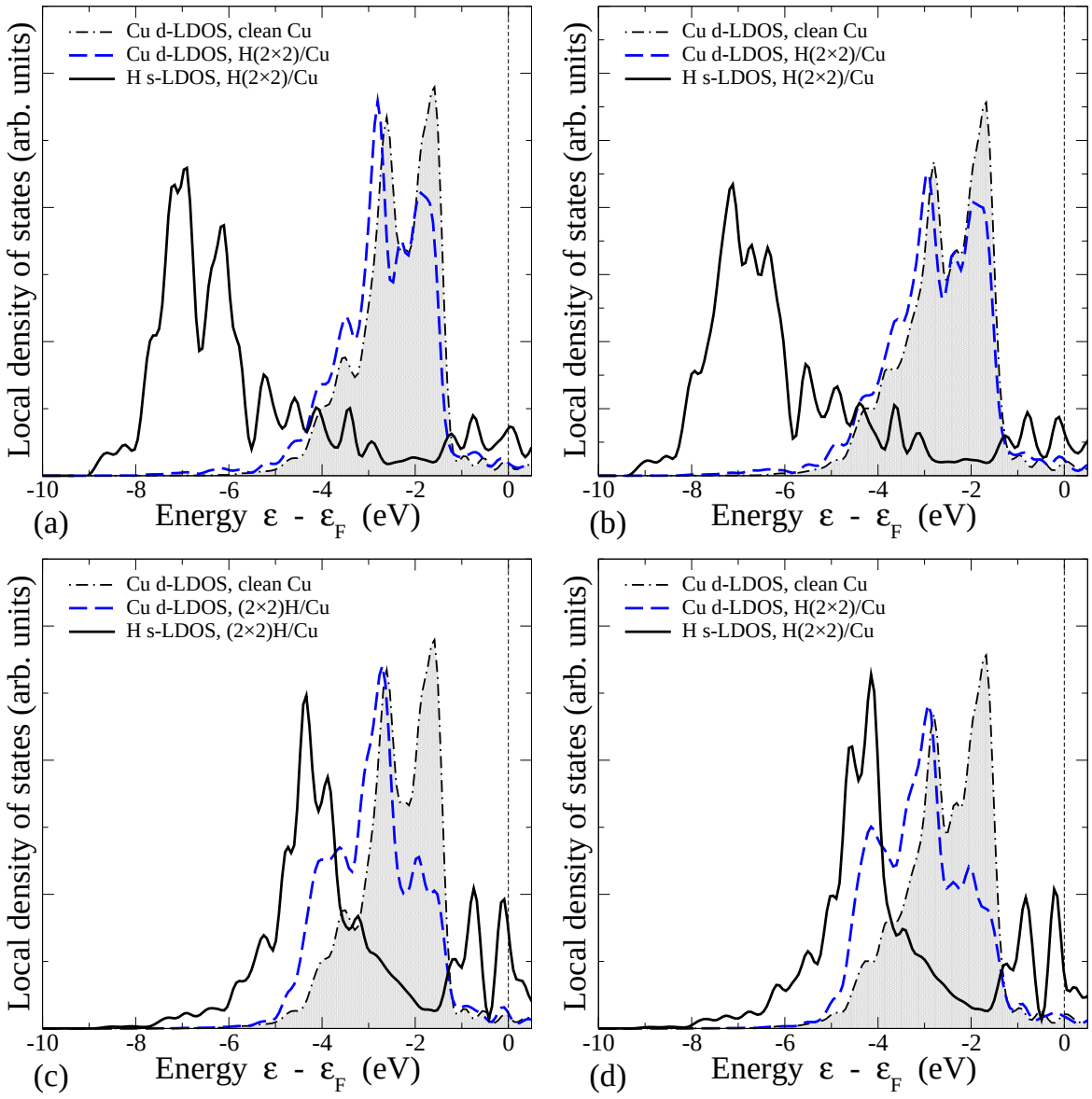

Figure 4.4: Local density of states of the hydrogen 1s state and the Cu d-band for atomic hydrogen adsorption on unstrained Cu(111) at the fcc hollow site (a) and at the top site (c) and on compressed Cu(111) at the fcc site (b) and at the top site (d). The hydrogen 1s density of states is multiplied by a factor of 10.

beneath the hydrogen atom is strongly modified by the presence of the adsorbate, as Fig. 4.4 clearly demonstrates, in spite of the fact that only one d orbital is directly involved in the interaction.

Although on the compressed surface the antibonding H 1s-Cu d resonance becomes more occupied leading to an increased repulsion, the adsorbate-induced downshift of the Cu d-band center is larger by 0.15 eV compared to the unstrained surface. This larger downshift overcompensates the increased occupation of the antibonding states thus stabilizing the adsorption at the top site of the compressed Cu(111) surface.

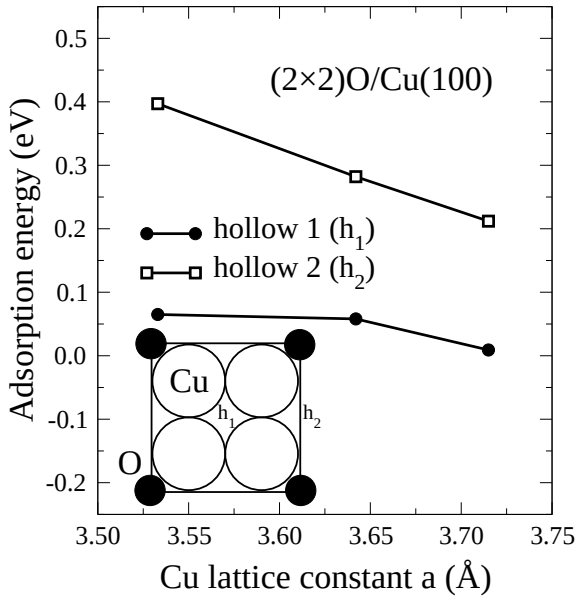

Figure 4.5: Atomic hydrogen adsorption energies as a function of the lattice strain at the hollow sites of the O(2×2)/Cu(100) surface. The adsorption sites are indicated by h_1 and h_2 in the inset.

Consequently, if the hydrogen atom is strongly interacting with a particular copper substrate atom, then apparently the d-band model is no longer fully appropriate. Instead, the response of the local d-band to the presence of the adsorbate has to be taken into account. We find the same phenomenon not only for the one-fold coordinated top sites at Cu(111) and Cu(100), but also for the two-fold coordinated bridge site at the Cu(100) surface. In fact, for the on-top adsorption of *oxygen* on strained copper surfaces the same unexpected trend as a function of lattice strain is found [131]. An analysis reveals that also for O/Cu(111) the on-top adsorption leads to a strong perturbation of the electronic structure stabilizing the adsorption on the compressed surface [156].

Surprisingly, the same trend is also observed for the fourfold hollow site at the Cu(100) surface. However, here the decreasing binding energy upon lattice expansion is caused by another mechanism. For the extended lattice, the hydrogen adsorption position moves closer to the surface plane (see Table 4.2). This means that the interaction of the hydrogen atom with the second layer copper atom will become stronger. In fact, for an adsorption height of $h_{\mathrm{Cu-H}} = 0$ Å, the distance between the hydrogen atom and the surface copper atom would be the same as the distance to the second layer copper atom leading to an effectively fivefold coordinated adsorption site. The second layer copper atom is already twelvefold coordinated which means that it is rather unreactive. Therefore the reduced distance between the hydrogen atom and the second layer copper atom upon lattice expansion leads to an increased repulsion which is responsible for the lower binding energy [157].

For the (2×2) oxygen-precovered Cu(100) surface we have also determined the atomic hydrogen adsorption energies as a function of the lattice strain (see Fig. 4.5).

For a quarter monolayer oxygen on Cu(100) there are two inequivalent fourfold hollow adsorption sites h_1 and h_2. They are indicated in the inset of Fig. 4.5. As already well-known [143], there is a direct repulsion between oxygen and hydrogen adsorbed on copper surfaces, in other words, oxygen poisons the hydrogen adsorption, in particular at site h_2 which is closer to the oxygen atoms than site h_1. Similar results have been found for the hydrogen adsorption on the (2×2) sulfur-precovered Pd(100) surface [158, 159].

In contrast to the clean Cu(100) surface, we obtain a strong decrease of the adsorption energy upon lattice expansion at the oxygen-covered Cu(100) surface. As Fig. 4.2b shows, the d-band center shift is indeed a little bit more pronounced at the oxygen-precovered surface compared to the clean Cu(100) surface, but not stronger than at the clean Cu(111) surface. This suggests that it is not the d-band center shift that is responsible for the change in the adsorption energy, but simply the distance between hydrogen and oxygen which increases with the lattice expansion and thus reduces the mutual repulsion. This view is supported by the fact that the change in the adsorption energy is larger at site h_2 that is closer to the oxygen atoms.

4.3 Hydrogen dissociation barrier on Cu

In addition to the atomic hydrogen adsorption energies we have also determined the hydrogen dissociation barrier on Cu(111), Cu(100) and (2×2)O/Cu(100). At all surfaces, we have kept the center of mass of the hydrogen molecule fixed above the bridge site with the molecular axis parallel to the surface. We have then determined the dissociation path into the adjacent hollow adsorption site by calculating the potential energy surface (PES) as a function of the H-H interatomic distance $d_{\mathrm{H-H}}$ and the center of mass distance from the surface $Z_{\mathrm{Cu-H_2}}$ in this configuration. Thus the studied dissociation paths correspond to the hollow-bridge-hollow (h-b-h) configuration which is well-known [138, 160] to be the most favorable H_2 dissociation path on Cu(111). At Cu(100), in fact it has been found that the minimum dissociation barrier can be further reduced by 30 meV by slightly tilting the molecular axis [160]. On (2×2)O/Cu(100), we expect an even stronger energy gain upon tilting from the h_1-b-h_2 configuration because of the inequivalence of the h_1 and the h_2 site.

However, in order to assess the strain effects for similar configurations we did not

Lattice	Cu(111)				Cu(100)			
strain	E_b	$d_{\mathrm{H-H}}$	$Z_{\mathrm{Cu-H_2}}$	E_{des}	E_b	$d_{\mathrm{H-H}}$	$Z_{\mathrm{Cu-H_2}}$	E_{des}
−3%	0.581	0.974	1.270	0.892	0.534	1.17	1.080	0.844
0%	0.503	0.971	1.230	0.844	0.569	1.22	1.020	0.779
+2%	0.453	0.987	1.190	0.773	0.588	1.23	0.975	0.746

Table 4.3: Dissociation barrier height E_b, H-H distance d and H_2 distance from the surface Z at the dissociation barrier position and desorption barrier E_{des} on Cu(111) and Cu(100) for the hollow-bridge-hollow geometry as a function of the lattice strain.

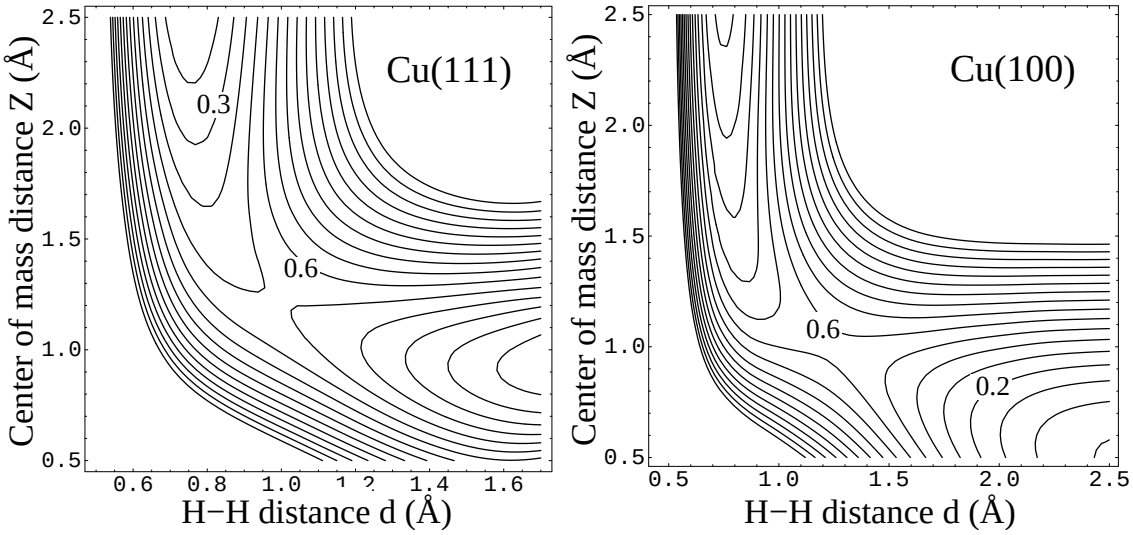

Figure 4.6: Potential energy surface for the hydrogen dissociation on Cu(111) and Cu(100) as a function of the H-H interatomic distance d and the center of mass distance from the surface Z. The energy is in eV/molecule, the energy spacing of the contour lines is 0.1 eV. The dissociation path corresponds to the h-b-h geometry, i.e., the center of mass has been kept fixed laterally above the bridge site with the hydrogen atoms dissociating into the neighboring three- or fourfold hollow sites, respectively. Note the different scale of the d axes.

consider any tilting of the molecular axis in our calculations. The potential energy surfaces of H_2 dissociation in the h-b-h geometry on unstrained Cu(111) and Cu(100) as a function of the H-H distance d_{H-H} and the center of mass distance Z_{Cu-H_2} are shown in Fig. 4.6. It is apparent that the H_2 dissociation barrier on Cu(111) is at a larger distance from the surface, but at a closer separation of the two hydrogen atoms, i.e. it corresponds to an *earlier* barrier [141].

The energetic heights of the H_2 dissociation barriers as a function of the lattice strain are plotted in Fig. 4.7. As far as the unstrained surfaces are concerned, Cu(111) exhibits the lowest dissociation barrier although the Cu(100) surface has a higher d-band center than Cu(111) and should thus be more reactive, i.e., the dissociation barrier should be smaller. This fact has been explained by geometric effects [160]. At Cu(100), the most favorable atomic adsorption positions, the hollow sites, are farther away from the bridge site than for Cu(111) so that the transition state to dissociation occurs at a separation of the two hydrogen atoms that is 0.25 Å larger compared to Cu(111). This is demonstrated in Table 4.3 where the dissociation and desorption barrier heights E_b and E_{des}, respectively, the H-H distance d_{H-H} and the distance from the surface Z_{Cu-H_2} are collected for Cu(111) and Cu(100) as a function of the lattice strain.

As in the case of the atomic adsorption energies, there is no unique trend of the H_2 dissociation barrier on Cu as a function of lattice strain. For H_2/Cu(111), the dissociation barrier decreases for increasing lattice constant. This behavior is in accordance with the predictions of the d-band model in Eq. (4.4). For Cu(100), on the other hand, the dissociation barrier increases upon lattice expansion. Thus Cu(100)

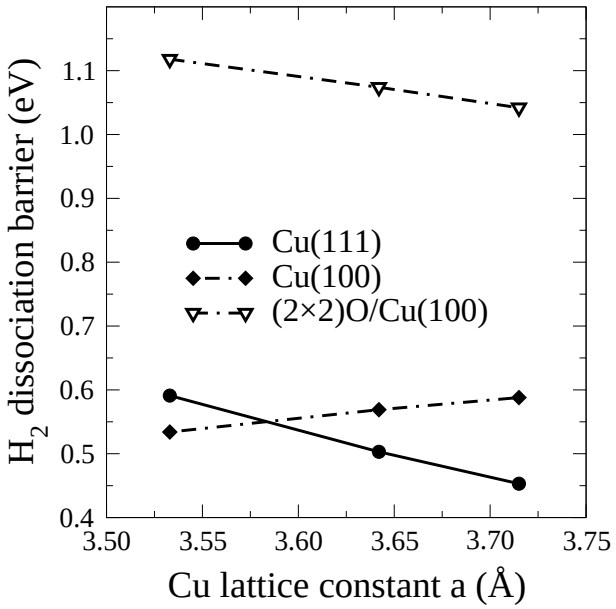

Figure 4.7: The H_2 dissociation barrier in the h-b-h geometry (see text) on Cu(111), Cu(100) and (2×2)O/Cu(100) as a function of the lattice strain.

shows again a trend that is opposite to the predictions of the d-band model. Indeed we connect this dependence of the dissociation barrier with the trend found for the adsorption energies. Since the dissociation barrier is at a larger separation of the two hydrogen atoms, it is strongly influenced by final states effects, i.e., by the atomic adsorption energies [160]. And since atomic adsorption becomes energetically less favorable at the expanded Cu(100) surface, the dissociation barrier also increases upon lattice expansion.

Interestingly enough, on Cu(100) the increase in the dissociation barrier height upon lattice expansion is less pronounced than the increase in the adsorption energies. This can be deduced from the fact that the desorption barrier E_{des} which has been evaluated according to Eq. (2.24) decreases with increasing lattice constant (see Table 4.3). On Cu(111), the desorption barrier also decreases upon lattice expansion but for this surface this mainly stems from the decrease in the dissociation barrier height since the atomic adsorption energies in the Cu(111) hollow sites are almost independent of small lattice strain (see Fig. 4.3a).

In a recent DFT study the H_2 dissociation at kink and vacancy defects of Cu surfaces has been addressed [147]. Similar to our results, the observed trend in the dissociation barriers did not correlate with the position of the center of the local d-band. An analysis of the electronic structure revealed that in fact changes in the Cu sp-states are more important for the modification of the barriers at the defects than changes in the Cu d-states. On the basis of our analysis we cannot exclude that there is also an influence of the Cu sp-states on the trends found in our study. However, we would expect that any influence of the sp-electrons would lead to a unique dependence of adsorption energies and barriers on the substrate strain because of the delocalized

nature of the sp-electrons. Since we do not find such an unique trend we do not believe that the sp electrons are crucial for an understanding of our results.

As far as the oxygen-covered Cu(100) surface is concerned, we also find a decrease in the dissociation barrier height with increasing lateral lattice constant, as Fig. 4.7 shows. However, since this trend is opposite to the one found for the clean Cu(100) surface, this dependence can again be attributed to the increased distance between hydrogen and oxygen upon lattice expansion which reduces the mutual repulsion.

4.4 Reactivity of hydrogen

According to the d-band model, a stronger atomic binding and smaller dissociation barriers are expected on the expanded Cu surfaces. Nevertheless, as reviewed in Secs. 4.2 and 4.3, we find no general trend in the hydrogen-copper interaction energies as a function of lattice strain. Depending on the surface orientation and the adsorption site, hydrogen atomic adsorption energies increase, decrease or remain constant when the lateral lattice constant is varied. In particular at Cu(100), atomic hydrogen adsorption becomes weaker upon lattice expansion. The smaller atomic binding energies of hydrogen on expanded Cu(100) also lead to a dissociation barrier that rises with increasing lattice constant. An analysis of the underlying electronic structure reveals that the d-band model is no longer necessarily appropriate when the local density of states at the substrate atoms is strongly perturbed by the presence of the adsorbate which occurs especially at low-coordinated adsorption sites.

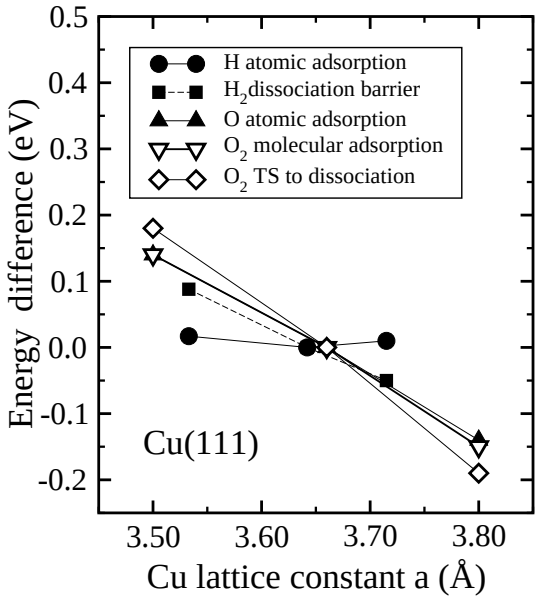

Figure 4.8: Change of the hydrogen adsorption energy and dissociation barrier and the oxygen atomic and molecular adsorption energies as well as the transition state (TS) to dissociation on Cu(111) as a function of the lattice constant. The data for oxygen are taken from Ref. [131].

Recent DFT calculations of atomic hydrogen adsorption on flat and stepped Ru(0001) by Rogadóttir and Nørskov [126] also obtained a very small change in the adsorption energy for different reactive sites. At the low-coordinated step edge sites the corresponding d-band center is higher than for the flat surface. Nevertheless, the hydrogen adsorption energy is only increased by 0.03 eV, while NH_2 is stabilized by more than 1 eV. Apparently the d-band model is not fully applicable for hydrogen adsorption on some metal surfaces.

In Fig. 4.8 we compare the change of the hydrogen adsorption energy and dissociation barrier with the oxygen atomic and molecular adsorption energies as well as the transition state (TS) to dissociation on Cu(111) as a function of the lattice constant. The oxygen data are taken from Ref. [131]. Note that in Ref. [131] a larger lattice strain has been considered.

It is obvious that the atomic hydrogen adsorption energies on Cu(111) do not follow the trend observed for oxygen on Cu(111). However, the change of the H_2 dissociation barrier on Cu(111) caused by substrate strain, although somewhat smaller, is comparable to the change in the oxygen-copper energetics which is in the order of up to 0.2 eV for 5% change in the lattice constant. Thus our calculations confirm that reaction rates on Cu surfaces could be substantially affected by lattice strain.

4.5 Reaction intermediates over stretched surface

The adsorption energies of the reaction intermediates in the partial oxidation of methanol to formaldehyde on a stretched surface have been evaluated on pure Cu(110) for a lateral lattice constant of 3.80 Å in a (2×2) supercell which corresponds to an expansion by 4%. The molecular properties of various adsorbates on the unstrained and the expanded substrate are listed in Table 4.5.

The methanol, methoxy and formaldehyde adsorption energies are all increased by 0.03 eV upon the slab expansion. The adsorption geometry of each molecule is not changed on the strained surface. A significant energy lowering is only found for atomic oxygen adsorption. The overall energy lowering of methanol, methoxy and formaldehyde is in agreement with the d-band model, but only for oxygen the substrate

Adsorbate		E_{ads} (eV)		$h_{\text{Cu-O}}$ (Å)		$d_{\text{Cu-O}}$ (Å)	
/Cu(110)$_{L_x}$	Config	$a_{3.64}$	$a_{3.80}$	$a_{3.64}$	$a_{3.80}$	$a_{3.64}$	$a_{3.80}$
$\frac{1}{2}O_2$	pseudo fcc	−2.46	−2.64	0.63	0.59	1.89	1.88
CH_3OH	O_{sb}-H_{hl}	−0.35	−0.37	1.84	1.84	2.34	2.36
CH_3O	step edge	−2.98	−3.01	1.44	1.31	1.95	1.94
CH_2O	η^1-phase	−0.22	−0.25	1.71	1.66	2.16	2.15
OH	pseudo fcc	−3.49	−3.56	1.43	1.35	1.95	1.95

Table 4.4: Adsorption energies E_{ads} and adsorption height $h_{\text{Cu-O}}$ and distance to the nearest Cu atom $d_{\text{Cu-O}}$ of various adsorbates on unstrained and expanded Cu(110) surface with lattice constants of 3.64 and 3.80 Å respectively.

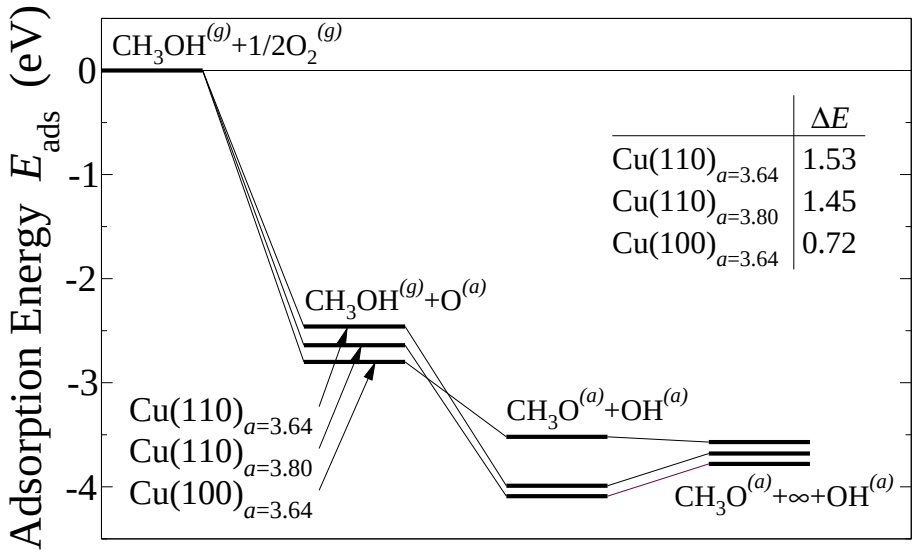

Figure 4.9: Intermediate energies of methanol hydroxyl bond breaking over oxygen covered Cu(100) and Cu(110). ΔE represents the energy difference between CH_3OH+O and CH_3O+OH.

expansion has a sizable effect.

The binding energy of atomic oxygen at the pseudo fcc hollow site is increased by 0.18 eV on the stretched surface. This result is in agreement with the GGA-PW91 calculations by Yu and Mavrikakis [131]. The oxygen binding on strained Cu(111) surface becomes stronger upon lattice expansion in the order of 0.1 eV per 0.1 Å. The Cu(110) surface is more reactive than Cu(111), but the adsorption geometry of the pseudo fcc hollow site is close to Cu(111). The oxygen adsorption geometry is just slightly anisotropic and the substrate atoms are less coordinated. Thus the adsorption energy gain is completely consistent with the result of Yu and Mavrikakis [131].

The hydrogen adsorption energy is almost independent of the slab expansion [161]. The hydrogen conversion to surface hydroxyl on the O-covered surface lowers the total energy by 0.9 eV on the equilibrium Cu(110) surface. We note that the energy gain upon OH formation is larger on the equilibrium surface than on the strained surface, since the increase in the adsorption energy upon lattice expansion for oxygen is much larger than for hydroxyl. Less strongly bound oxygen leads to a stronger O-H bonding.

The energy gain for the reaction intermediates on the (111) facets of the (110) surface does not only depend on the d-band contribution but also on the adsorption geometry. On Cu(100), the atomic oxygen adsorption energy is −2.80 eV where the distance to the nearest Cu atom $d_{\mathrm{Cu-O}}$ is 2.01 Å. The corresponding adsorption energy on Cu(110) is −2.46 eV. Surprisingly it is smaller than on Cu(100). The d-band model predicts a higher reactivity for an open surface, as described in Fig. 4.2b, i.e. $\varepsilon_{\mathrm{d}}^{\mathrm{Cu(100)}} < \varepsilon_{\mathrm{d}}^{\mathrm{Cu(110)}}$ and thus the adsorption energy should be larger on Cu(110). Apparently, the adsorption behavior of oxygen on Cu(110) is very similar to the one on Cu(111) because of the comparable threefold adsorption geometries.

On the expanded (110) surface, the co-adsorption of methanol and atomic oxygen

also leads to the spontaneous OH bond breaking of methanol. In contrast, we find no dissociative adsorption pathway without dissociation barrier on the O/Cu(100) surface. The surface intermediate states in the OH bond breaking are plotted in Fig. 4.9 with respect to gas-phase methanol and oxygen. The attractive interaction between methoxy and hydroxyl on Cu(110) which does not depend on the lattice expansion creates an intermediate state that is distinctly different from the one on Cu(100).

As a result, ΔE is largest on the equilibrium Cu(110) substrate, caused by weakly bound oxygen and the methoxy-hydroxyl attraction. Thus the OH bond breaking is influenced not only by the electronic structure but also by the geometric structure. The reactivity of the oxygen-covered surface, however, is mostly governed by the bonding strength of the adsorbed atomic oxygen. Less tightly bound oxygen is more active for the methanol decomposition.

Thus the binding strength of several adsorbates on the Cu/ZnO catalyst is enhanced on expanded metallic Cu island. At Cu(111), the change of the H_2 dissociation barrier upon lattice expansion was successfully explained within the d-band model. The extension to the methanol decomposition will be discussed in the next chapter.

Chapter 5

Methanol reactions on Cu surfaces

The oxidation of methanol on surfaces has been studied in detail in experiment and theory with the focus on Cu surfaces after the influential study of Wachs and Madix [12]. In this work details of the methanol oxidation were identified by performing temperature programmed desorption (TPD) experiments on oxygen-precovered Cu(110). The reaction pathways determined by Wachs and Madix have proven their validity through numerous successive experiments [81, 82, 84, 93, 111, 120, 122–125, 162–165]. There were several attempts to reproduce the intermediate states and corresponding pathways theoretically [80, 85–88, 92], but these studies only focused on details of the methanol-surface interaction. Hence the determination of reaction pathways including coadsorbed oxygen represents an important contribution.

TDP experiments show that at low temperatures the methanol decomposition path to methoxy is open in the presence of oxygen. It was believed that on clean Cu surfaces the dehydrogenation of methanol is suppressed [12, 166, 167]. In contrast, methanol is converted to methoxy with the help of surface oxygen through a Langmuir-Hinselwood process [168, 169]. Secondary ion mass spectrometry (SIMS) experiments explicitly show the combined increase of methoxy and hydroxyl on oxygen-covered Cu [125]. The methanol dehydrogenation process produces methoxy simultaneously decreasing the amount of surface oxygen [170]. The removal of oxygen occurs via desorption in the form of water,

$$2\mathrm{CH_3OH}^{(g)} + \frac{1}{2}\mathrm{O_2}^{(g)} \longrightarrow 2\mathrm{CH_3O}^{(a)} + \mathrm{H_2O}^{(g)}. \tag{5.1}$$

Recent high resolution XPS experiments by Ammon *et al.* [170] provide a much more detailed microscopic picture of the methanol dehydrogenation process. These spectra show that the hydroxyl bond breaking is activated at 144 K on the clean surface. Furthermore, small amounts of methanol are converted to formaldehyde above 220 K. In fact, this result is in contradiction with early experiments by Sexton *et al.* [111], who only found a physisorbed monolayer of methanol. However, the HRXPS data strongly

suggest the possibility of a low activation barrier for OH bond breaking. Hence it is very important point to understand at the same time the low reactivity of methanol oxidation over the clean surface and the low activation barrier for hydroxyl bond breaking.

Adsorbed methoxy is the most abundant surface intermediate species during the oxidation process. It is decomposed into formaldehyde and atomic hydrogen at 330-400 K under low remaining oxygen coverage [12, 164]. Otherwise, if enough oxygen is available, the channel for formate synthesis is open [171–173]. The CO_2 production channel in Eq. (3.2) follows the later reaction path. This means that it can be suppressed by controlling the oxygen coverage on the surface. In this thesis, the considered reactions will be restricted to the formation of formaldehyde, any further reaction of formaldehyde will not be included.

The methoxy dehydrogenation to formaldehyde has been observed on clean Cu surface. The experimentally determined activation energy of the CH bond breaking on Cu(110) was 0.91-0.92 eV [163]. This experimental activation barrier was determined by heating up the system and measuring the peak temperature of formaldehyde formation. It shows that the CH bond scission on the pure surface requires a large activation energy of the order of 1.0 eV. The methoxy decomposition on the surface can be simplified as

$$2CH_3O^{(a)} \longrightarrow 2CH_2O^{(g)} + {H_2}^{(g)}. \tag{5.2}$$

On the oxygen precovered surface, the methanol oxidation is strongly promoted. STM images of Leibsle *et al.* [120] of the oxygen precovered Cu(110) substrate demonstrate that methoxy forms a stable $c(2 \times 2)$ super structure building a zigzag chainlike structure in [001] direction. The oxygen-covered islands and methoxy-covered islands are well-segregated, and under methanol dosage the methoxy islands are observed to grow at the expense of the oxygen islands. The formaldehyde formation was detected via the disappearance of the $c(2 \times 2)$ methoxy islands along the [001] direction. Silva *et. al.* demonstrated that further oxygen exposure promotes the synthesis of formaldehyde [124].

5.1 Clean surface reaction pathways

The initial steps of the methanol oxidation on clean copper surfaces proceed via OH and CH bond scissions caused by the direct adsorbate-surface interactions as described in Eq. (5.3),

$$CH_3OH^{(g)} \longrightarrow CH_3O^{(a)} + H^{(a)} \longrightarrow CH_2O^{(g)} + 2H^{(a)}. \tag{5.3}$$

It is assumed that the hydrogen atoms remain on the surface in the atomic adsorbate state. Diffusion into the substrate and H_2 desorption into the gas-phase are not taken into account during this decomposition process. The hydrogen desorption barriers in Table 4.3 are 0.84 eV and 0.78 eV on Cu(111) and Cu(100), respectively. On Cu(110), a barrier lower than 0.8 eV is expected, however, still it is considerably large. Hence the assumption of hydrogen remaining on the surface at low temperatures is energetically reasonable. The observed hydrogen desorption above room temperature [12] is also consistent with the DFT calculations.

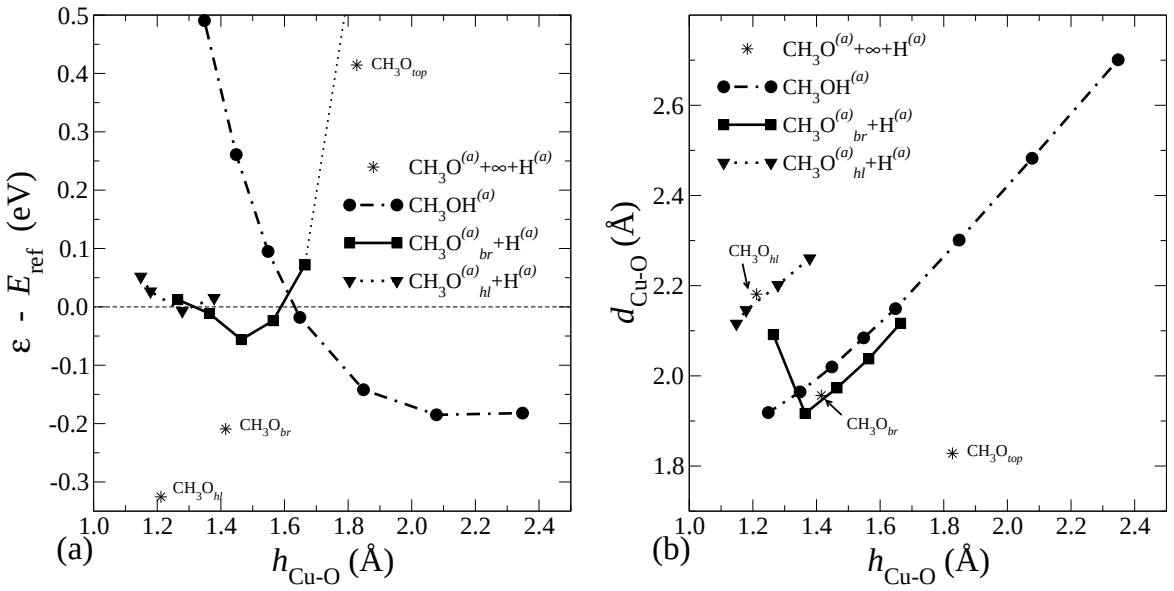

Figure 5.1: Energetics of the methanol interaction with Cu(100) as a function of the methanol height $h_{\mathrm{Cu-O}}$. All degrees of freedoms are fully relaxed except for the O z-coordinate, which corresponds to the methanol height from surface atoms. $d_{\mathrm{Cu-O}}$ represents the distance between oxygen and the nearest Cu atom. Very close to the surface the methanol hydroxyl bond breaks at $h_{\mathrm{Cu-O}} = 1.1$ Å. The adsorption result on the clean surface are plotted as stars.

Within a (2×2) surface unit cell, there is still a remaining repulsive interaction between surface hydrogen and the reaction intermediates. On Cu(100), this repulsive interaction due to the presence of a hydrogen concentration of $\theta_{\mathrm{H}} = 0.25$ is 0.3 eV for methoxy at the hollow site with a coverage $\theta_{\mathrm{CH_3O}} = 0.25$ and 0.57 eV for formaldehyde. As far as the energetics along the reaction pathways reported in the following are concerned, the dissociation barriers of each dehydrogenation steps determined by the NEB method include the hydrogen-adsorbate repulsive interaction, but the energies of the intermediate states are lowered by assuming an infinite separation of the species. The energy difference between reactant and product states is denoted as follows

$$E_{\mathrm{R}\to\mathrm{P}} = E_{\mathrm{product+H}} - E_{\mathrm{reactant}}, \tag{5.4}$$

where $E_{\mathrm{product+H}}$ is the sum of adsorption energies of atomic hydrogen and the product molecule.

5.1.1 Hydroxyl bond breaking

The hydroxyl bond dissociation process on Cu(100) is illustrated in Fig. 5.1 as a function of the methanol adsorption height $h_{\mathrm{Cu-O}}$. The dash-dotted line represents methanol with intact OH bond. The solid and the dotted lines represent methoxy at bridge site and hollow site, respectively, coexisting with atomic hydrogen. The methanol energy increases steeply upon approaching the surface, and very close to the

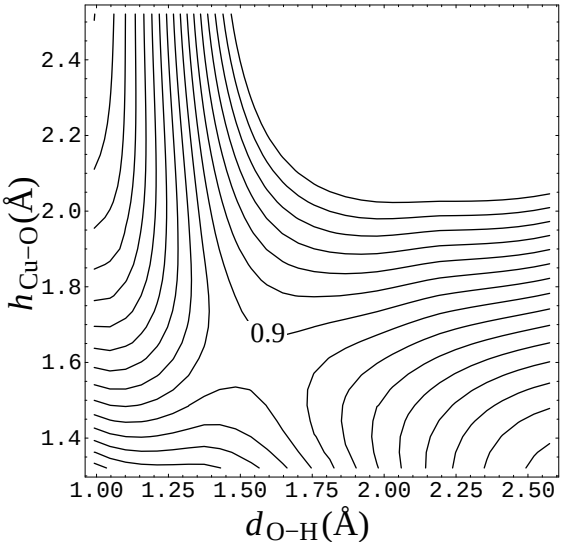

Figure 5.2: Potential energy surface of methanol decomposition over Cu(100). The methanol oxygen atom is confined to the hollow site which is the most favorite configuration for methoxy on the clean surface. The activation barrier is 0.88 eV. Such a large barrier shows that the hollow is not an active site for methanol decomposition.

surface the methanol hydroxyl bond breaks at $h_{\mathrm{Cu-O}} = 1.1$ Å. The methoxy-hydrogen system has two local minimum energy configurations. Methoxy on the bridge is more stable than at the hollow site. And at the bridge site an earlier and lower dissociation barrier is expected than at the hollow site. The activation energy can be estimated to be around 0 eV compared to E_{ref}.

In Fig. 5.1b, the distance from the nearest Cu atom to the methoxy oxygen atom is plotted as a function of the adsorption height. The results for the approach of methanol (dash-dotted line) are close to those for the co-adsorption of methoxy and atomic hydrogen at the bridge site (solid line). It demonstrates that the energetically favorable approach of methanol to the surface is found for the bridge site. In this configuration, the dissociative barrier is determined only by the OH bond stretching.

For methoxy approaching the four fold hollow site, a high dissociation barrier is found in the potential energy surface (PES) illustrated in Fig. 5.2. It shows that the hydroxyl bond breaks 1.6 Å above the surface with a large dissociation barrier of 0.88 eV. An analysis of the methanol-surface interaction suggests that the cost mainly comes from the methanol repulsion from surface. The methanol curve in Fig. 5.1a demonstrates that methanol approaching the bridge site 1.6 Å away from the surface only requires 0.2 eV, whereas at the hollow site there is 0.4 eV higher cost of 0.6 eV.

The exact barrier configuration can be better determined using the nudged elastic band method (NEB). Thus a barrier height of 0.3 eV is obtained on Cu(100). The transition state configuration corresponds to methanol on the bridge site with the OH bond parallel to the surface as predicted by Fig. 5.1. After the dehydrogenation, methoxy diffuses to the energetically preferred high symmetry site.

The transition state over Cu(110) surface is determined by the dimer method [77].

The OH bond becomes broken 1.38 Å above the surface at an O-H separation of 1.50 Å. The barrier height is 0.38 eV with respect to E_{ref}. Apparently the activation barrier is higher than on the Cu(100) surface. The transition state is much closer to the surface than the methoxy adsorption height. As a result, a high electronic density is induced at the methanol. The higher barrier is attributed to the larger repulsion between methanol and the substrate which requires an extra energy cost for the OH bond breaking and leads to the high dissociation barrier.

The influence of the surface hydrogen concentration on the interaction energetics can be estimated by comparing the results of Fig. 5.1 with the adsorption results on the clean surface which are plotted as stars. The methoxy binding energy on the clean surface increases by maximizing the distance to the nearest Cu atoms and the coordination number. With hydrogen present, the bridge site is the most favorable adsorption site, the height of methoxy is 1.46 Å. Hydrogen coadsorption weakens the binding of methoxy and leads to a higher total energy of the system than for the methanol physisorption state, i.e., the dissociation of methanol becomes endothermic within an (2×2) surface unit cell. The detailed properties of methoxy under a high coverage including coadsorbates are discussed in Sec. 3.4.

We can conclude that most of the energetic cost leading to the activation barrier for dissociation is caused by the molecule-surface repulsion rather than the hydroxyl bond stretching. The bridge site becomes the active site for the methanol decomposition due to the lower energetic cost for the approach of methanol.

Interestingly, it has been reported by Chen and Masel [174] that the methanol decomposition to formaldehyde is very active on clean Cu(210). The (210) surface is already rather open with a step-like structure. Because of the low coordination of the atoms directly at the surface, its reactivity should be high according to the d-band model as illustrated in Fig. 4.2b. Hence the hydroxyl bond dissociation barrier on Cu(210) is expected to be smaller than on the Cu(100) surface. On Cu(210), methoxy and hydrogen can be efficiently separated after the breaking of the methanol OH bond. This is the main difference to Cu(111), Cu(100) and Cu(110). Unfortunately, the stabilization mechanism for methoxy and hydrogen on Cu(210) is not known from the experiment. The TPD experiments of Chen and Masel, however, provide an explanation for the high activity of Cu(210) for the methanol decomposition. The first observed product is hydrogen at about 250 K [174]. On Cu(110), it is observed only at 336 K [12]. Since the hydrogen desorption requires only a small activation energy on Cu(210), there is an easy removal of hydrogen atoms from the surface. The intermediate state can be assumed to be methoxy at the pseudo (110) long bridge or pseudo (100) step edge site and hydrogen at the pseudo four fold hollow site. The DFT calculations for Cu(210) show that atomic hydrogen adsorption is endothermic (Fig. 4.3d). Hence H_2 desorption is energetically preferred. Thus H_2 desorption is more likely than the recombinative desorption of H and methoxy as methanol.

Experimentally, clean Cu is considered to be inactive for methanol decomposition to formaldehyde [12]. The only exception is reported for Cu(210) by Chen and Masel [174]. But still the formaldehyde formation from methanol is observed on clean Cu by Ammon *et al.* as illustrated in Fig. 5.3. This means that H_2 desorption does occur on Cu, so that the recombinative desorption of methoxy and hydrogen is blocked. Moreover, the

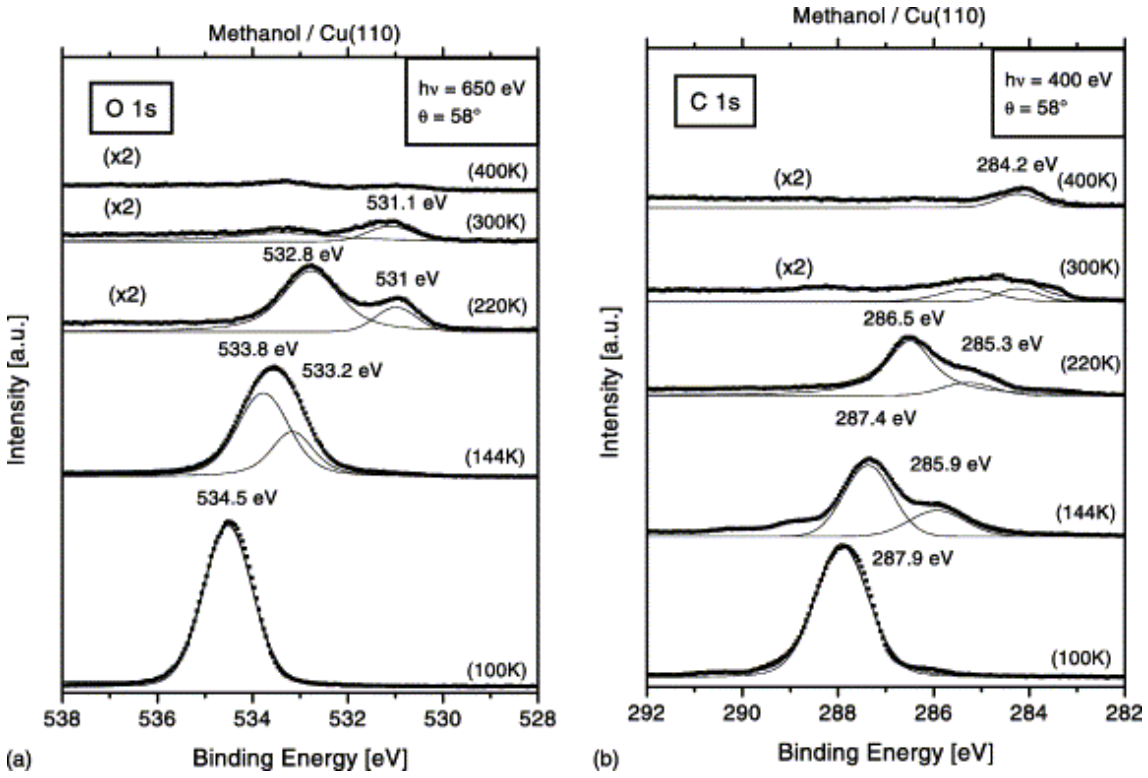

Figure 5.3: HRXP spectra after adsorption of 7.5 L methanol on the pure Cu(110) surface at 100 K (bottom-most spectra) and subsequent annealing to the indicated temperatures. The data were recorded at a sample temperature of 95 K, the emission angle was 58° with respect to the surface normal. (a) O 1s spectra $h\nu = 650$ eV, (b) C 1s spectra $h\nu = 400$ eV (from [170]).

DFT calculations yield a low activation barrier for OH bond breaking. Therefore, we focus on the fact that adsorbed methoxy is strongly influenced by hydrogen present on the surface. The coadsorption of hydrogen and methoxy induces a strong repulsion. After the breaking of the OH bond, the system lowers its total energy by maximizing the distance between hydrogen and methoxy. For more methanol decomposed on the surface, the hydrogen concentration will be increased. At low temperatures, hydrogen will remain on the surface because H_2 desorption is hindered. With methoxy and hydrogen separated far from each other, methoxy can be found on the clean areas of the surface (note the O 1s peak at 533.2 eV in Fig. 5.3). Well-isolated methoxy will be decomposed into formaldehyde and atomic hydrogen at higher temperatures (note the O 1s peak at 531 eV in Fig. 5.3). The amount of formaldehyde production is extremely small, and it is sensitively influenced by the amount of initial methanol exposure. In the next subsection, the CH bond scission on clean surfaces will be discussed in detail.

5.1.2 CH bond breaking

The active configuration for the CH bond breaking process on the clean surface has been assumed to correspond to a bending motion of the methyl group with keeping the Cu-O bond length constant [12, 89]. We have studied various adsorption configurations to find a suitable candidate for this active configuration. In Sec. 3.2, we found a metastable methoxy configuration at the bridge site of Cu(100) and the short bridge site of Cu(110), where the CO bond is tilted by ca. 30° with respect to the surface normal. Similar local minimum configurations have been found on the hydrogen-covered surfaces. The DFT calculations predict the active configuration for the methoxy oxidation to be slightly beside the bridge site. The reaction path determined by the NEB method is in agreement with the expectations mentioned above. Methoxy shifts to the bridge site and the CO bond starts bending. Then the CH bond extension occurs at this tilted configuration. The reaction pathway of the methanol oxidation to the η^2-phase formaldehyde on clean Cu(100) is illustrated in Fig. 5.4.

The barrier height of the second oxidation step is 1.38 eV on Cu(100) and 1.44 eV on Cu(110). GGA-PW91 (DACAPO) calculations of Greeley and Mavirikakis [85] for Cu(111) found a barrier of 1.42 eV. DFT cluster calculation by Gomes *et al.* [86] predicted the barrier to be 1.80 eV for Cu(111). All these results are much larger than the experimental value of 0.92 eV for Cu(110) [163] and 1.06 eV for Cu(111) [82]. There might be several reasons for the discrepancy between theory and experiment. First, we consider the effect of surface oxygen as discussed by Greeley and Mavrikakis. DFT cluster calculations by Gomes *et al.* found a 0.12 eV lower methoxy decomposition barrier caused by the presence of hydroxyl on the surface [86]. However, surface oxygen is hardly active in the methoxy decomposition. According to the experiments, the methoxy dehydrogenation is active at a low coverage of residual oxygen. We found that the methyl group of methoxy interacts repulsively with surface oxygen, in agreement with the experiment. The TPD study of Madix and Telford [163] revealed further details of the surface adsorbates present after the first oxidation step. Residual oxygen has not been detected. In addition, our calculations demonstrate that methoxy prefers to be located at oxygen-free parts of the Cu surface. This suggests that the experimentally measured barrier for methoxy decomposition corresponds to a clean Cu surface configuration.

Secondly, the contribution of strain effects of the Cu substrate and of subsurface oxygen to the methanol oxidation has been discussed for Cu/ZnO catalysts [175–177]. An upshift of the surface d-band center leads to a lowering of the activation energy for ethylene dehydrogenation on various Pd overlayers [178]. The ethylene dissociation barrier decreased by 0.47 eV for a d-band center up-shift of 1 eV. Greeley and Mavrikakis showed that the lattice strain induced d-band center shift lowered the activation energy for O_2 dissociation on Cu(111) by 0.15 eV for 4% expansion. However, the lattice strain of the Cu/ZnO catalyst is below 1% [127]. Thus the contribution of the lattice strain is expected to be below 0.1 eV for the real catalyst Cu/ZnO, and therefore it cannot be considered as a dominant factor. Knop-Gericke *et al.* found that a subsurface oxygen species only present under reaction condition promotes the methanol synthesis. The oxygen species can be introduced through a surface recon-

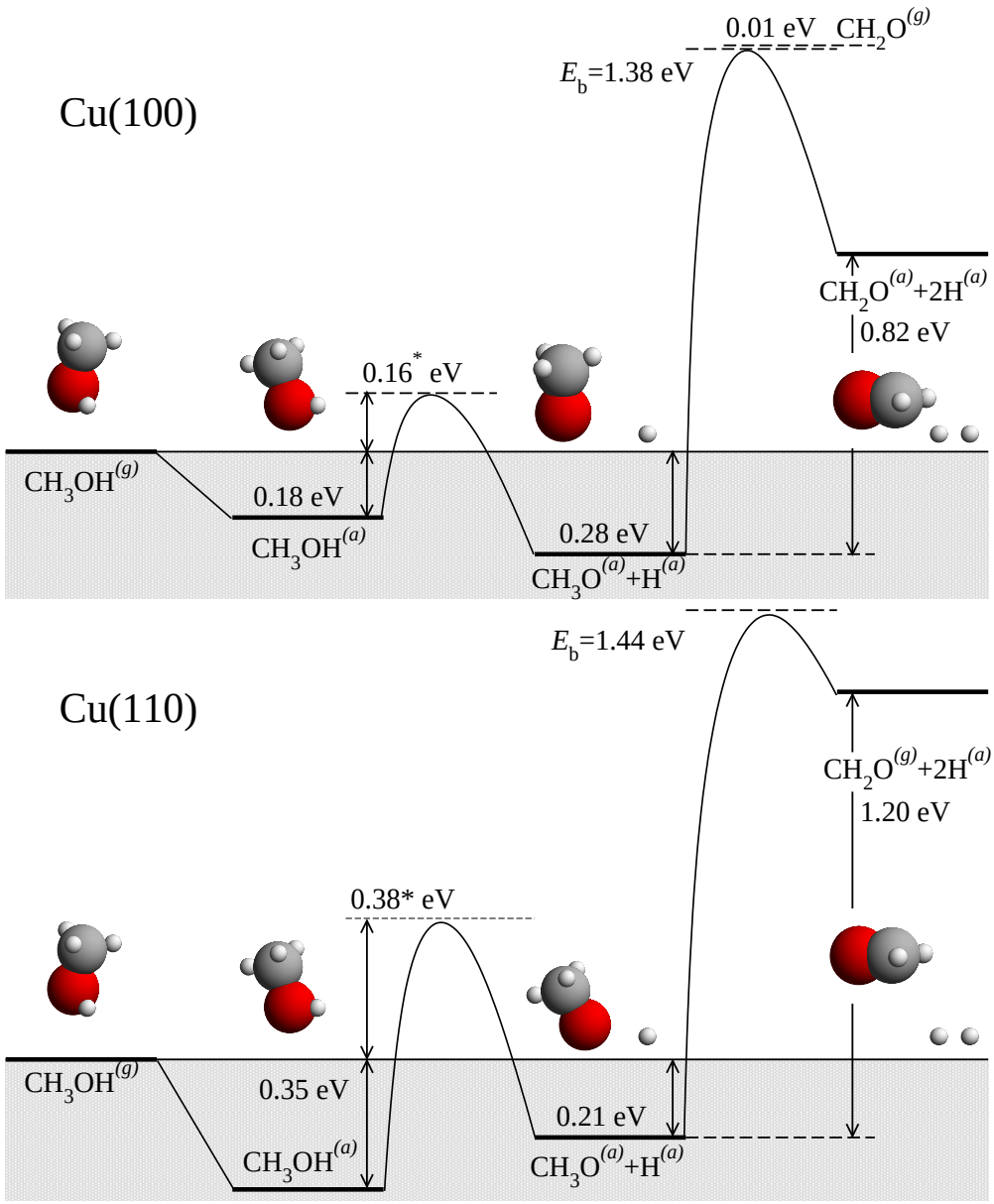

Figure 5.4: Reaction pathways from methanol to η^2-phase formaldehyde on Cu(100) and Cu(110). For the energetics it is assumed that the atomic hydrogen remains on the surface at an infinite separation from the reaction intermediates.

struction by the high coverage of adsorbates. Oxygen-Cu surface clusters might provide an efficient surface geometry for methanol oxidation. However, because of its complexity subsurface oxygen structure have not been included in this work.

Thirdly, surface relaxations during the decomposition process might be important. In the case of Cu, however, the surface distortion upon adsorption is not significant. The calculations show that the methoxy induced surface relaxation lowers the total energy by 70 meV, and chemisorbed formaldehyde (η^2-phase) by 0.1 eV. These two configurations lead to the largest surface distortion. Hence, the energy lowering dur-

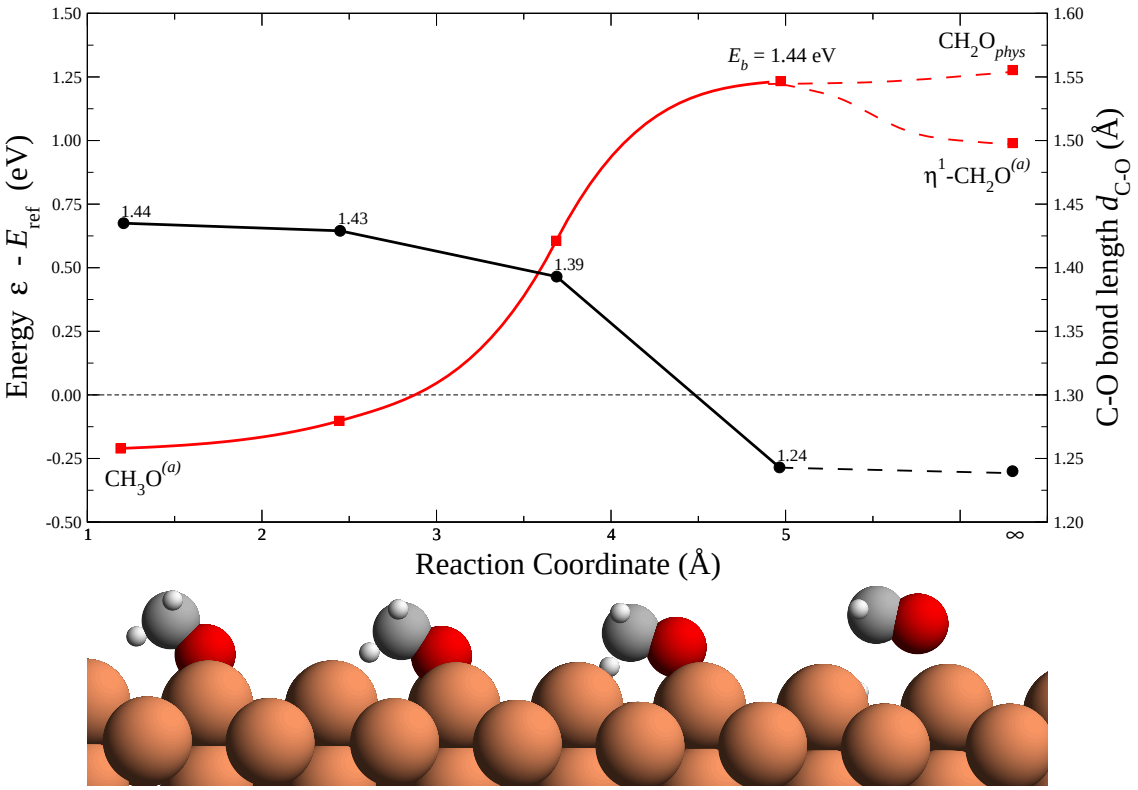

Figure 5.5: Reaction path of the methoxy oxidation on clean Cu(110) surface and its correspoding CO bond length change. The dissociation barrier is estimated to be 1.44 eV. The reaction coordinate denotes the sum of all ionic displacement. The geometric configuration of the NEB images along the reaction path is illustrated in the lower panel.

ing the oxidation process due to relaxations is expected to be below 0.1 eV. Atomic hydrogen induces almost no surface distortion.

In conclusion, we believe that the discrepancy between theory and experiment is mainly due to a failure of the exchange-correlation functional. It is well-known that CH bond scission barriers on metal surfaces are overestimated in GGA-DFT calculations. The CH bond breaking energy of ethylene (C_2H_4) to vinyl (C_2H_3) on Pd(111) was calculated to be 1.5 eV by GGA-PW91 (DACAPO) by Pallassana *et al.* [179], while the experimental value is 0.65-0.75 eV on Pd(100) [180]. In methane (CH_4) decomposition on Ni, the GGA-PW91-derived dissociation barrier is 1.0 eV [160]. However, molecular beam experiments found an activation energy in 0.65 eV on Ni(100) and 0.75 eV on Ni(111) (see Abbott *et al.* [181] and references therein). In contrast to DFT-GGA, *ab initio* quantum chemistry methods obtain barrier height close to the experimental results, 0.67 eV for Ni(100) [182] and 0.7 eV for Ni(111) [183]. Thus, an overestimation of CH bond breaking barriers is obtained using DFT-GGA for several organic molecules over various metal surfaces. Because of this overestimation, the CH dissociation barriers determined by DFT-GGA can only be carefully interpreted in a qualitative fashion.

The NEB calculations show that the barrier for the breaking of the CH bond is

considerably high. On Cu(100), $E_{\mathrm{R}\to\mathrm{P}}$ is larger than the dissociation barrier if physisorbed formaldehyde is chosen as the product state. To avoid this problem, we picked chemisorbed formaldehyde (η^2-phase) as the product state. This leads to a slightly smaller barrier height than on Cu(111). The CH bond breaking barrier on Cu(110) surface is plotted in Fig. 5.5. The dissociation barrier of 1.44 eV is marginally larger than on Cu(100) and on Cu(111). The transition state configuration implies that on Cu(110) an extra repulsive interaction remains between the surface hydrogen and formaldehyde after the CH bond breaking. The CH bond length of 2.28 Å at the transition state is considerably larger than the value of 1.64 Å on Cu(111) [85].

The most abundant surface intermediate found in TPD experiments is methoxy [12]. This is caused by the fact that the methoxy to formaldehyde conversion is hindered by a large activation barrier and that methoxy is very stable on the surface. The surface temperature is not high enough for the conversion to formaldehyde, and methoxy remains on the surface. From the results for the OH bond breaking we concluded that the hydrogen concentration on the surface is strongly correlated with the methoxy stability. On clean surfaces, only a low coverage of methoxy adsorbates can be stabilized. If the methoxy adsorbates survive up to the reaction temperature of methoxy oxidation (300-450 K), formaldehyde formation is induced. Considering the HRXP spectra of Ammon *et al.*, we note that a very weak formaldehyde peak is found on clean Cu(110) in Fig. 5.3. The low rate of formaldehyde formation demonstrates that on clean surfaces methoxy is hard to stabilize. Furthermore, it reflects that the separation of hydrogen and methoxy is not efficient on clean Cu(110).

Finally we conclude that the formation of formaldehyde on pure Cu surfaces is inactive because of the high CH bond dissociation barrier and the instability of the methoxy adsorbate under a high concentration of co-adsorbed hydrogen. Thus the efficiency of the formaldehyde formation depends mainly on the fact whether it is possible to reduce the hydrogen concentration on the surface.

5.2 Oxidation on oxygen covered surface

The methanol oxidation rate is greatly promoted by the presence of oxygen on the surface. Early experiments already mentioned the importance of oxygen [12]. So far, we have obtained a detailed microscopic picture of the reaction on clean surfaces. It suggests that reducing the surface hydrogen concentration leads to a high reactivity for the formaldehyde formation. In this section, we focus on water desorption in the low temperature regime as an efficient channel for hydrogen removal.

The methanol conversion to formaldehyde is maximal on various Cu surfaces for an oxygen coverage of $\theta_{\mathrm{O}} \cong 1/4$ [12, 82, 162]. TPD experiments show that surface oxygen is removed from the surface as water after the first oxidation step. For lower oxygen coverages, the methoxy formation and water desorption are dominant, and for higher coverages methanol dehydrogenation is hindered. The second oxidation step is promoted by the surface itself. If additional oxygen is offered, carbon dioxide formation becomes possible. The reaction of methanol and adsorbed oxygen maintains a 2:1 stoichiometry.

STM images of O/Cu(110) [120, 123, 124] show well-segregated methoxy and oxygen islands. The methoxy structure grows by removing (2×1) oxygen islands in the [001] direction and forms a stable $c(2 \times 2)$ structure. The oxygen islands do not directly support the methoxy oxidation step. The methoxy adsorbate structure remains stable without further oxygen or hydrogen exposure because of the high CH bond dissociation barrier.

5.2.1 Water desorption

The reaction path for the water desorption on O/Cu(110) proceeds through the following steps according to the DFT calculations:

$$CH_3OH^{(g)} + O^{(a)} \longrightarrow CH_3O^{(a)} + OH^{(a)}, \tag{5.5}$$

$$CH_3OH^{(g)} + OH^{(a)} \longrightarrow CH_3O^{c(2\times2)} + H_2O^{(g)}. \tag{5.6}$$

The corresponding reaction pathway is illustrated in Fig. 5.6 including the energies of the intermediate states. Water desorption via the formation of a $c(2 \times 2)CH_3O$ structure is strongly exothermic by 1.08 eV. It shows that water formation is an energetically preferred reaction. Microscopically, the methanol molecules are assumed to sequentially approach the surface oxygen. The first methanol is attracted by the negatively charged surface oxygen via the hydroxyl bond. The hydroxyl bond of the first methanol spontaneously dissociates without any barrier. The second methanol oxidation initiates the water desorption.

However, DFT calculations for methanol on OH/Cu(110) found no spontaneous hydroxyl bond breaking of CH_3OH. Methanol just showed a larger binding energy than on the clean surface. Moreover, water desorption from the second methanol hydroxyl bond breaking is slightly endothermic. The DFT calculations find a relatively strongly bound physisorbed methanol precursor state coexisting with OH. A forced OH bond scission creates a strongly interacting methoxy-water configuration. The water desorption requires 1.03 eV from this methanol-hydroxyl configuration. This pathway requires a large activation energy for the second methanol oxidation (lower path in Fig. 5.6). Thus a detour with forming a $c(2 \times 2)CH_3O$ structure seems to be preferred (upper path in Fig. 5.6).

First, the methoxy-water configuration was tested for a $c(2\times2)CH_3O$ surface structure. This configuration showed almost no attraction. The energy gain because of the attractive interaction of methoxy and water was compensated by the cost of the methoxy structure distortion and the water molecule deformation. Thus the stability of the $c(2\times2)CH_3O$ structure clearly prevents the methanol synthesis induced by water decomposition. The second methanol oxidation step, hence, can be considered to occur through methoxy.

The water desorption leads to the removal of surface hydrogen which makes the recombinative desorption of methanol impossible and thus promotes the further oxidation of methoxy. However, the repulsion between adsorbed methanol and the surface hydroxyl causes a large activation barrier for the water desorption (see the lower panel

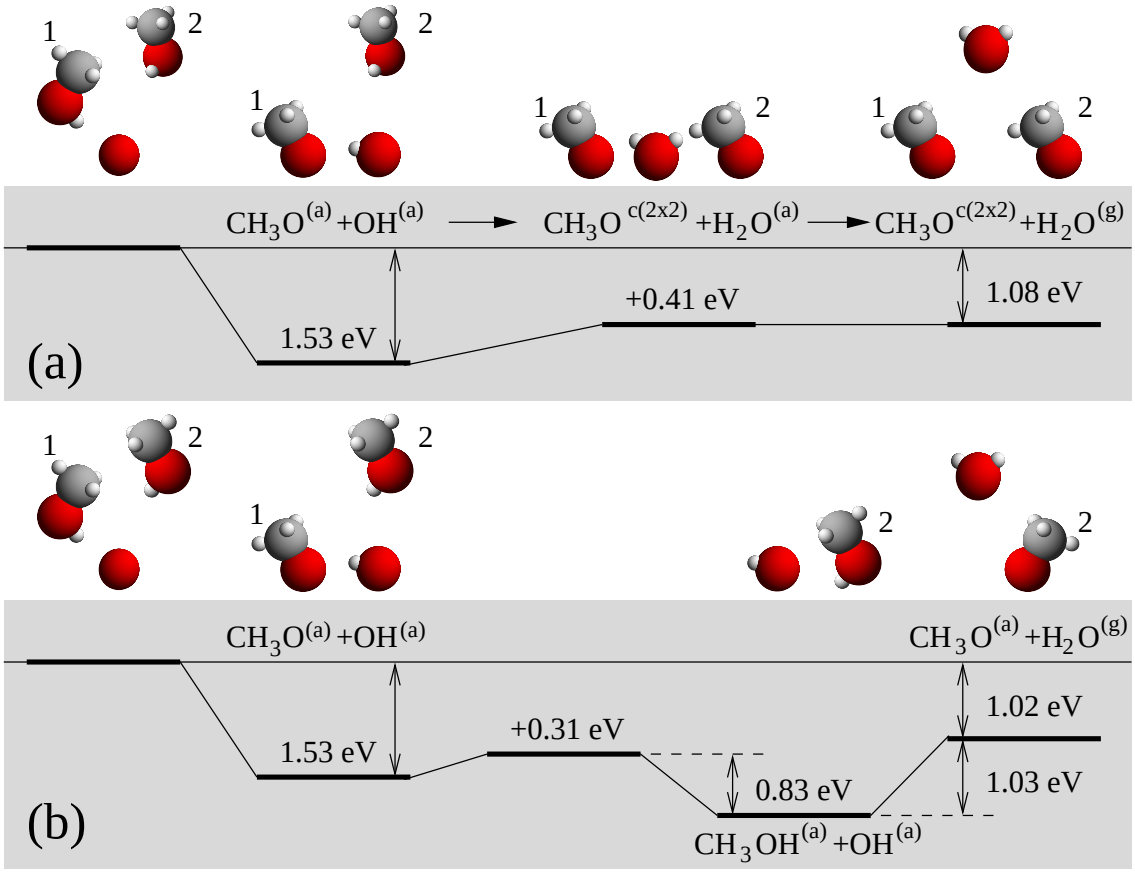

Figure 5.6: Reaction path of water desorption on O/Cu(110). The oxygen coverage corresponds to $\theta_O = 0.25$ and methanol was supplied with $\theta_{CH_3OH} = 0.5$. Thus the stoichiometry is 2:1 for methanol and oxygen. The upper path describes the reaction of the $c(2 \times 2)CH_3O$ structure formation and the desorption of water. In the lower path, a separation between methoxy and hydroxyl after the dissociative adsorption of the first methanol molecule is assumed so that it then corresponds to the reaction of methanol with adsorbed hydroxyl.

of Fig. 5.6). Hence an alternative reaction path should be considered. On the clean surface, the methanol OH bond breaking is hindered by a relatively small barrier. Hence we can assume that methanol dissociates on a clean part of the Cu surfaces and then the hydrogen atoms diffuse to an oxygen atom present some where else on the surface leading to water formation and desorption. This scheme is illustrated in Fig. 5.7. It is exothermic by 0.54 eV on Cu(100) and by 1.02 eV on Cu(110).

Interestingly, it turned out that the larger energy gain on Cu(110) is caused by the less strongly bound surface oxygen which makes it more reactive. The water desorption process illustrated in Fig. 5.7 is summarized in Eqs. (5.7) and (5.8).

$$O^{(a)} + H^{(a)} \longrightarrow OH^{(a)} \tag{5.7}$$

$$OH^{(a)} + H^{(a)} \longrightarrow H_2O^{(g)} \tag{5.8}$$

This shows that the indirect support of surface oxygen also leads to the same water

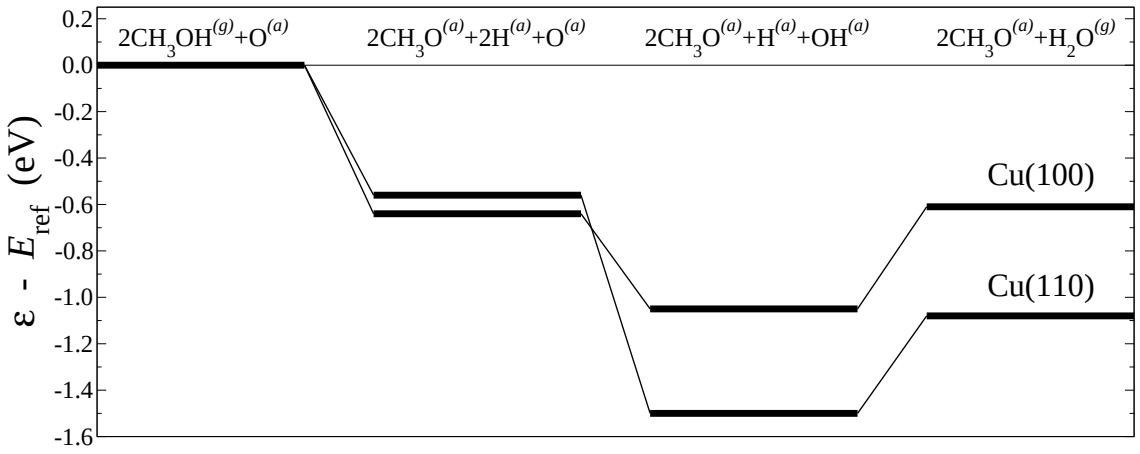

Figure 5.7: Water formation and desorption on O/Cu(110) and O/Cu(100) when the methoxy is formed on a clean part of the Cu surface and the hydrogen atoms then diffuse towards an oxygen atom.

desorption channel as the direct methanol-oxygen interacting scheme. The reverse water gas shift (RWGS: $H_2 + CO_2 \longrightarrow CO + H_2O$) reaction on $Cu/ZnO/Al_2O_3$ catalyst is an important industrial process for the synthesis of methanol and methanol reformation. Several experiments show that the concentration of oxygen on the surface is effectively reduced by hydrogen adatoms [184, 185].

Taking into account the water desorption is necessary for a complete description of the TPD and STM experiments at lower temperatures. Water desorption prevents the recombination of methoxy and hydrogen to methanol, since the water desorption temperature is lower the methoxy-hydrogen recombination temperature [167, 186]. Moreover, these considerations emphasize the important role of the methoxy super structure. The next oxidation step, the CH bond breaking of methoxy, occurs on a clean surface at higher surface temperatures.

The hydrogen diffusion after the methanol OH bond breaking by the clean surface leads to an alternative indirect path for the removal of surface oxygen reduction by water desorption. The presence of the water desorption channel explains why in the experiments the oxygen islands on the surface are reduced gradually under methanol dosage and also for high hydrogen concentrations. Both the indirect and the direct interaction channels for surface oxygen can be summarized as

$$2CH_3OH^{(g)} + O^{(a)} \longrightarrow 2CH_3O^{c(2\times2)} + H_2O^{(g)}. \tag{5.9}$$

Sendner and Groß have simulated the TPD experiments of the methanol decomposition on oxygen-covered Cu(110) using the kinetic Monte Carlo (KMC) method [187, 188]. In this simulation, the activation energies were taken from the DFT calculations presented in this thesis. However, in order to get the correct peak positions, the methanol binding energy had to be increased and the methoxy dehydrogenation barrier had to be reduced, as already discussed in Secs. 3.2 and 5.1.2. Figure 5.8 shows an comparison between the experimental and theoretical TPD spectra. There is a semi-quantitative agreement between the spectra. Still the calculated low-temperature

peaks of water and methanol desorption are too narrow. This is caused by the fact that the lateral interaction between these adsorbates was not included in the simulations. Overall, however, the comparison demonstrates that the methanol oxidation process is qualitatively well-described by the DFT calculations.

5.2.2 CH bond breaking and reaction products

The oxidation of the methoxy in the $c(2 \times 2)$ structure corresponds to methoxy dehydrogenation on a clean Cu surface. The TPD experiments show that the formaldehyde formation peak is at a temperature of 350 K [163]. The species desorbing at higher temperatures are hydrogen, formaldehyde and methanol. These products come from the direct CH bond scission. The temperature of formaldehyde formation is higher than the one for hydrogen desorption, therefore the surface hydrogen formed in the CH bond scission desorbs according to Eq. (5.2). An alternative path is the methoxy-hydrogen recombination according to

$$2\mathrm{CH_3O}^{c(2\times2)} \longrightarrow \mathrm{CH_3OH}^{(g)} + \mathrm{CH_2O}^{(g)} \tag{5.10}$$

Several experiments have been performed addressing the codosing methanol and oxygen on Cu(110) [123, 172, 173, 189]. By controlling the stoichiometry of the reactants the selectivity of the reaction can be changed. According to the reaction schemes (5.2) and (5.10), the reaction products are recombined methanol, molecular hydrogen and formaldehyde. All these products are observed in TPD experiments in the 300-420 K temperature range. Although these reactions require a high energy, they become possible once the surface hydrogen is removed because this makes the direct recombinative methanol desorption impossible.

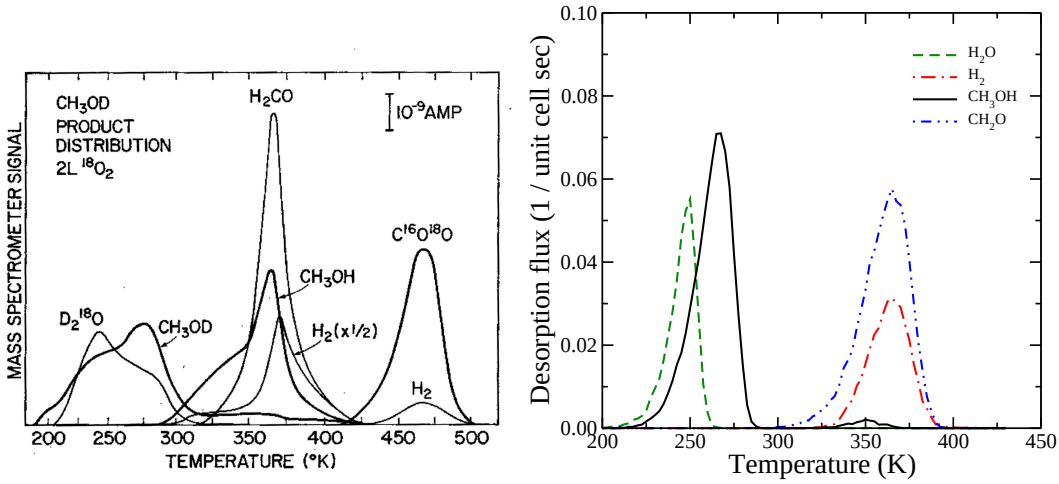

Figure 5.8: Comparison of (a) a measured [12] and (b) a calculated [187, 188] TPD spectrum for the methanol decomposition on oxygen-covered Cu(110). The theoretical TPD spectrum is simulated using the kinetic Monte Carlo method with the activation barriers E_a derived from the DFT calculations presented in this thesis.

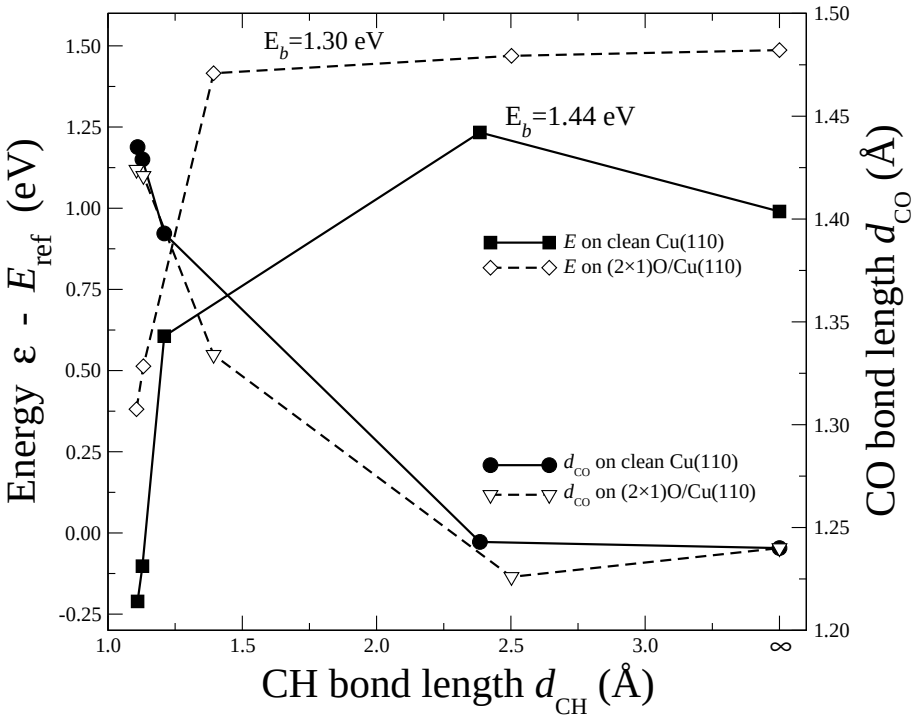

Figure 5.9: Energy and the CO bond length as a function of the CH bond length for the CH bond scission on pure Cu(110) and (2×1)O/Cu(110). The activation energy for the C-H bond breaking is smaller on O/Cu(110) than on the clean surface.

STM experiments have shown that the methoxy superstructure disappears upon continuing oxygen exposure [124]. A shrinkage of the zigzag chains and a reduction of the $c(2 \times 2)$ island in [001] direction were found. This demonstrates that the stability of the methoxy structure is weakened by further oxygen adsorption. Note that the co-adsorption of methoxy and oxygen leads to a repulsive interaction. Thus the further exposed oxygen does not support direct CH bond breaking and does not form hydroxyl.

In Sec. 3.4, it was shown that the $c(2 \times 2)$ structure becomes unstable by oxygen poisoning. Even though surface oxygen induces a strong repulsion within methoxy structure, further oxygen adsorption into the methoxy super structure is still possible. Oxygen poisoning with $\theta_{\mathrm{O}} = 0.25$ ML coverage reduces the stability of the methoxy super structure by 0.71 eV, a $\theta_{\mathrm{O}} = 0.5$ ML coverage even by 1.66 eV.

Formaldehyde formation through the C-H bond breaking of methoxy was studied on a (2×1)O surface. The oxygen induced "added row" reconstruction of the Cu(110) substrate is not considered. The methoxy coverage was $\theta_{\mathrm{CH_3O}} = 0.25$ with the methoxy radicals located between the oxygen rows to reflect the STM experiments which found that the methoxy structure is reduced in the [001] direction by oxygen exposure. The energy difference $E^{2nd}_{\mathrm{R}\rightarrow\mathrm{P}}$ changes to 1.13 eV on the oxygen covered surface from 1.20 eV on the clean surface. Both product and reactant states experiences an overall energetic shift, because both atomic hydrogen and methoxy are repelled from the oxygen on the surface.

The CH dissociation barrier on the oxygen covered surface is 1.30 eV. It is 0.14 eV

lower than on the clean surface. This barrier height lowering by oxygen is similar to the effect of surface hydroxyl [86]. In Fig. 5.9, the reaction pathway of the C-H bond dissociation on clean and (2×1)O covered Cu(110) is shown as a function of the C-H bond length. Methoxy is slightly less strongly bound on the O-covered surface.

The CO bond length change upon the C-H bond stretching shows a similar trend on both surfaces. The same trend was found for the Cu-O distance $d_{\mathrm{Cu-O}}$. On the clean surface, the energy rises rapidly for small CH bond expansion. In this step, the dominant methoxy motion is the CO bond bending. As shown in Fig. 5.5, the energy varies smoothly around the minimum. The energy on the oxygen-covered surface reaches its final value much earlier. This demonstrates that the bending motion of the CO bond is much smoother on the oxygen-covered surface. However, the absolute value is higher, since methoxy is more weakly bound on the oxygen-covered surface.

The presence of oxygen on the surface makes methoxy less stable and thus also leads to a lowering of the barrier height for methoxy oxidation. The fact that methoxy was observed in STM experiments to vanish upon continuing oxygen supply [124] can be explained by this poisoning effect. On oxygen-rich surfaces, the further oxidation of formaldehyde is observed [171–173]. According to our results the η^1-phase of formaldehyde (see table 3.4) should be the most active species. This oxidation proceeds through formaldehyde intermediates and CO_2 desorption. However, these further oxidation steps are not considered in this thesis.

Chapter 6

Conclusions

We have studied the microscopic reaction steps in the partial oxidation of methanol to formaldehyde on various Cu surfaces with and without the presence of oxygen by performing electronic structure calculations based on density functional theory. The energetics of the reaction pathways and of the reaction intermediates have been determined in detail.

As a first step, in Chap. 3 we have determined the energy minimum configurations of methanol, methoxy and formaldehyde. Physisorbed methanol and formaldehyde are weakly bound to Cu surfaces at a large distance from the upper-most Cu layer. In contrast, the methoxy radical interacts strongly with the Cu surface via its oxygen atom. Methoxy prefers to be adsorbed at high-coordination sites on Cu.

Furthermore, we have found a chemisorbed configuration for formaldehyde. This configuration has not been identified in experiment and theory before for Cu surfaces. In this η^2-phase, formaldehyde binds directly to the Cu atoms via both its carbon and oxygen atoms. There is a strong attraction to the surface for this species, but most of the energy gain is compensated by the cost of the deformation of the chemisorbed formaldehyde. As a result, the η^2-phase formaldehyde has a relatively small binding energy of about 0.7 eV. The chemisorbed formaldehyde species is expected to play an important role in the further oxidation of methanol.

Various co-adsorption systems with different coverages have been tested as possible reaction intermediates. Methoxy experiences a large repulsive interaction with co-adsorbed hydrogen or oxygen. It forms a dense layer on Cu, excluding other adsorbed species. The most stable methoxy structure is $c(2 \times 2)CH_3O/Cu(110)$ with methoxy located at the pseudo (111) step edge sites.

Possible strain effects in real catalysts are addressed by slab calculations with different lateral lattice constants. In Chap. 4, the reactivity of Cu substrates are analyzed in terms of the d-band model. Hydrogen adsorption has been considered in detail as a benchmark system. The calculations show that the reactivity of Cu can be described by the d-band model, but at some sites no clear trend of the adsorption energy as

a function of the lattice strain has been found. Additional calculations for reaction intermediates clearly show an enhanced reactivity of the stretched surface. However, the gain in adsorption energy for methanol, methoxy and formaldehyde is modest. A considerable change was only found for oxygen. The activity of real catalyst seems to be dominantly controlled by the oxygen exposure.

In Chap. 5, the reaction pathways are determined in terms of intermediate state energies and activation barriers. Methanol oxidation on clean Cu surfaces is believed to be inactive. However, recent HRXPS experiment by Ammon *et al.* revealed that a considerable amount of methanol is decomposed on clean Cu(110), while the formaldehyde formation rate is extremely low. More interestingly, on clean Cu(210) formaldehyde synthesis is very active. Various calculations for the O-H bond breaking of methanol show that the activation barrier is rather small, e.g. only 0.15 eV on Cu(100). The further reaction to formaldehyde is hindered by a large CH bond breaking barrier. The calculations show that methoxy will be preferentially recombine with surface hydrogen, since the hydroxyl bond reconstruction is only hindered by a small barrier. On the other hand, the high H_2 desorption and CH bond breaking barriers prevent the methoxy decomposition. The low reactivity of pure Cu for methanol oxidation is caused by these two barriers.

The high activity for formaldehyde formation on oxygen-covered Cu surfaces can be explained by the efficient removal of surface hydrogen in the form of water. The RWGS process reduces the surface hydrogen concentration. On clean Cu, methoxy is very stable over a long time. The decay to formaldehyde occurs at higher temperatures without the direct influence of surface oxygen. Hence, oxygen is an efficient agent for methanol oxidation mainly by removing surface hydrogen.

For the second oxidation step, oxygen does not promote the CH bond breaking directly. The methyl group and surface oxygen interact repulsively and the TPD spectra show no water desorption between 330 and 400 K. Thus we know that there is no direct promotion of the second oxidation step by oxygen. However, recent STM experiment show that continuing oxygen exposure leads to the removal of adsorbed methoxy from the surface. The oxygen exposure makes the methoxy adsorbates unstable. It facilitates the methoxy bending motion and causes a lower activation barrier for the C-H bond breaking. Further oxygen exposure also induces a strong binding of the η^1-phase formaldehyde which is an intermediate state for the CO_2 formation.

In the DFT calculations the CH bond breaking barrier is overestimated by 0.5 eV compared to the experiment. Although a direct comparion between experiment and theory is not easy, still there remains a considerable mismatch between experiment and theory. It turns out that GGA overestimates the energy barrier for CH bond breaking for several systems. Therefore, the calculated barrier height can only be very carefully interpreted in a qualitative fashion.

In conclusion, the catalytic activity of Cu-based catalysts for methanol oxidation depends crucially on the fact how easily hydrogen atoms can be removed from the surface. On clean and oxygen-covered Cu surfaces hydrogen desorption is hindered by larger activation barrier than the methanol recombinative desorption. Tensile strain of the substrate lowers the desorption barrier but hydrogen adsorption energies are hardly affected. The presence of oxygen on the surface leads to hydrogen removal via water

desorption. The activity of oxygen-covered Cu surfaces depends on the metal-oxygen interaction strength with more weakly bound oxygen being more reactive. In addition, the surface geometry plays an important role. Stepped surfaces often show a higher catalytic activity. Finally, the selectivity for CO and CO_2 formation can be controlled by oxygen exposure.

Bibliography

[1] F. Besenbacher, I. Chorkendorff, B. S. Clausen, B. Hammer, A. M. Molenbroek, J. K. Nørskov, and I. Stensgaard. Design of a surface alloy catalyst for steam reforming. *Science*, 279:1913–1915, 1998.

[2] Axel Groß. *Theoretical surface science : A microscopic perspective*. Springer-Verlag, 2003.

[3] Axel Groß. The virtual chemistry lab for reactions at surfaces: Is it possible? Will it be useful? *Surf. Sci.*, 500:347–367, 2002.

[4] A. Groß. Dynamics of molecule-surface interactions from first principles. In D. P. Woodruff, editor, *The Chemical Physics of Solid Surfaces*, volume 11, chapter 1. Elsevier, Amsterdam, 2003.

[5] World Methanol Supply/Demend, 2000. DeWitt & Company, Inc.

[6] B. Peppley, J. Amphlett, L. Kearns, and R. Mann. Methanol-steam reforming on $Cu/ZnO/Al_2O_3$ catalysts. Part 2. A comprehensive kinetic model. *Appl. Catal. A*, 179:31–49, 1999.

[7] G. C. Chinchen, K. C. Waugh, and D. A. Whan. The activity and state of the copper surface in methanol synthesis catalysts. *Appl. Catal.*, 25:101, 1986.

[8] G. C. Chinchen, C. M. Hay, H. D. Vandervell, and K. C. Waugh. The measurement of copper surface-areas by reactive frontal chromatography. *J. Catal.*, 103: 79, 1987.

[9] C. T. Campbell, K. A. Daube, and J. M. White. $Cu/ZnO(000\bar{1})$ and $ZnO_x/Cu(111)$: Model catalysts for methanol synthesis. *Surf. Sci.*, 182:458–476, 1987.

[10] N. Jedrecy, S. Gallini, M. Sauvage-Simkin, and R. Pinchaux. Copper growth on the O-terminated $ZnO(000\bar{1})$ surface: Structure and morphology. *Phys. Rev. B*, 64:085424, 2001.

[11] L. V. Koplitz, O. Dulub, and U. Diebold. STM study of copper growth on $ZnO(0001)$–Zn and $ZnO(000\bar{1})$–O surfaces. *J. Phys. Chem. B*, 107:10583–10590, 2003.

[12] I. E. Wachs and R. J. Madix. The selective oxidation of CH_3OH to CH_2O on a Copper(110) catalyst. *J. Catal.*, 53:208, 1978.

[13] M. Born and J. R. Oppenheimer. Über die Theorie der Molekeln. *Ann. Phys.*, 84:457, 1927.

[14] J. H. Ziman. *Electrons and Phonons*. Oxford University Press, Oxford, 1960.

[15] P. Hohenberg and W. Kohn. Inhomogeneous electron gas. *Phys. Rev.*, 136:B864, 1964.

[16] L. H. Thomas. The calculation of atomic fields. *Proc. Cambridge Philos. Soc.*, 23:542–548, 1927.

[17] E. Fermi. A statistical method for the determination of some atomic properties and the application of this method to the theory of the periodic system of elements. *Z. Phys.*, 48:73–79, 1928.

[18] E. H. Lieb. Thomas-Fermi and related theories of atoms and molecules. *Rev. Mod. Phys.*, 53:603–641, 1981.

[19] W. Kohn and L. J. Sham. Self-consistent equations including exchange and correlation effects. *Phys. Rev.*, 140:A1133, 1965.

[20] J. W. Rayleigh. In finding the correction for the open end of an organ-pipe. *Phil. Trans.*, 161:77, 1870.

[21] W. Ritz. Über eine neue Methode zur Lösung gewisser Variationsprobleme der mathematischen Physik. *J. reine angew. Math.*, 135:1–61, 1908.

[22] G. B. Arfken and H. J. Weber. *Mathematical Methods for Physicists*. Academic Press, San Diego, 4th edition, 1995.

[23] M. C. Payne, M. P. Teter, D. C. Allan, T. A. Arias, and J. D. Joannopoulos. Iterative minimization techniques for *ab initio* total-energy calcualtions: molecular dynamics and conjugate gradients. *Rev. Mod. Phys.*, 64:1045, 1992.

[24] D. D. Johnson. Modified Broyden's method for accelerating convergence in self-consistent calculations. *Phys. Rev. B*, 38:12807, 1988.

[25] J. F. Janak. Proof that $\partial E/\partial n_i = \varepsilon$ in density-functional theory. *Phys. Rev. B*, 18:7165, 1978.

[26] D. M. Ceperley and B. J. Alder. Ground state of the electron gas by a stochastic method. *Phys. Rev. Lett.*, 45:566, 1980.

[27] John P. Perdew. Accurate density functional for the energy: Real-space cutoff of the gradient expansion for the exchange hole. *Phys. Rev. Lett.*, 55:1665, 1985.

[28] W. Kohn. Nobel lecture: Electronic structure of matter—wave functions and density functionals. *Rev. Mod. Phys.*, 71:1253–1266, 1999.

[29] A. D. Becke. Density-functional exchange-energy approximation with correct asymptotic behavior. *Phys. Rev. A*, 38:3098, 1988.

[30] C. Lee, W. Yang, and R. Parr. Development of the Colle-Salvetti correlation-energy formula into a functional of the electron density. *Phys. Rev. B*, 37:785, 1988.

[31] John P. Perdew, J. A. Chevary, S. H. Vosko, Koblar A. Jackson, Mark R. Pederson, D. J. Singh, and Carlos Fiolhais. Atoms, molecules, solids, and surfaces: Applications of the generalized gradient approximation for exchange and correlation. *Phys. Rev. B*, 46:6671, 1992.

[32] J. P. Perdew, K. Burke, and M. Ernzerhof. Generalized gradient approximation made simple. *Phys. Rev. Lett.*, 77:3865, 1996.

[33] B. Hammer, L. B. Hansen, and J. K. Nørskov. Improved adsorption energetics within density-functional theory using revised Perdew-Burke-Ernzerhof functionals. *Phys. Rev. B*, 59:7413, 1999.

[34] Neil W. Ashcroft and N. David Mermin. *Solid State Physics*. Saunders College Publishing, 1976.

[35] H. J. Monkhorst and J. D. Pack. Special points for Brillouin-zone integrations. *Phys. Rev. B*, 13:5188, 1976.

[36] M. Methfessel and A. T. Paxton. High-precision sampling for Brillouin-zone integration. *Phys. Rev. B*, 40:3616, 1989.

[37] P. E. Blöchl, O. Jepsen, and O. K. Andersen. Improved tetrahedron method for Brillouin-zone integration. *Phys. Rev. B*, 49:16223, 1994.

[38] P. Pulay. Convergence acceleration of iterative sequences. The case of SCF iteration. *Chem. Phys. Lett.*, 73:393, 1980.

[39] G. Kresse and J. Hafner. Ab initio molecular dynamics for liquid metals. *Phys. Rev. B*, 47:558, 1993.

[40] G. Kresse and J. Hafner. Norm-conserving and ultrasoft pseudopotentials for the first-row and transition elements. *J. Phys.: Condens. Matter*, 6:8245, 1994.

[41] G. Kresse and J. Furthmüller. Efficient iterative schemes for ab initio total-energy calculations using a plane-wave basis set. *Phys. Rev. B*, 54:11169, 1996.

[42] G. Kresse and J. Furthmüller. Efficiency of ab-initio total energy calculations for metals and semiconductors using a plane-wave basis set. *Comput. Mater. Sci.*, 6:15–50, 1996.

[43] P. Teter, M. C. Payne, and D. C. Allan. Solution of Schrödinger's equation for large systems. *Phys. Rev. B*, 40:12255, 1989.

[44] D. M. Bylander, L. Kleinman, and Seongbok Lee. Self-consistent calculations of the energy bands and bonding properties of B_12C_3. *Phys. Rev. B*, 42:1394, 1990.

[45] A. Wood, D. M. Zunger. A new method for diagonalising large metrices. *J. Phys. A: Math, Gen.*, 18:1343–1359, 1985.

[46] R. P. Feynman. Forces in molecules. *Phys. Rev.*, 56:340, 1939.

[47] J. C. Slater. Wave functions in a periodic potential. *Phys. Rev.*, 51:846, 1947.

[48] O. K. Adersen. Liner methods in band theory. *Phys. Rev. B*, 12:3060, 1975.

[49] B. Kohler, S. Wilke, M. Scheffler, R. Kouba, and C. Ambrosch-Draxl. Force calculation and atomic-structure optimization for the full-potential linearized augmented plane-wave code WIEN. *Comput. Phys. Commun.*, 94:31–48, 1996.

[50] U. von Barth and C. D. Gelatt. Validity of the frozen-core approximation and pseudopotential theory for cohesive energy calculations. *Phys. Rev. B*, 21:2222, 1980.

[51] N. Troullier and J. L. Martins. Efficient pseudopotentials for plane-wave calculations. *Phys. Rev. B*, 43:1993, 1991.

[52] A. M. Rappe, K. M. Rabe, E. Kaxiras, and J. D. Joannopoulos. Optimized pseudopotentials. *Phys. Rev. B*, 41:1227, 1990.

[53] David Vanderbilt. Soft self-consistent pseudopotentials in a generalized eigenvalue formalism. *Phys. Rev. B*, 41:7892, 1990.

[54] P. E. Blöchl. Projector augmented-wave method. *Phys. Rev. B*, 50:17953, 1994.

[55] G. Kresse and D. Joubert. From ultrasoft pseudopotentials to the projector augmented-wave method. *Phys. Rev. B*, 59:1758, 1999.

[56] F. D. Murnaghan. The compressibility of media under extreme pressure. *Proc. Natl. Acad. Sci. USA*, 30:244–247, 1944.

[57] F. Birch. Finite strain isotherm and velocities for single-crystal and polycrystalline NaCl at high pressures and 300 K. *J. Geophys. Res.*, 83:1257, 1978.

[58] R. Smoluchowski. Anisotropy of the electronic work function of metals. *Phys. Rev.*, 60:661–674, 1941.

[59] Matthias Scheffler and Catherine Stampfl. Theory of adsorption on metal substrates. In K. Horn and M. Scheffler, editors, *Handbook of surface science*, volume 2. Elsevier, Amsterdam, 1999.

[60] Roald Hoffmann. A chemical and theoretical way to look at bonding on surfaces. *Rev. Mod. Phys.*, 60:601, 1988.

[61] B. Hammer and M. Scheffler. Local chemical reactivity of a metal alloy surface. *Phys. Rev. Lett.*, 74:3487, 1995.

[62] R. O. Jones and O. Gunnarsson. The density functional formalism, its applications and prospects. *Rev. Mod. Phys.*, 61:689, 1989.

[63] A. D. Becke and K. E. Edgecombe. A simple measure of electron localization in atomic and molecular systems. *J. Chem. Phys.*, 92:5397–5403, 1990.

[64] M. J. Gillan. Quantum simulation of hydrogen in metals. *Phys. Rev. Lett.*, 58: 563, 1987.

[65] M. J. Gillan. Quantum-classical crossover of the transition rate in the damped double well. *J. Phys. C*, 20:3621–3641, 1987.

[66] Gregory A. Voth, David Chandler, and William H. Miller. Rigorous formulation of quantum transition state theory and its dynamical corrections. *J. Chem. Phys.*, 91:7749–7760, 1989.

[67] G. A. Voth. Feynman path integral formulation of quantum mechanical transition-state theory. *J. Phys. Chem.*, 97:8365–8377, 1993.

[68] Michael Messina, Gregory K. Schenter, and Bruce C. Garrett. Centroid-density quantum rate theory: Variational optimization of the dividing surface. *J. Chem. Phys.*, 98:8525–8536, 1993.

[69] Michael Messina, Gregory K. Schenter, and Bruce C. Garrett. Quantum activated rate theory: Variational optimization of planar dividing surfaces. *J. Chem. Phys.*, 99:8644–8653, 1993.

[70] G. Mills, H. Jónsson, and G.K. Schenter. Reversible work transition state theory: application to dissocative adsorption of hydrogen. *Surf. Sci.*, 324:305–337, 1995.

[71] G. Schenter, G. Mills, and H. Jónsson. Reversible work based quantum transition

state theory. *J. Chem. Phys.*, 101:8964, 1994.

[72] Bruce C. Garrett and Donald G. Truhlar. Generalized transition state theory. Classical mechanical theory and applications to collinear reactions of hydrogen molecules. *J. Phys. Chem.*, 83:1052–1079, 1979.

[73] R. P. Feynman and A. R. Hibbs. *Quantum Mechanics and Path Integrals*. McGraw-Hill, New York, 1965.

[74] Greg Mills and Hannes Jónsson. Quantum and thermal effects in H_2 dissociative adsorption: Evaluation of free energy barriers in multidimensional quantum systems. *Phys. Rev. Lett.*, 72:1124, 1997.

[75] G. Henkelman and H. Jónsson. Improved tangent estimate in the nudged elastic band method for finding minimum energy paths and saddle points. *J. Chem. Phys.*, 113:9978, 2000.

[76] G. Henkelman, B. P. Uberuaga, and H. Jónsson. A climbing image nudged elastic band method for finding saddle points and minimum energy paths. *J. Chem. Phys.*, 113:9901, 2000.

[77] G. Henkelman and H. Jónsson. A dimer method for finding saddle points on high dimensional potential surfaces using only first derivatives. *J. Chem. Phys.*, 111: 7010, 1999.

[78] William L. Jørgensen and Lionel Salem. *The Organic Chemist's Book of Orbitals*. Academic Press, New York, 1973.

[79] C. F. Jackels. A potential-energy surface study of the $^2A_1$ and low-lying dissociative states of the methoxy radical. *J. Chem. Phys.*, 82:311, 1985.

[80] D. Zeroka and R. Hoffmann. Adsorption of methoxy on Cu(100). *Langmuir*, 2: 553, 1986.

[81] M. Bowker and R. J. Madix. XPS, UPS and Thermal desorption studies of alchol adsorption on Cu(110), I Methanol. *Surf. Sci.*, 95:190–206, 1980.

[82] J. N. Russell Jr., S. M. Gates, and J. T. Yates Jr. Reaction of methanol with Cu(111) and Cu(111) + O(ads). *Surf. Sci.*, 163:516–540, 1985.

[83] B. A. Sexton and A. E. Hughes. A comparison of weak molecular adsorption of organic molecules on clean copper and platinum surfaces. *Surf. Sci.*, 140:227, 1984.

[84] D. B. Clarke, D. Lee, M. J. Sandoval, and A. T. Bell. Infrared studies of the mechanism of methanol decomposition on Cu/SiO_2. *J. Catal.*, 150:81–93, 1994.

[85] J. Greeley and M. Mavrikakis. Methanol Decomposition on Cu(111): A DFT Study. *J. Catal.*, 208:291–300, 2002.

[86] J. R. B. Gomes, J. A. N. F. Gomes, and F. Illas. Methoxy radical reaction to formaldehyde on clean and hydroxy radical-covered copper(111) surfaces: a density functional theory study. *Surf. Sci.*, 443:165–176, 1999.

[87] J. R. B. Gomes and J. A. N. F. Gomes. A DFT study of the methanol oxidation catalyzed by a copper surface. *Surf. Sci.*, 471:59–70, 2001.

[88] J. Greeley and M. Mavrikakis. A first-principles study of methanol decomposition on Pt(111). *J. Am. Chem. Soc.*, 124:7193–7201, 2002.

[89] R. Ryberg. Symmetry and orientation of CH_3O on Cu(100). *Phys. Rev. B*, 31: 2545, 1985.

[90] R. Ryberg. The oxidation of methanol on Cu(100). *J. Chem. Phys.*, 82:567–573, 1985.

[91] D. E. Ricken, A. W. Somers, J. Robinson, and A. M. Bradshaw. Structure of the surface methoxy species on Cu(111). *Faraday Disc. Chem. Soc.*, 89:291, 1990.

[92] J. A. Rodriguez. The bonding of acetate, methoxy, thiomethoxy and pyridne to Cu surfaces: a molecular orbital study. *Surf. Sci.*, 273:385–404, 1992.

[93] R. Ryberg. Oxidation of methanol on Cu(100) studied by infrared spectroscopy. *Phys. Rev. Lett.*, 49:1579, 1982.

[94] K. Amemiya and Y. Kitajima. Oxygen K-edge x-ray-absorption fine-structure study of surface methoxy species on Cu(111) and Ni(111). *Phys. Rev. B*, 59:2307, 1999.

[95] M. Bader, A. Puschmann, and J. Hasse. Orientation of CH_3O on Cu(110) as examined by near-edge x-ray-absorption fine-structure spectroscopy. *Phys. Rev. B*, 33:7336, 1986.

[96] E. Holub-Krappe, K. C. Prince, K. Horn, and D. P. Woodruff. X-ray photoelectron diffraction determination of the molecular orientation of CO and methoxy adsorbed on Cu(110). *Surf. Sci.*, 173:176–193, 1986.

[97] H. E. Dastoor, P. Gardner, and D. A. King. Identification of two tilted adsorbed μ_2-methoxy species on Ni(110) using RAIRS. *Chem. Phys. Lett.*, 209:493–498, 1993.

[98] J. Singh, W. K. Walter, A. Atrei, and D. A. King. The influence of soft mode adsorbate vibrations on NEXAFS analyses: NO on Pd(110). *Chem. Phys. Lett.*, 185:426–432, 1991.

[99] G. Blyholder. Molecular orbital view of chemisorbed carbon monoxide. *J. Phys. Chem.*, 68:2772, 1964.

[100] G. Blyholder. CNDO model of carbon monoxide chemisorbed on nickel. *J. Phys. Chem.*, 79:756, 1975.

[101] R. P. Eischens, S. A. Francis, and W. A. Pliskin. The effect of surface coverage on the spectra of chemisorbed CO. *J. Phys. Chem.*, 60:194, 1956.

[102] J. K. Nørskov. Chemisorption on metal surfaces. *Rep. Prog. Phys.*, 53:1253–1295, 1990.

[103] B. Hammer, O. Nielsen, and J. K. Nørskov. Structuresensitivity in adsorption: CO interaction with stepped and reconstructed Pt surfaces. *Catal. Lett.*, 46:31, 1997.

[104] G. Blyholder. Metal-support interaction: A theoretical approach. *J. Mol. Catal. A: Chem.*, 119:11–17, 1997.

[105] Jiwha Lee, C. P. Hanrahan, R. M. Arias, J. Martin, and H. Metiu. Detection by metastable quenching spectroscopy of enhanced back-donation from a Ni(111) surface to the $2\pi^*$ orbital of chemisorbed CO, caused by coadsorption of potassium. *Phys. Rev. Lett.*, 51:1803, 1983.

[106] K. Hermann, P. S. Bagus, and C. J. Nelin. Size dependence of surface cluster models: CO adsorbed on Cu(100). *Phys. Rev. B*, 35:9467, 1987.

[107] J. A. Rodriguez. Adsorption of CO and CO_2 on clean and cesium-covered Cu(110). *J. Phys. Chem.*, 93:5238–5248, 1989.

[108] A. F. Carley, M. W. Roberts, and A. J. Strutt. Activation of carbon monoxide and carbon dioxide at cesium-promoted Cu(110) and Cu(110)-O surfaces. *J. Phys. Chem.*, 98:9175–9181, 1998.

[109] N. M. Abbas and R. J. Madix. The effects of structured overlayers of sulfur on the kinetics and mechanism of simple reactions on Pt(111): 1. formaldehyde decomposition. *Appl. Surf. Sci.*, 7:241, 1981.

[110] E. M. Stuve, R. J. Madix, and B. A. Sexton. An EELS study of the oxidation of H_2CO on Ag(110). *Surf. Sci.*, 119:279, 1982.

[111] B. A. Sexton, A. E. Hughes, and N. R. Avery. A spectroscopic study of the adsorption and reactions of methanol, fromaldehyde and methyl formate on clean and oxygenated Cu(110) surfaces. *Surf. Sci.*, 155:366–386, 1985.

[112] A. B. Anton, J. E. Parmeter, and W. H. Weinberg. Adsorption of formaldehyde on the Ru(001) and Ru(001)-p(2×2)O surfaces. *J. Am. Chem. Soc.*, 108:1823–1833, 1986.

[113] W. E. Buhro, A. T. Patton, C. E. Strouse, and J. A. Gladysz. Synthesis, chemical properties, and X-ray crystal structures of rhenium formaldehyde and thioformaldehyde complexes. *J. Am. Chem. Soc.*, 105:1056, 1983.

[114] K. Kropp, Y. Skibbe, G. Erker, and K. Krüer. Fischer-Tropsch intermediates: Tris[(η^2-formaldehyde) zirconocene] from the carbonylation of a zirconium hydride. *J. am. Chem. Soc.*, 105:3353, 1983.

[115] R. G. Copperthwaite, P. R. Davies, M. A. Morris, M. W. Roberts, and R. A. Ryder. The reactive chemisorption of carbon dioxide at magnesium and copper surfaces at low temperature. *Catal. Lett.*, 1:11, 1988.

[116] H.-J. Freund and M. W. Roberts. Surface chemistry of charbon dioxide. *Surf. Sci. Rep.*, 25:225–173, 1996.

[117] R. A. Hadden, K. C. Vandervell, H. D. Waugh, and G. Webb. The adsorption and decomposition of carbon dioxide on polycrystalline copper. *Catal. Lett.*, 1: 27, 1988.

[118] D. J. Coulman, J. Wintterlin, R. J. Behm, and G. Ertl. Novel mechanism for the formation of chemisorption phases: The (2 × 1)O-Cu(110) "Added-Row" Reconstruction. *Phys. Rev. Lett.*, 64:1761, 1990.

[119] F. Jensen, F. Bensenbacher, E. Lægsgaard, and I. Stensgaard. Surface reconstruction of Cu(110) induced by oxygen chemisorption. *Phys. Rev. B*, 41:10223, 1990.

[120] F. M. Leibsle, S. M. Francis, R. Davis, N. Xiang, S. Haq, and M. Bowker. Scanning tunneling microscopy studies of formalehyde synthesis on Cu(110). *Phys. Rev. Lett.*, 72:2569, 1994.

[121] F. M. Leibsle, S. M. Francis, S. Haq, and M. Bowker. Aspects of formaldehyde

synthesis on Cu(110) as studied by STM. *Surf. Sci.*, 318:46–60, 1994.

[122] S. Poulston, A. H. Jones, R. A. Bennett, and M. Bowker. Contrasting reaction pathways in methanol oxidation on Cu(110) studied by STM. *J. Phys.: Condens. Matter*, 8:L765–L771, 1996.

[123] S. L. Silva, R. M. Lemor, and F. M. Leibsle. STM studies of methanol oxidation to formate on Cu(110) surfaces: I. sequential dosing experiments. *Surf. Sci.*, 421: 135–145, 1999.

[124] S. L. Silva, R. M. Lemor, and F. M. Leibsle. STM studies of methanol oxidation to formate on Cu(110) surfaces: II. codosing experiments. *Surf. Sci.*, 421:146–156, 1999.

[125] M. A. Karolewski and R. G. Cavell. Characterisation of adsorbed intermediates in the $CH_3OH/O/Cu(100)$ system by secondary ion mass spectrometry. *Appl. Surf. Sci.*, 173:151–163, 2001.

[126] Á. Logadóttir and J. K. Nørskov. Ammonia synthesis over a Ru(0001) surface studied by density functional calculations. *J. Catal.*, 220:273–279, 2003.

[127] M. Günter, T. Ressler, B. Bems, C. Büscher, T. Genger, O. Hinrichsen, M. Muhler, and R. Schlögl. Implication of the microstructure of binary Cu/ZnO catalysts for their catalytic activity in methanol synthesis. *Catal. Lett.*, 71:37, 2001.

[128] B. Hammer and J. K. Nørskov. Electronic factors determining the reactivity of metal surfaces. *Surf. Sci.*, 343:211–220, 1995.

[129] M. Mavrikakis, B. Hammer, and J. K. Nørskov. Effect of strain on the reactivity of metal surfaces. *Phys. Rev. Lett.*, 81:2819, 1998.

[130] A. Ruban, B. Hammer, H. L. Stoltze, P. Skriver, and J. K. Nørskov. Surface electronic structure and reactivity of transition and noble metals. *J. Mol. Catal. A*, 115:421–429, 1997.

[131] Y. Xu and M. Mavrikakis. Adsorption and dissociation of O_2 on Cu(111): thermochemistry, reaction barrier and the effect of strain. *Surf. Sci.*, 494:131–144, 2001.

[132] G. Anger, A. Winkler, and K. D. Rendulic. Adsorption and desorption kinetics in the systems $H_2/Cu(111)$, $H_2/Cu(110)$ and $H_2/Cu(100)$. *Surf. Sci.*, 220:1–17, 1989.

[133] A. Hodgson, J. Moryl, P. Traversaro, and H. Zhao. Energy transfer and vibrational effects in the dissociation and scattering of D_2 from Cu(111). *Nature*, 356: 501, 1992.

[134] M. Gostein, H. Parhiktheh, and G. O. Sitz. Survival probability of H_2 ($\nu = 1$, $J = 1$) scattered from Cu(110). *Phys. Rev. Lett.*, 75:342, 1995.

[135] H. Hou, S. J. Gulding, C. T. Rettner, A. M. Wodtke, and D. J. Auerbach. The stereodynamics of a gas-surface reaction. *Science*, 277:80, 1997.

[136] K. Svensson, L. Bengtsson, J. Bellman, M. Hassel, M. Persson, and S. J. Andersson. Two-dimensional quantum rotation of adsorbed H_2. *Phys. Rev. Lett.*, 83: 124, 1999.

[137] C. T. Rettner, H. A. Michelsen, and D. J. Auerbach. Quantum-state-specific

dynamics of the dissociative adsorption and associative desorption of H_2 at a Cu(111) surface. *J. Chem. Phys.*, 102:4625–4641, 1995.

[138] B. Hammer, M. Scheffler, K. W. Jacobsen, and J. Nørskov. Multidimensional potential energy surface for H_2 dissociation over Cu(111). *Phys. Rev. Lett.*, 73: 1400, 1994.

[139] A. Groß, B. Hammer, M. Scheffler, and W. Brenig. High-dimensional quantum dynamics of adsorption and desorption of H_2 at Cu(111). *Phys. Rev. Lett.*, 73: 3121, 1994.

[140] G. R. Darling and S. Holloway. Rotational motion and the dissociation of H_2 on Cu(111). *J. Chem. Phys.*, 101:3268–3281, 1994.

[141] G. R. Darling and S. Holloway. The dissociation of diatomic molecules at surfaces. *Rep. Prog. Phys.*, 58:1595–1672, 1995.

[142] G.-J. Kroes, E. J. Baerends, and R. C. Mowrey. Six-dimensional quantum dynamics of dissociative chemisorption of ($\nu = 0$, $j = 0$) H_2 on Cu(100). *Phys. Rev. Lett.*, 78:3583, 1997.

[143] D. M. Bird. Effects of coadsorbates in dissociative chemisorption of hydrogen on metallic surfaces. *Faraday Discuss.*, 110:335–346, 1998.

[144] G.-J. Kroes. Six-dimensional quantum dynamics of dissociative chemisorption of H_2 on metal surfaces. *Prog. Surf. Sci.*, 60:1–85, 1999.

[145] Axel Groß. Reactions at surfaces studied by ab initio dynamics calculations. *Surf. Sci. Rep.*, 32:291–340, 1998.

[146] W. A. Diño, H. Kasai, and A. Okiji. Orientational effects in dissociative adsorption associative desorption dynamics of $H_2(D_2)$ on Cu and Pd. *Prog. Surf. Sci.*, 63:63–134, 2000.

[147] Ž. Šljivančanin and B. Hammer. H_2 dissociation at defected Cu: Preference for reaction at vacancy and kink sites. *Phys. Rev. B*, 65:85414, 2002.

[148] J. Harris and S. Andersson. H_2 dissociation at metal surfaces. *Phys. Rev. Lett.*, 55:1583, 1985.

[149] M. H. Cohen, M. V. Ganguglia-Pirovano, and J. Kudrnovský. Orbital symmetry, reactivity, and transition metal surface chemistry. *Phys. Rev. Lett.*, 72:3222, 1994.

[150] V. Pallassana, M. Neurock, L. Hansen, B. Hammer, and J. Nørskov. Theoretical analysis of hydrogen chemisorption on Pd(111), Re(0001) and Pd_{ML}/Re(0001), Re_{ML}/Pd(111) pseudomorphic overlayers. *Phys. Rev. B*, 60:6146, 1999.

[151] N. D. Lang and A. Williams. Theory of atomic chemisorption on simple metals. *Phys. Rev. B*, 18:616, 1978.

[152] C. N. Hinselwood. Hydrogen chemisorption by the spin-density functional formalism: 2. role of the sp-conduction electrons of metal-surfaces. *Phys. Scripta*, 18:481–493, 1978.

[153] P. Kratzer, B. Hammer, and J. K. Nørskov. Geometric and electronic factors determining the differences in reactivity of H_2 on Cu(100) and Cu(111). *Surf. Sci.*, 359:45–53, 1996.

[154] J. Strömquist, L. Bengtsson, M. Persson, and B. Hammer. The dynamics of H absorption in and adsorption on Cu(111). *Surf. Sci.*, 397:382–394, 1998.

[155] B. Hammer and J. K. Nørskov. Why gold is the noblest of all the metals. *Nature*, 376:238–240, 1995.

[156] Y. Xu and M. Mavrikakis. private communication.

[157] Ata Roudgar and Axel Groß. Local reactivity of metal overlayers: Density functional theory calculations of Pd on Au. *Phys. Rev. B*, 67:033409, 2003.

[158] S. Wilke and M. Scheffler. Poisoning of Pd(100) for the dissociation of H_2: a theoretical study of co-adsorption of hydrogen and sulphur. *Surf. Sci.*, 329: L605–L610, 1995.

[159] C. M. Wei, A. Groß, and M. Scheffler. *Ab initio* calculation of the potential energy surface for the dissociation of H_2 on the sulfur-covered Pd(100) surface . *Phys. Rev. B*, 57:15572, 1998.

[160] P. Kratzer, B. Hammer, and J. K. Nørskov. A theoretical study of CH_4 dissociation on pure and gold-alloyed Ni(111) surfaces. *J. Chem. Phys.*, 105:5595, 1996.

[161] S. Sakong and A. Groß. Dissociative adsorption of hydrogen on strained Cu surfaces. *Surf. Sci.*, 525:107–118, 2003.

[162] B. A. Sexton. Surface vibrations of adsorbed intermediates in the reaction of alcohols with Cu(100). *Surf. Sci.*, 88:299–318, 1979.

[163] R. J. Madix and S. G. Telford. Primary and secondary kinetic isotope effects for methoxy dehydrogenation and Cu(110): absence of tunnelling corrections. *Surf. Sci.*, 328:L576–L581, 1995.

[164] A. F. Carley, P. R. Davies, G. G. Mariotti, and S. Read. Reaction pathways in methanol oxidation at Cu(110) surfaces. *Surf. Sci.*, 364:L525–L529, 1996.

[165] F. Raimondi, K. Geissler, J. Wambach, and A. Wokaun. Hydrogen production by methanol reforming: post-reaction characterization of a $Cu/ZnO/Al_2O_3$ catalyst by XPS and TPD. *Appl. Surf. Sci.*, 189:59–71, 2002.

[166] N. Canning and R. J. Madix. Towards an organometallic chemistry of surface. *J. Phys. Chem.*, 88:2437–2446, 1984.

[167] D. A. Outka and R. J. Madix. Brønsted basicity of atomic oxygen on the Au(110) surface: Reactions with methanol, acetylene, water and ethylne. *J. Am. Chem. Soc.*, 109:1708–1714, 1987.

[168] I. Langmuir. The mechanism of the catalytic action of platinum in the reactions of $2CO + O_2 = 2CO_2$ and $2H_2 + O_2 = 2H_2O$. *Trans. Faraday Soc.*, 17:621, 1922.

[169] C. N. Hinselwood. Annual reports on the progress of chemistry. *Ann. Res. London Chem. Soc.*, 27:11, 1930.

[170] Ch. Ammon, A. Bayer, G. Held, B. Richer, Th. Schmidt, and H. P. Steinrück. Dissociation and oxidation of methanol on Cu(110). *Surf. Sci.*, 507:845–850, 2002.

[171] I. E. Wachs and R. J. Madix. The oxidation of H_2CO on a copper(110) surface. *Surf. Sci.*, 84:375, 1979.

[172] P. R. Davies and G. G. Mariotti. Controlling reaction selectivity in the oxidation of methanol at Cu(110) surfaces. *Catal. Lett.*, 43:261, 1997.

[173] M. Bowker, S. Poulston, R. A. Bennett, and A. H. Jones. Comments on "Controlling reaction selectivity in the oxidation of methanol at Cu(110) surfaces" by P.R. Davies and G.G. Mariotti. *Catal. Lett.*, 43:267, 1997.

[174] A. K. Chen and Rich Masel. Direct conversion of methanol to formaldehyde in the absence of oxygen on Cu(210). *Surf. Sci.*, 343:17–23, 1995.

[175] A. Knop-Gericke, M. Hävecker, T. Schedel-Niedrig, and R. Schlögl. High-pressure low-energy XAS: a new tool for probing reacting surfaces of heterogeneous catalysts. *Top. in Catal.*, 10:187–198, 2000.

[176] A. Knop-Gericke, M. Hävecker, T. Schedel-Niedrig, and R. Schlögl. Probing the electronic structure of an active catalyst surface under high-pressure reaction conditions: the oxidation of methanol over copper. *Catal. Lett.*, 66:215–220, 2000.

[177] A. Knop-Gericke, M. Hävecker, T. Schedel-Niedrig, and R. Schlögl. Characterisation of active phases of a copper catalyst for methanol oxidation under reaction conditions: an in situ X-ray absorption. *Top. in Catal.*, 15:27, 2001.

[178] V. Pallassana and M. Neurock. Electronic factors governing ethylene hydrogenation and dehydrogenation activity of pseudomorphic $Pd_{ML}/Re(0001)$, $Pd_{ML}/Ru(0001)$, Pd(111), and $Pd_{ML}/Au(111)$ surfaces. *J. Catal.*, 191:301–317, 2000.

[179] V. Pallassana, M. Neurock, V. S. Lusvardi, J. J. Lerour, D. D. Kragten, and R. A. van Santen. A density functional theory analysis of the reaction pathways and intermediates for ethylene dehydrogenation over Pd(111). *J. Phys. Chem. B*, 106:1656–1669, 2002.

[180] E. M. Stuve and R. J. Madix. Bonding and dehydrogenation of ethylene on palladium metal: Vibrational spectra and temperature programmed reaction studies on Pd(100). *J. Phys. Chem.*, 89:105–112, 1985.

[181] H. L. Abbott, A. Bukoski, and I. Kavulak, D. F. Harrison. Dissociative chemisorption of methane on Ni(100): Threshold energy from $CH_4(2\nu_3)$ eigenstate-resolved sticking measurements. *J. Chem. Phys.*, 119:6407, 2003.

[182] O. Swang, K. Faegri, O. Gropen, U. Wahlgren, and P. Siegbahn. A theoretical study of the chemisorption of methane on a Ni(100) surface. *Chem. Phys.*, 156: 379, 1991.

[183] H. Yang and J. L. Whitten. Dissociative chemisorption of CH_4 on Ni(111). *J. Chem. Phys.*, 96:5529, 1992.

[184] K.-H. Ernst, C. T. Campbell, and G Moretti. Kinetics of the reverse water-gas shift reaction over Cu(110). *J. Catal.*, 134:66–74, 1992.

[185] M. J. L. Ginés, A. J. Marchi, and C. R. Apesteguía. Kinetic study of the reverse water-gas shift reaction over $CuO/ZnO/Al_2O_3$ catalysts. *Appl. Catal. A: General*, 154:155–171, 1997.

[186] W. S. Sim, P. Gardner, and D. A. King. Structure and reactivity of the surface

methoxy species on Ag(111). *J. Phys. Chem.*, 99:16002, 1995.

[187] Christian Sendner, Sung Sakong, and Axel Groß. to be published.

[188] Sung Sakong, Christian Sendner, and Axel Groß. Partial oxidation of methanol on Cu(110): energetics and kinetics. *J. Mol. Struct. (Theochem)*. subm. March 2005.

[189] A. H. Jones, S. Poulston, R. A. Bennett, and M. Bowker. Methanol oxidation to formate on Cu(110) studied by STM. *Surf. Sci.*, 380:31–44, 1997.

List of publications

1. Sung Sakong and Axel Groß. Dissociative adsorption of hydrogen on strained Cu surfaces *Surf. Sci.*, 434:107-118, 2003

2. Sung Sakong and Axel Groß. Density functional theory study of the partial oxidation of methanol on copper surfaces *J. Catal.*, 231:420-429, 2005

3. Arezoo Dianat, Sung Sakong and Axel Groß. Quantum dynamics of the dissociation of H_2 on Rh(111) *Eur. J. Phys. B*, 45:425-432, 2005

4. Sung Sakong, Christian Sendner, and Axel Groß. Partial oxidation of methanol on Cu(110): energetics and kinetics *J. Mol. Struct. (Theochem)*, subm. March 2005.